Meteorological Model Performance for Annual 2016 Simulation WRF v3.8

EPA-454/R-19-010

July 2019

Meteorological Model Performance for Annual 2016 Simulation WRF v3.8

U.S. Environmental Protection Agency

Office of Air Quality Planning and Standards

Air Quality Assessment Division

Research Triangle Park, NC

Meteorological Model Performance for Annual 2016 Simulation WRF v3.8

1. INTRODUCTION

The Weather Research and Forecasting model (WRF) was applied for the entire year of 2016 to generate meteorological data to support emissions and photochemical modeling applications for this year. The WRF meteorological fields will be converted to air quality modeling input data and used to support assessments of ozone, PM2.5, visibility, and a variety of toxics.

The WRF model was applied to 36 km North America (36NOAM) and 12 km continental United States (12US) scale domains. Both model simulations were initialized directly from meteorological analysis data. Model parameterizations and options outlined in this document were chosen based on a series of sensitivity runs performed by U.S. Environmental Protection Agency (USEPA) Office of Research and Development that provided an optimal configuration based on temperature, mixing ratio, and wind field. All WRF simulations were done by CSRA under contract to the USEPA.

2. MODEL CONFIGURATION

Version 3.8 of the WRF model, Advanced Research WRF (ARW) core (Skamarock, 2008) was used for generating the 2016 simulation[1]. Selected physics options include Pleim-Xiu land surface model, Asymmetric Convective Model version 2 planetary boundary layer scheme, Kain-Fritsch cumulus parameterization utilizing the moisture-advection trigger (Ma and Tan, 2009), Morrison double moment microphysics, and RRTMG longwave and shortwave radiation schemes (Gilliam and Pleim, 2010).

The 36NOAM WRF model was initialized using the 0.25-degree GFS analysis and 3-hour forecast from the 00Z, 06Z, 12Z, and 18Z simulations. The 12US WRF model was initialized using the 12km North American Model (12NAM) analysis product provided by National Climatic Data Center (NCDC). Where 12NAM data was unavailable, the 40km Eta Data Assimilation System (EDAS) analysis (ds609.2) from the National Center for Atmospheric Research (NCAR) was used. Analysis nudging for temperature, wind, and moisture was applied above the boundary layer only. The model simulations were conducted continuously. The 'ipxwrf' program was used to initialize deep soil moisture at the start of the run using a 10-day spinup period (Gilliam and Pleim, 2010). Landuse and land cover data were based on the USGS for the 36NOAM simulation and the 2011 National Land Cover Database (NLCD 2011) for the 12US simulation. Sea surface temperatures were ingested from the Group for High Resolution Sea Surface Temperatures (GHRSST) (Stammer et al., 2003) 1km SST data.

[1] Version 3.8 was the most current version of WRF at the time the 2016 meteorological model simulations were performed.

Additionally, lightning data assimilation was utilized to suppress (force) deep convection where lightning is absent (present) in observational data. This method is described by Heath et al. (2016) and was employed to help improve precipitation estimates generated by the model.

Figures 2.1 and 2.2 show the 36NOAM and 12US domains, which utilize a Lambert conformal projection centered at (-97,40) with true latitudes of 33 and 45 degrees north. The 36NOAM domain contains 184 cells in the X direction and 160 cells in the Y direction. The 12US domain contains 412 cells in the X direction and 372 cells in the Y direction. The atmosphere is resolved with 35 vertical layers up to 50 mb (see table 2.1), with the thinnest layers being nearest the surface to better resolve the planetary boundary layer (PBL).

WRF Layer	**Height (m)**	**Pressure (mb)**	**Sigma**
35	17,556	5000	0.000
34	14,780	9750	0.050
33	12,822	14500	0.100
32	11,282	19250	0.150
31	10,002	24000	0.200
30	8,901	28750	0.250
29	7,932	33500	0.300
28	7,064	38250	0.350
27	6,275	43000	0.400
26	5,553	47750	0.450
25	4,885	52500	0.500
24	4,264	57250	0.550
23	3,683	62000	0.600
22	3,136	66750	0.650
21	2,619	71500	0.700
20	2,226	75300	0.740
19	1,941	78150	0.770
18	1,665	81000	0.800
17	1,485	82900	0.820
16	1,308	84800	0.840
15	1,134	86700	0.860
14	964	88600	0.880
13	797	90500	0.900
12	714	91450	0.910
11	632	92400	0.920
10	551	93350	0.930
9	470	94300	0.940
8	390	95250	0.950
7	311	96200	0.960

6	232	97150	0.970
5	154	98100	0.980
4	115	98575	0.985
3	77	99050	0.990
2	38	99525	0.995
1	19	99763	0.9975
Surface	0	100000	1.000

Table 2.1 WRF layers and their approximate height above ground level.

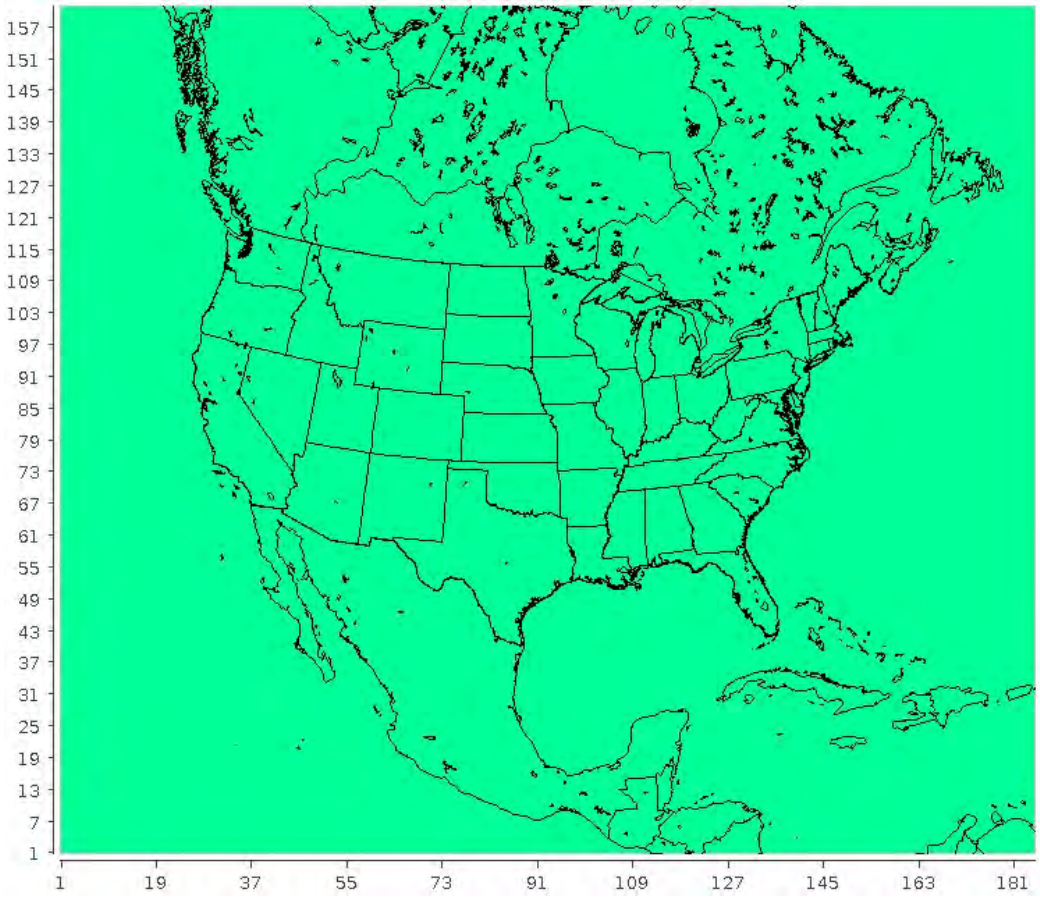

Figure 2.1 Map of WRF model domain: 36NOAM.

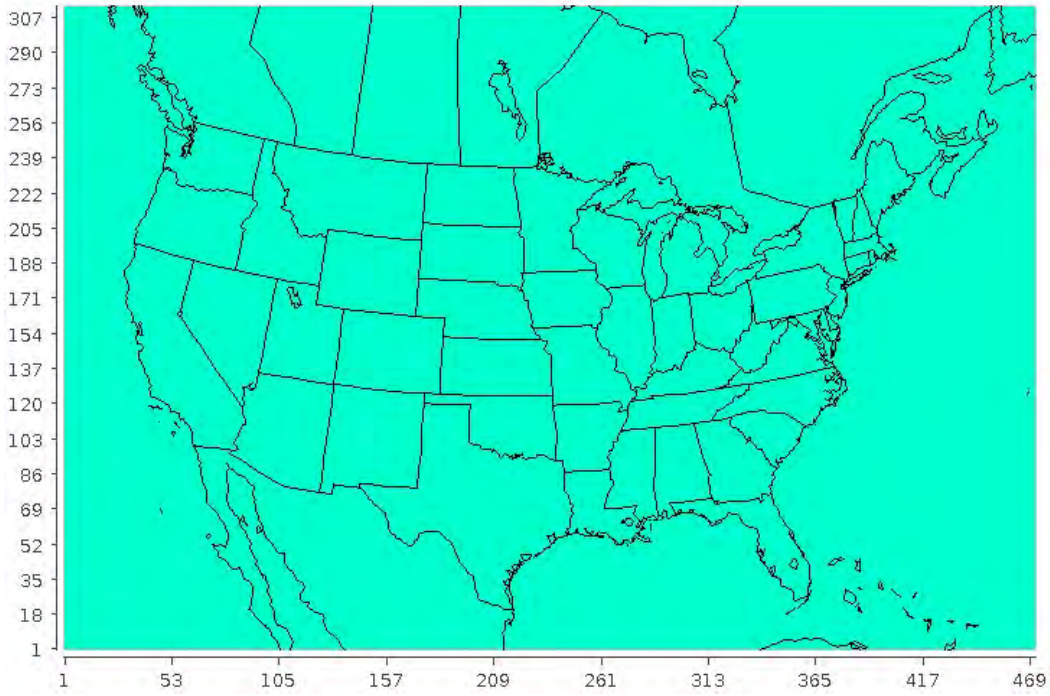

Figure 2.2 Map of WRF model domain: 12US.

3 MODEL PERFORMANCE DESCRIPTION

The WRF model simulations were evaluated to determine whether the output fields represent a reasonable approximation of the actual meteorology that occurred during the modeling period. Identifying and quantifying these output fields allows for a downstream assessment of how the air quality modeling results are impacted by the meteorological data. For the purposes of this assessment, 2-meter temperature and mixing ratio, 10-meter wind speed and direction, and shortwave radiation are quantitatively evaluated. A qualitative and quantitative evaluation of precipitation is also provided.

The observation database for surface-based temperature, wind speed and direction, and mixing ratio is based on measurements made at United States (i.e., National Weather Service) and Canadian (i.e., Environment Canada) airports. The observational dataset (ds472 network) is available from NCAR. Monitors used for evaluation are shown in Figure 3.1.

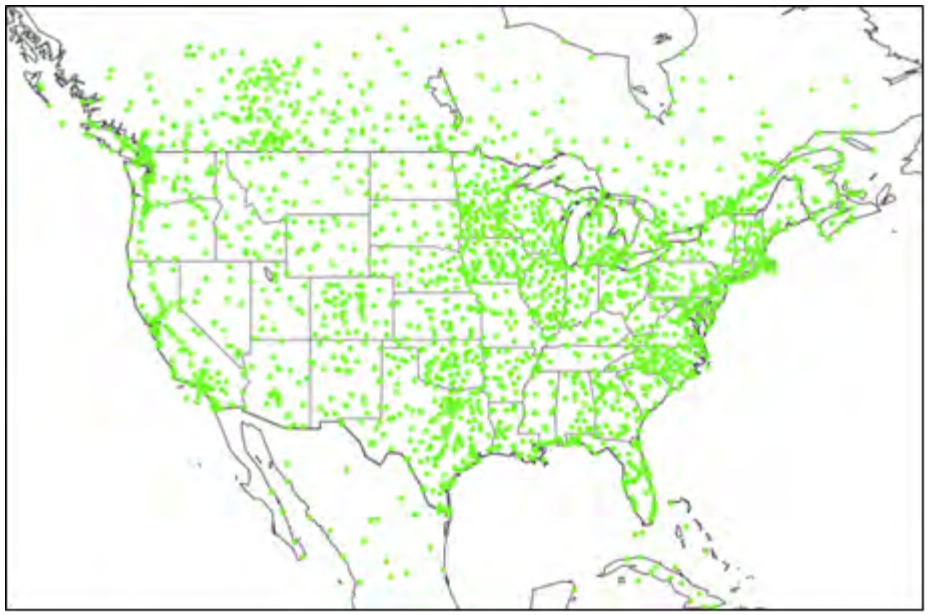

Figure 3.1 Stations used for model performance: ds472 network.

Shortwave downward radiation measurements are taken at Surface Radiation Budget Network (SURFRAD) (https://www.esrl.noaa.gov/gmd/grad/surfrad/index.html) and SOLRAD (formerly ISIS) (https://www.esrl.noaa.gov/gmd/grad/solrad/index.html) monitor locations. The SURFRAD network consists of 7 sites and the SOLRAD network consists of 9 sites across the United States (see Figure 3.2). Both networks are operated by the National Oceanic and Atmospheric Administration (NOAA), with SURFRAD sites existing as a subset of SOLRAD monitors that provide higher level radiation information not used in this evaluation.

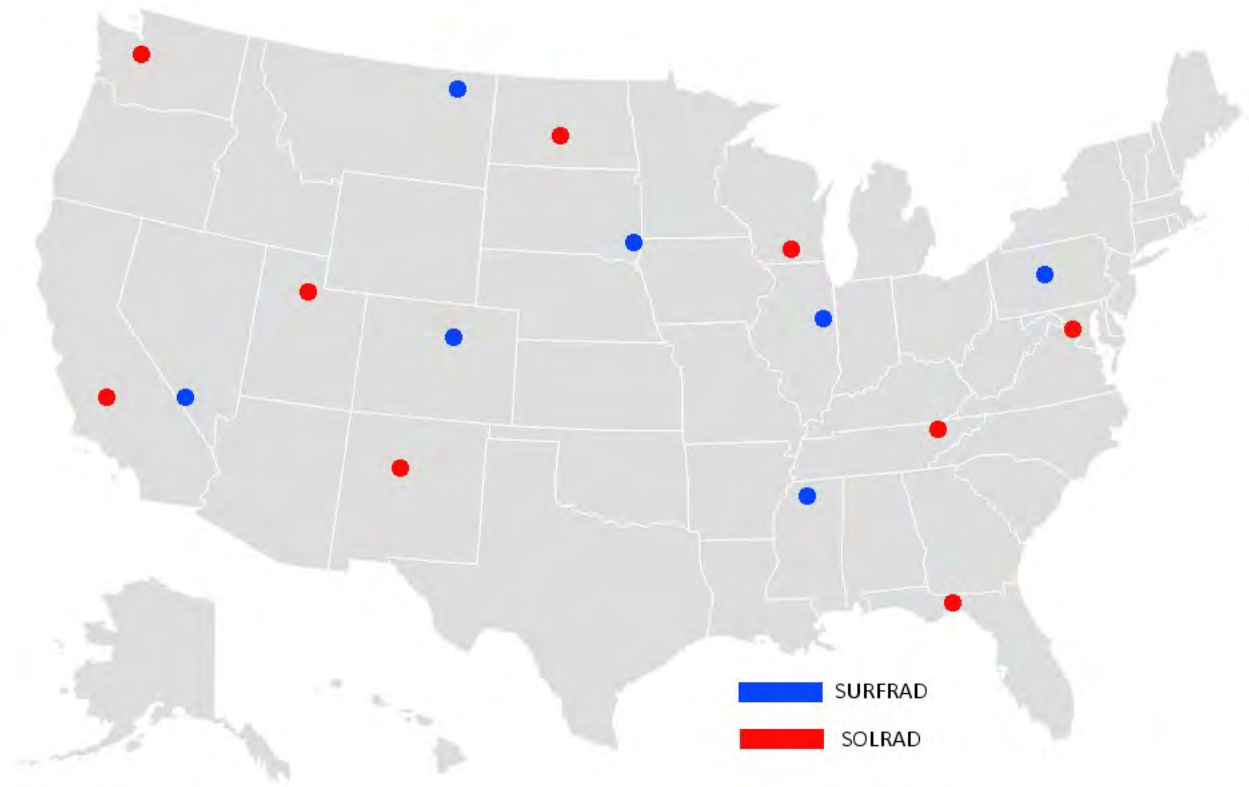

Figure 3.2. Location of SOLRAD and SURFRAD radiation monitors.

Rainfall amounts are estimated by the Parameter-elevation Relationships on Independent Slopes Model (PRISM) model, which uses an elevation-based regression model to analyze precipitation. PRISM's horizontal resolution is approximately 2 to 4 km and is re-projected to the WRF modeling domain for direct comparison to model estimates. The rainfall analysis is limited to the contiguous United States as the model utilizes elevation and measured precipitation data at automated weather stations.

Model performance (i.e., temperature, wind speed, and mixing ratio) is described using quantitative metrics: mean bias, mean (gross) error, fractional bias, and fractional error (Boylan and Russell, 2006). These metrics are useful because they describe model performance in the measured units of the meteorological variable and as a normalized percentage. Since wind direction is reported in compass degrees, estimating performance metrics for wind direction is problematic as modeled and observed northerly winds may be similar but differences would result in a very large artificial bias. For example, the absolute difference in a northerly wind direction measured in compass degrees of 1° and 359° is 358° when the actual difference is only 2°. To address this issue, wind field displacement, or the difference in the U and V vectors between modeled (M) and observed (O) values, is used to assess wind vector performance (Equation 1). Performance is best when these metrics approach 0.

(1) Wind displacement (km) = $(\mathbf{U}_M - \mathbf{U}_O + \mathbf{V}_M - \mathbf{V}_O)$*(1 km/1000 m)*(3600 s/hr)*(1 hr)

Rainfall performance is examined spatially using side-by-side comparisons of monthly total rainfall plots. The WRF model outputs predictions approximately 15 meters above the surface while observations are at 10 meters. WRF generates output at near instantaneous values (90 second time step) as opposed to longer averaging times taken at monitor stations. This should be considered when interpreting model performance metrics.

3.1 Model Performance for Winds

WRF-predicted wind speed estimates are compared to surface-based measurements made in the ds472 network described earlier. The results for the 36NOAM (Figure 3.1.1) and 12US (Figure 3.1.2) domains are shown below.

At 36km, wind speeds are generally overpredicted across most hours of the day for all seasons, in terms of mean bias. In general, performance improves at 12km with less overprediction relative to the 36km simulation. However, at 12km WRF tends to slightly overpredict wind speeds in the early morning and afternoon hours, while slightly underpredicting wind speeds in the late evening and overnight hours. There is no significant seasonal variability at either resolution in terms of wind speed.

The monthly spatial distributions of the wind speed biases (m/s) for all hours (Figures 3.1.3-3.1.10) and daytime hours[2] (Figures 3.1.11-3.1.18) are also presented, as well as the hourly average distribution of observed and predicted wind speeds by season and region (Figure 3.1.19). The previously mentioned overprediction of wind speeds at 36km is noticeable, primarily across the eastern coastal areas of the US and upper Midwest and Great Lakes regions. This overprediction improves significantly at 12km, though it still persists across the eastern US. The WRF simulations tend to underpredict wind speeds in the western US, though this underprediction is muted slightly during the daytime hours. As noted above, these biases generally persist regardless of changes in season.

[2] 12UTC to 00UTC

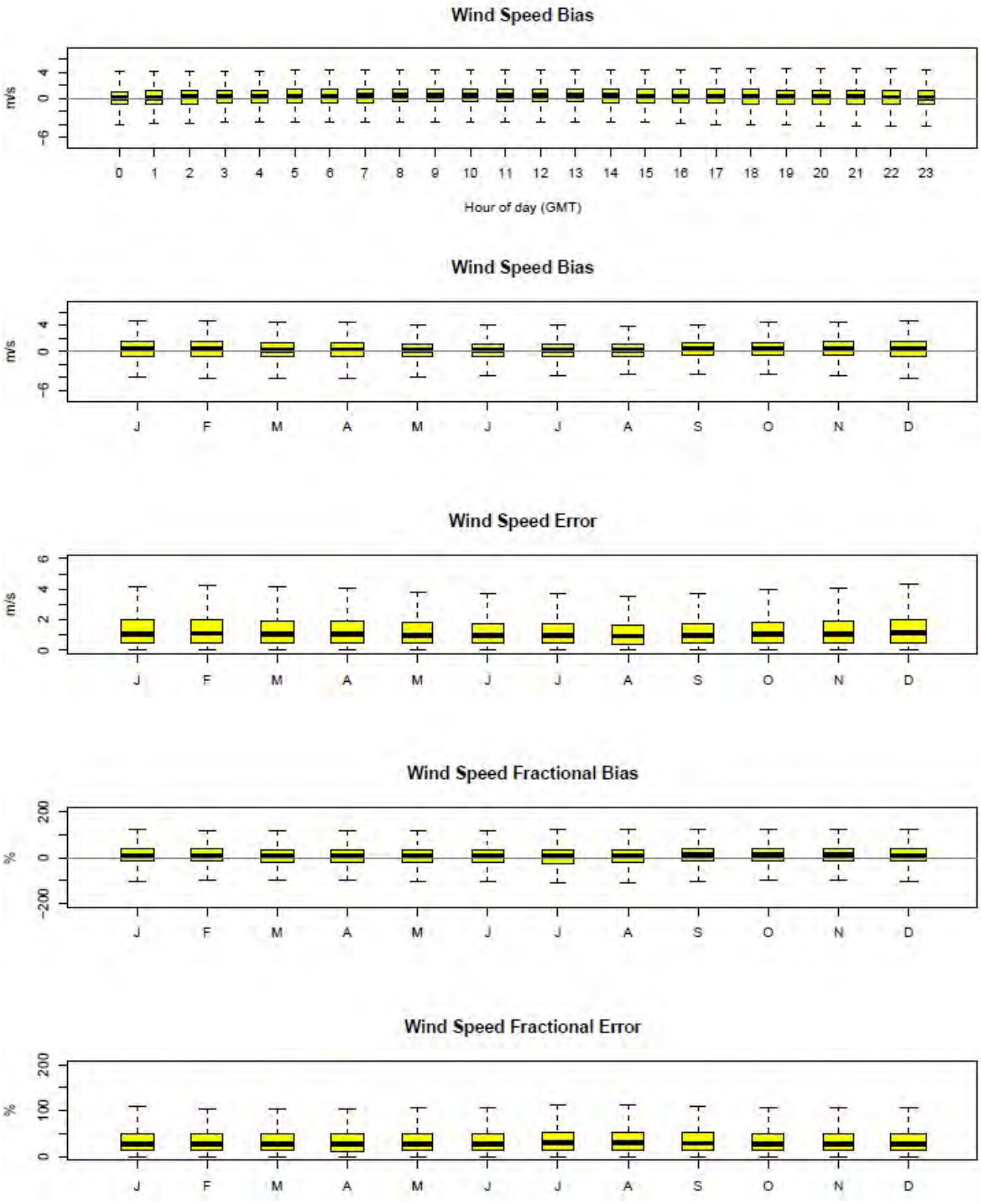

Figure 3.1.2. Distribution of hourly bias by hour and hourly bias, error, fractional bias, and fractional error for wind speed by month for 36NOAM domain.

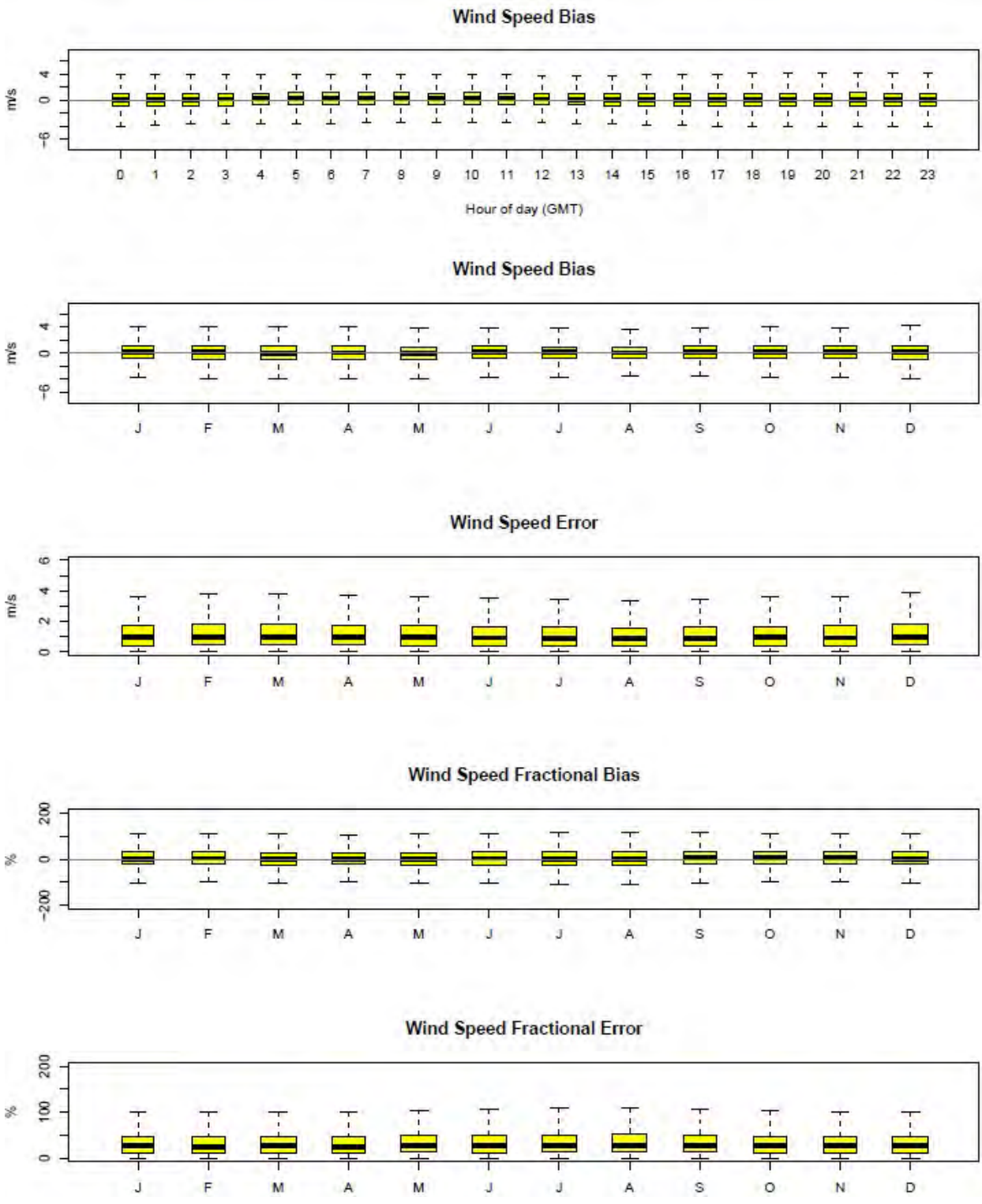

Figure 3.1.2. Distribution of hourly bias by hour and hourly bias, error, fractional bias, and fractional error for wind speed by month for 12US domain.

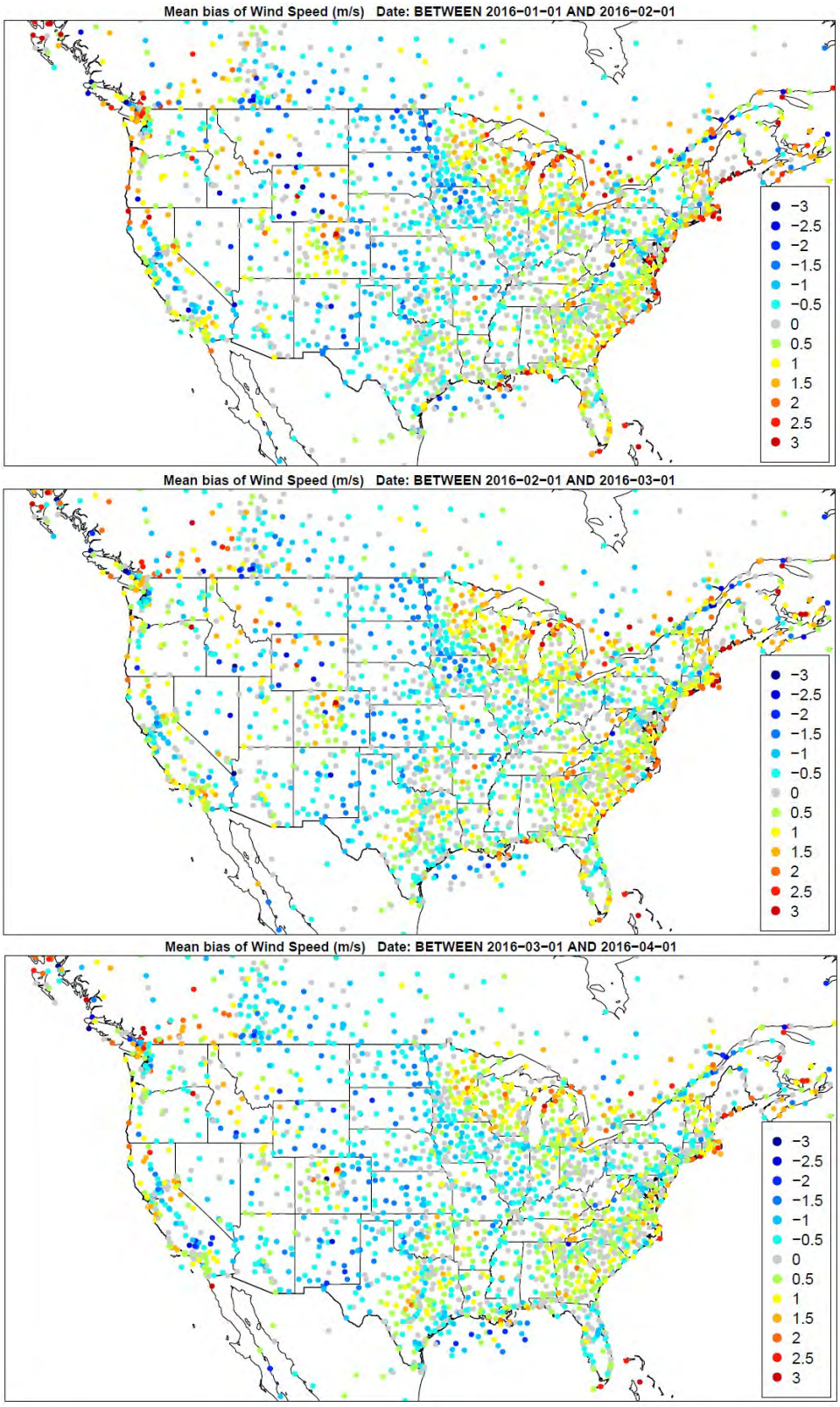

Figure 3.1.3. Spatial distribution of wind speed bias (m/s) across all hours for the months of January, February, and March (top to bottom) for the 36NOAM domain.

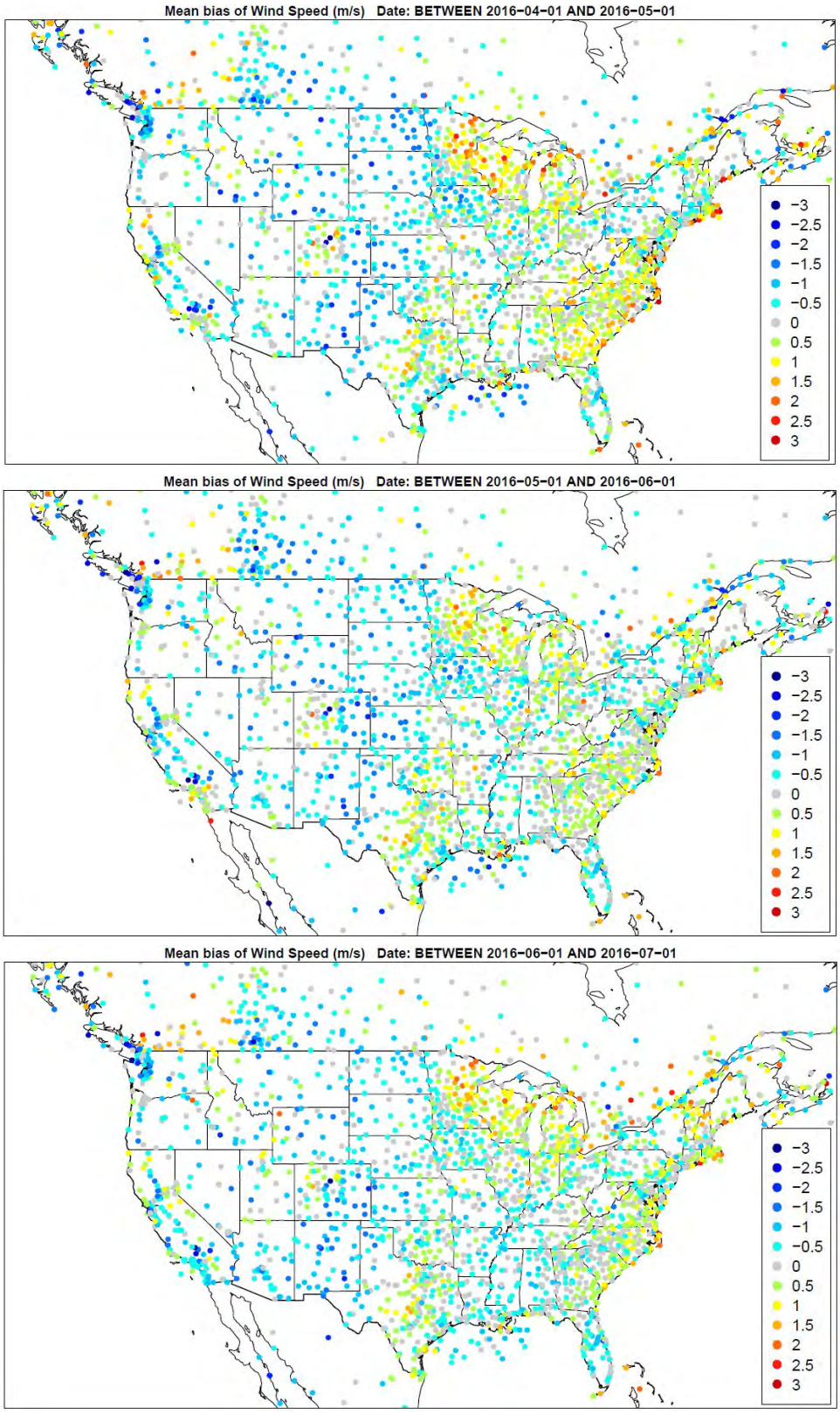

Figure 3.1.4. Spatial distribution of wind speed bias (m/s) across all hours for the months of April, May, June (top to bottom) for the 36NOAM domain.

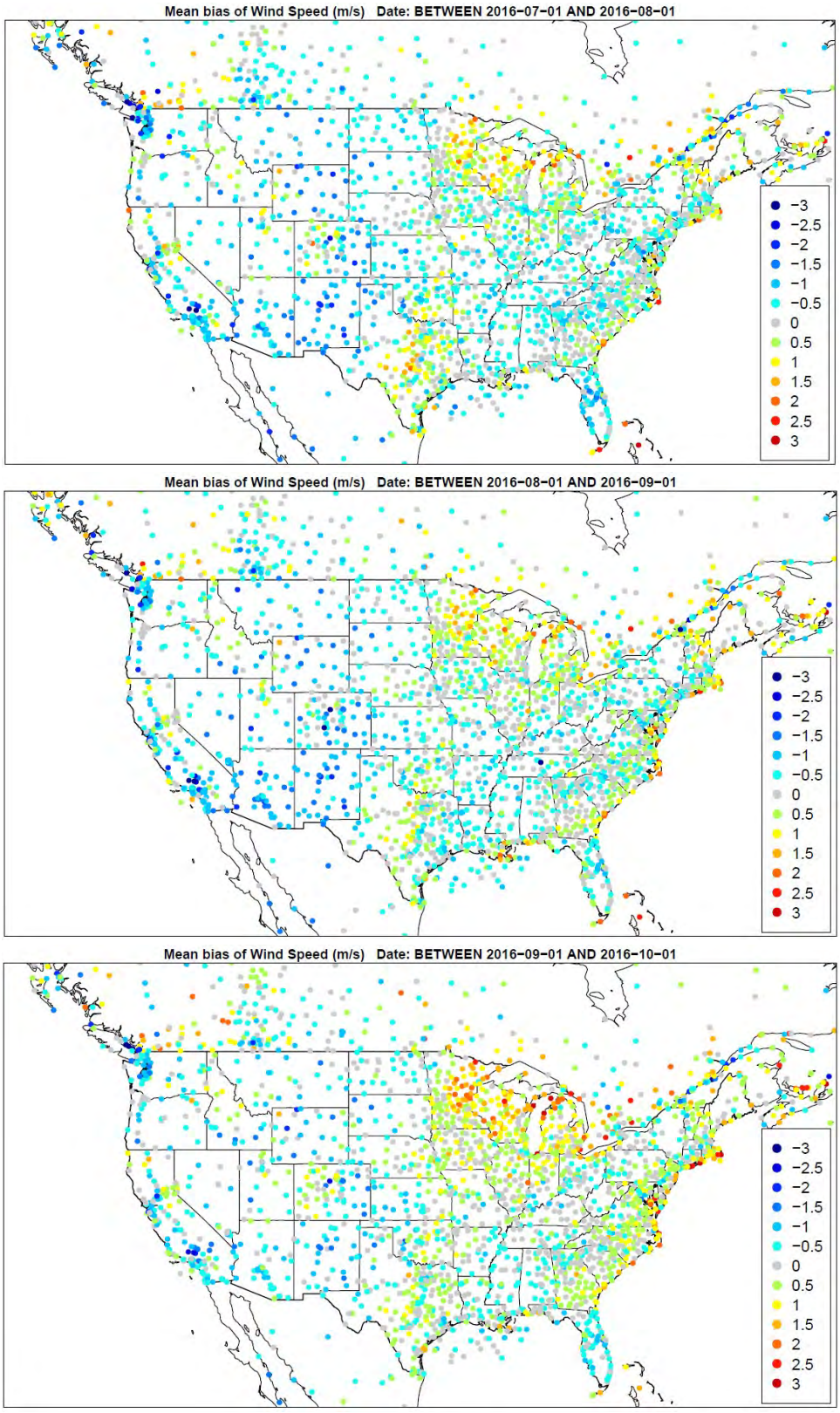

Figure 3.1.5. Spatial distribution of wind speed bias (m/s) across all hours for the months of July, August, September (top to bottom) for the 36NOAM domain.

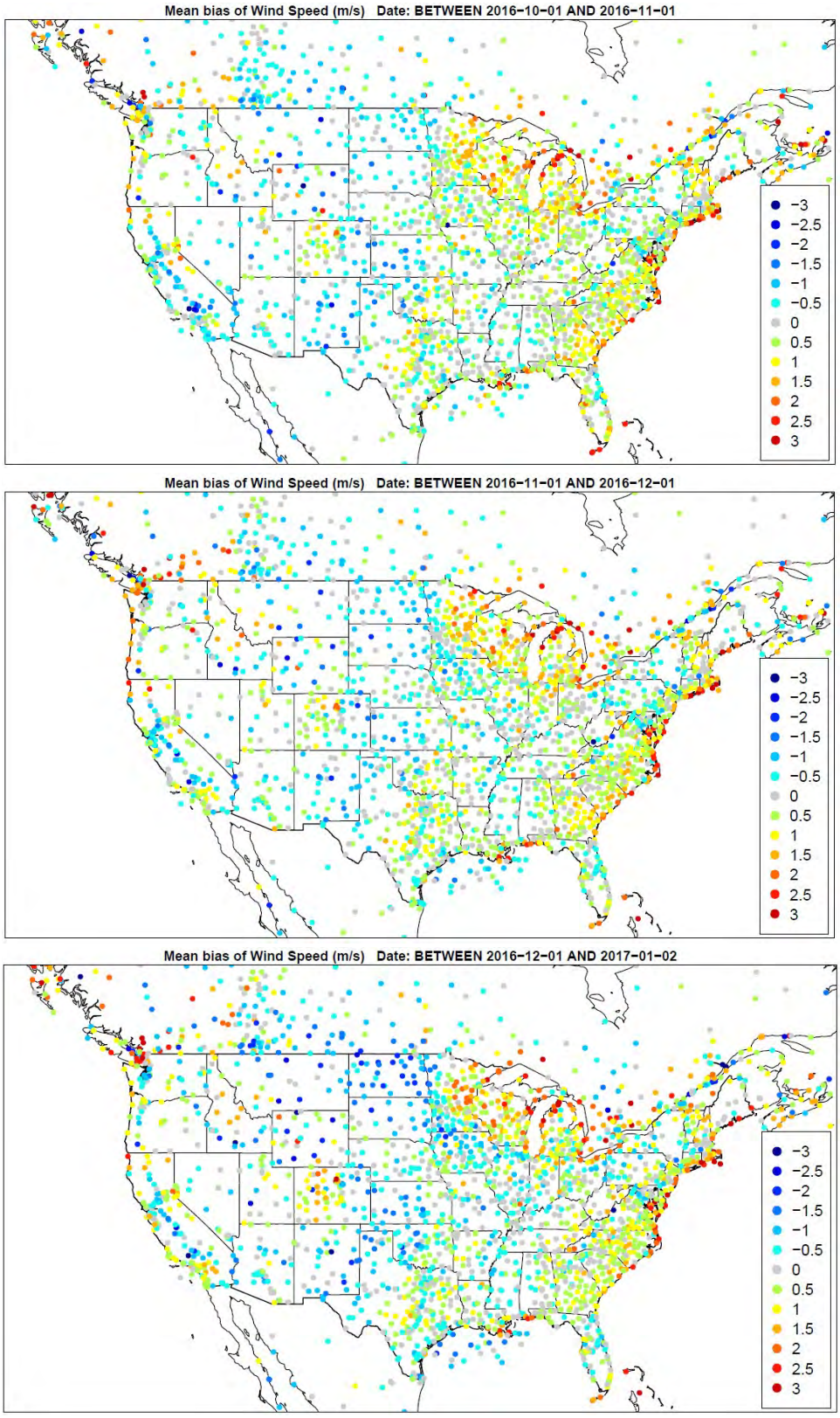

Figure 3.1.6. Spatial distribution of wind speed bias (m/s) across all hours for the months of October, November, December (top to bottom) for the 36NOAM domain.

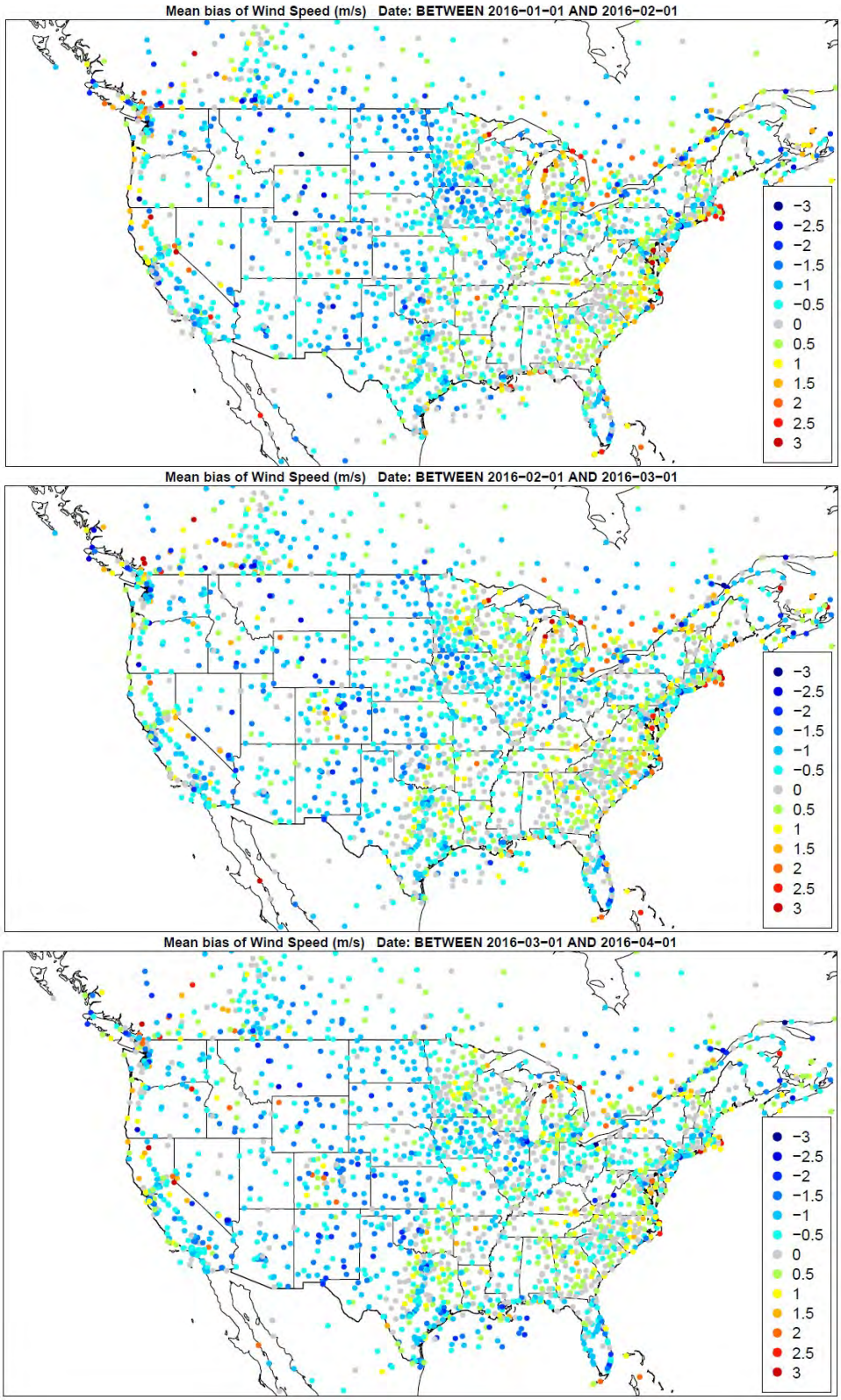

Figure 3.1.7. Spatial distribution of wind speed bias (m/s) across all hours for the months of January, February, and March (top to bottom) for the 12US domain.

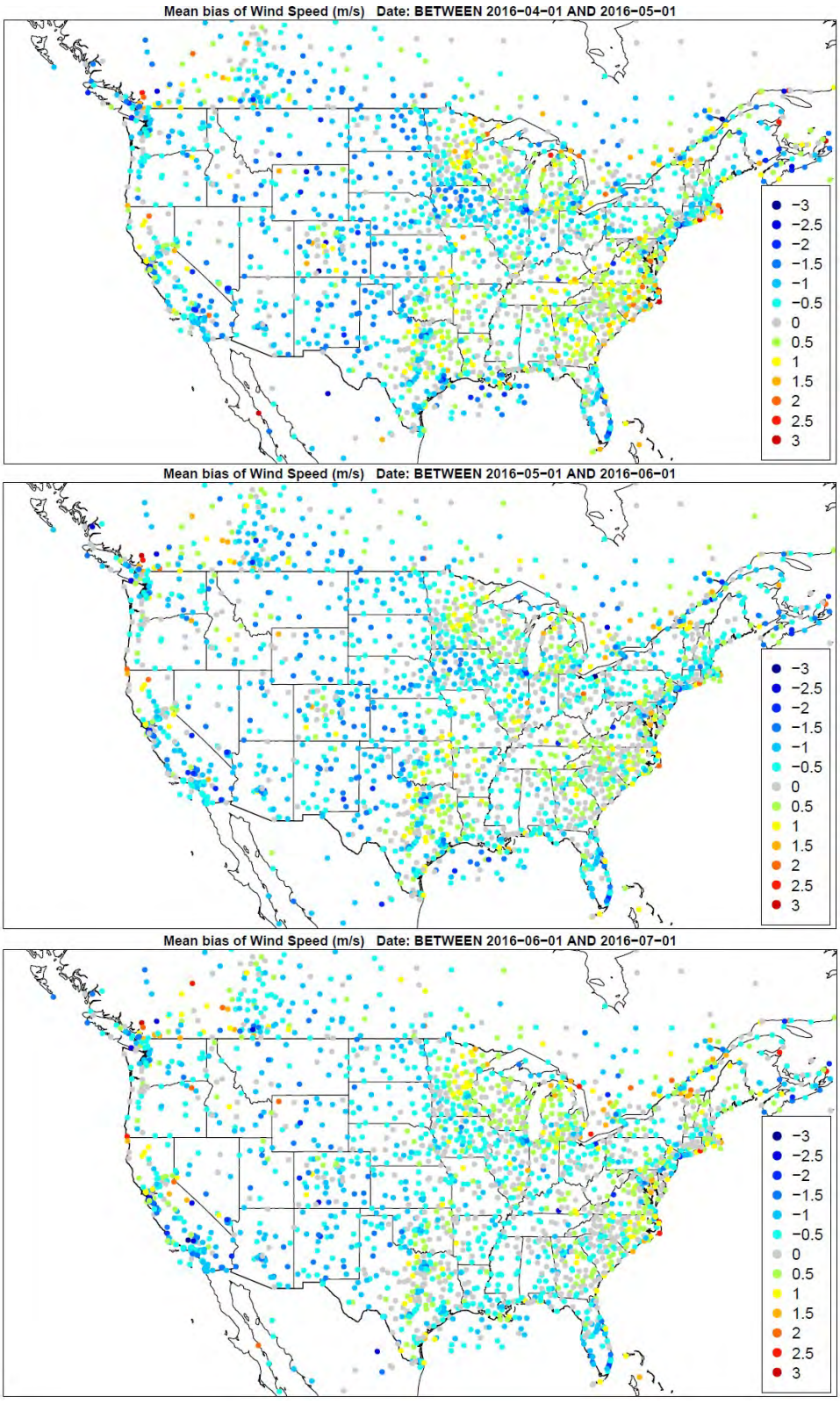

Figure 3.1.8. Spatial distribution of wind speed bias (m/s) across all hours for the months of April, May, and June (top to bottom) for the 12US domain.

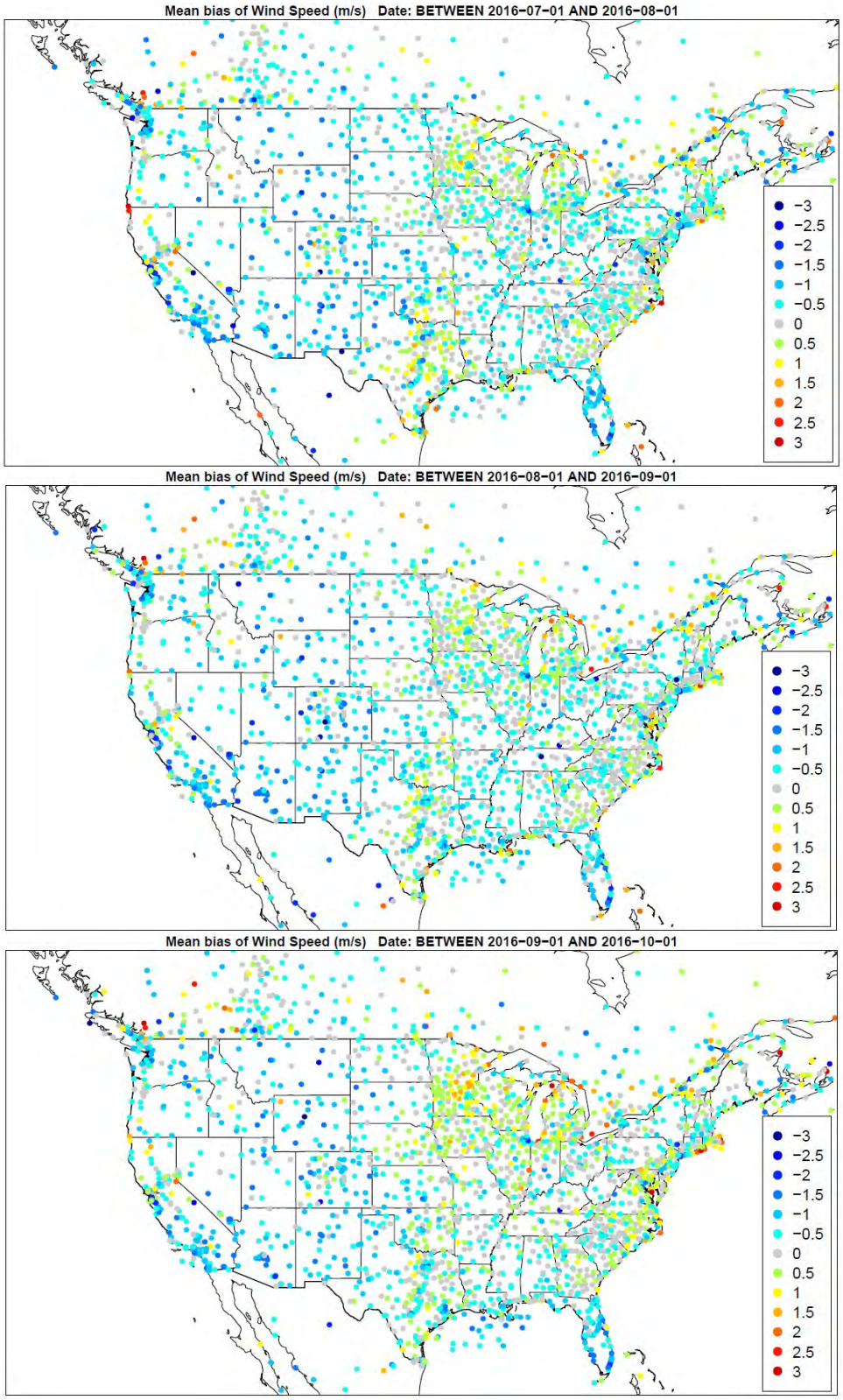

Figure 3.1.9. Spatial distribution of wind speed bias (m/s) across all hours for the months of July, August, and September (top to bottom) for the 12US domain.

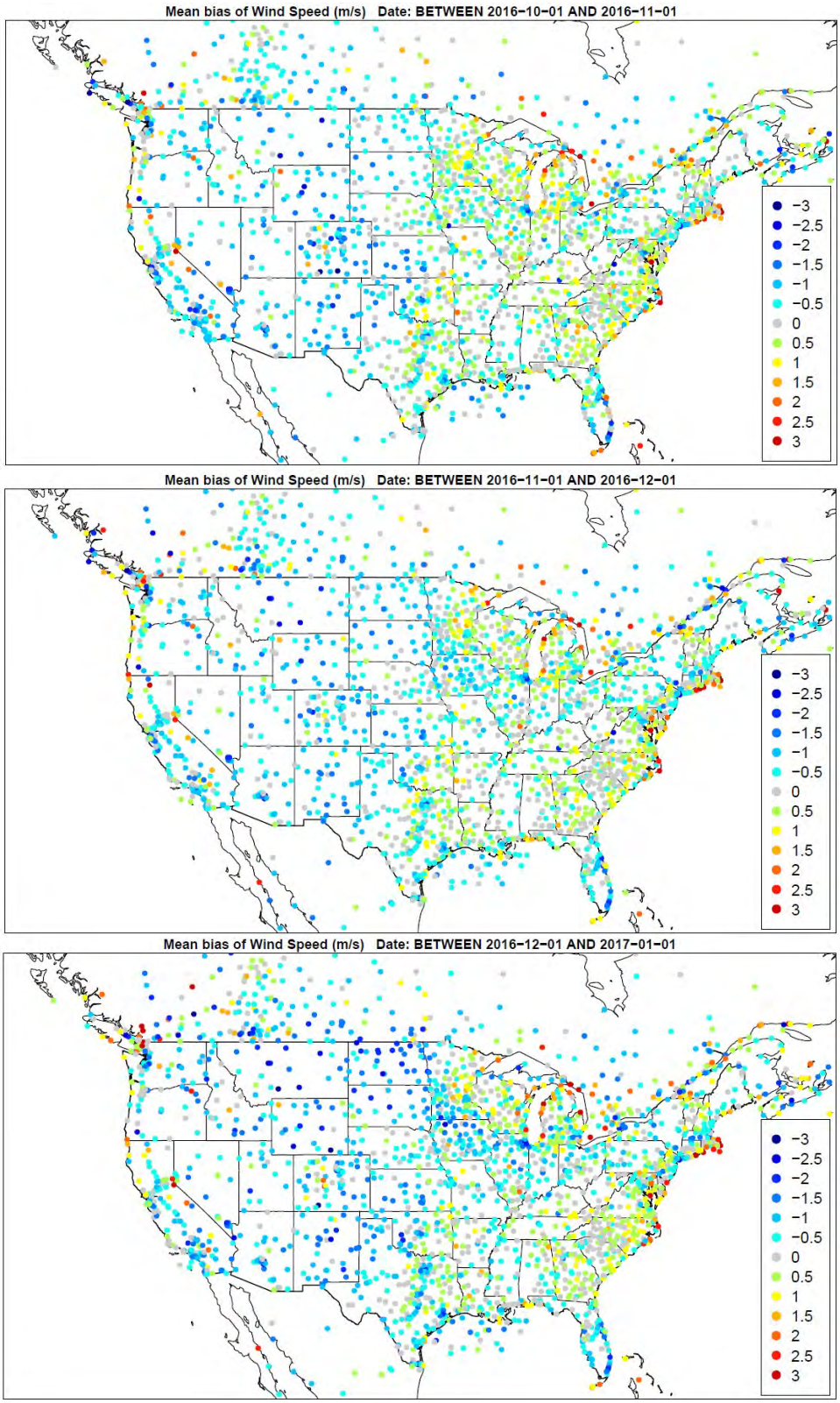

Figure 3.1.10. Spatial distribution of wind speed bias (m/s) across all hours for the months of October, November, and December (top to bottom) for the 12US domain.

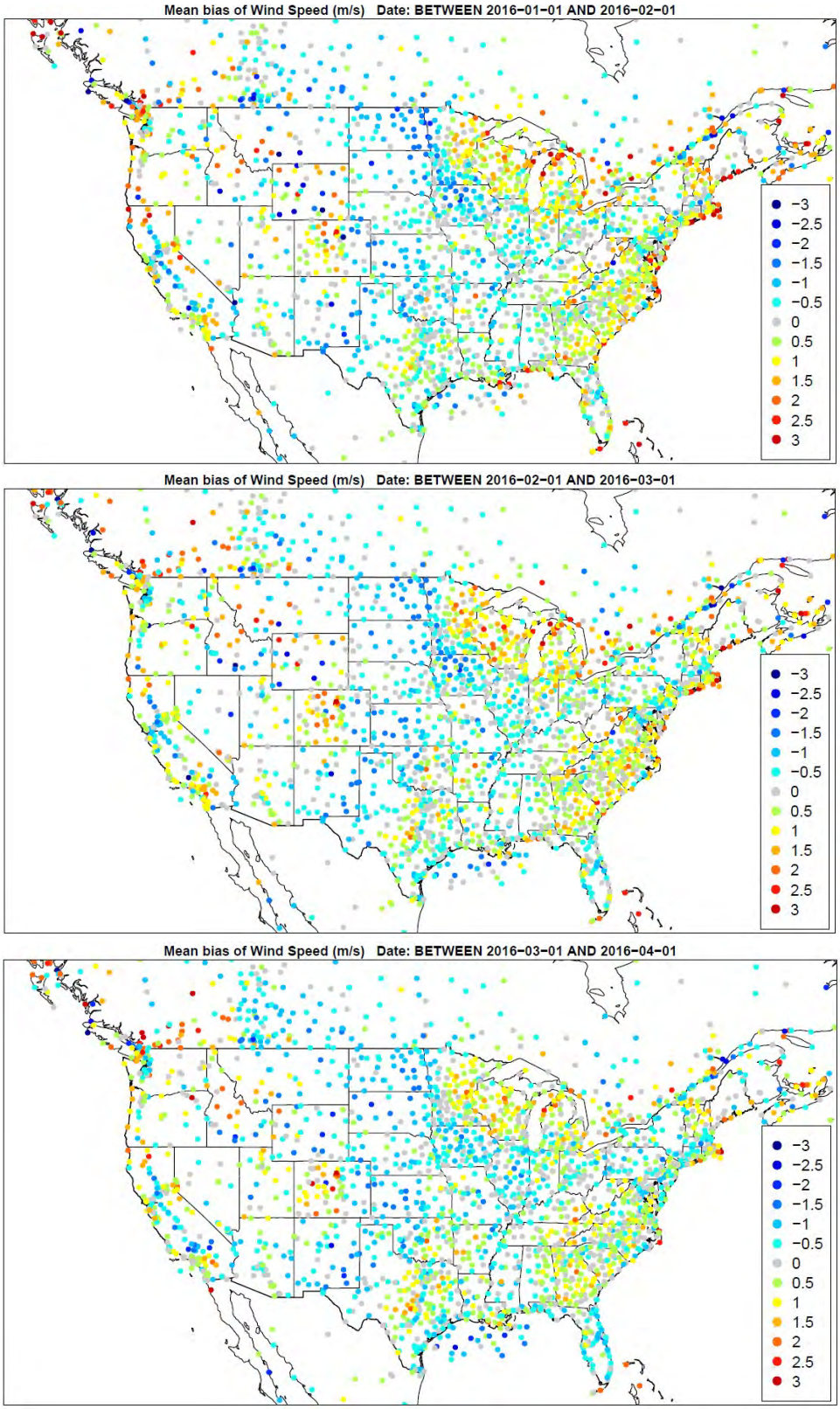

Figure 3.1.11. Spatial distribution of wind speed bias (m/s) across daytime hours for the months of January, February, and March (top to bottom) for the 36NOAM domain.

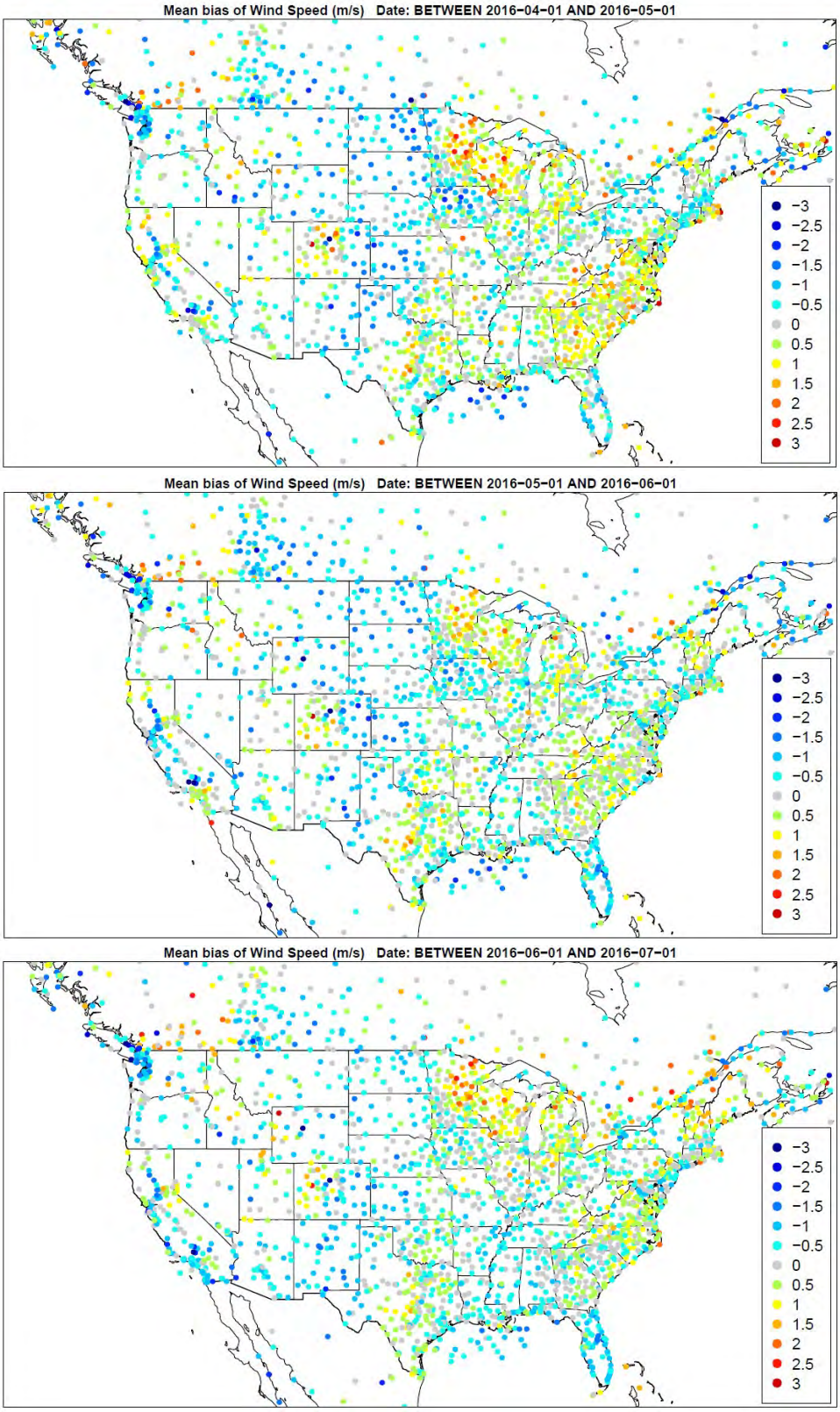

Figure 3.1.12. Spatial distribution of wind speed bias (m/s) across daytime hours for the months of April, May, and June (top to bottom) for the 36NOAM domain.

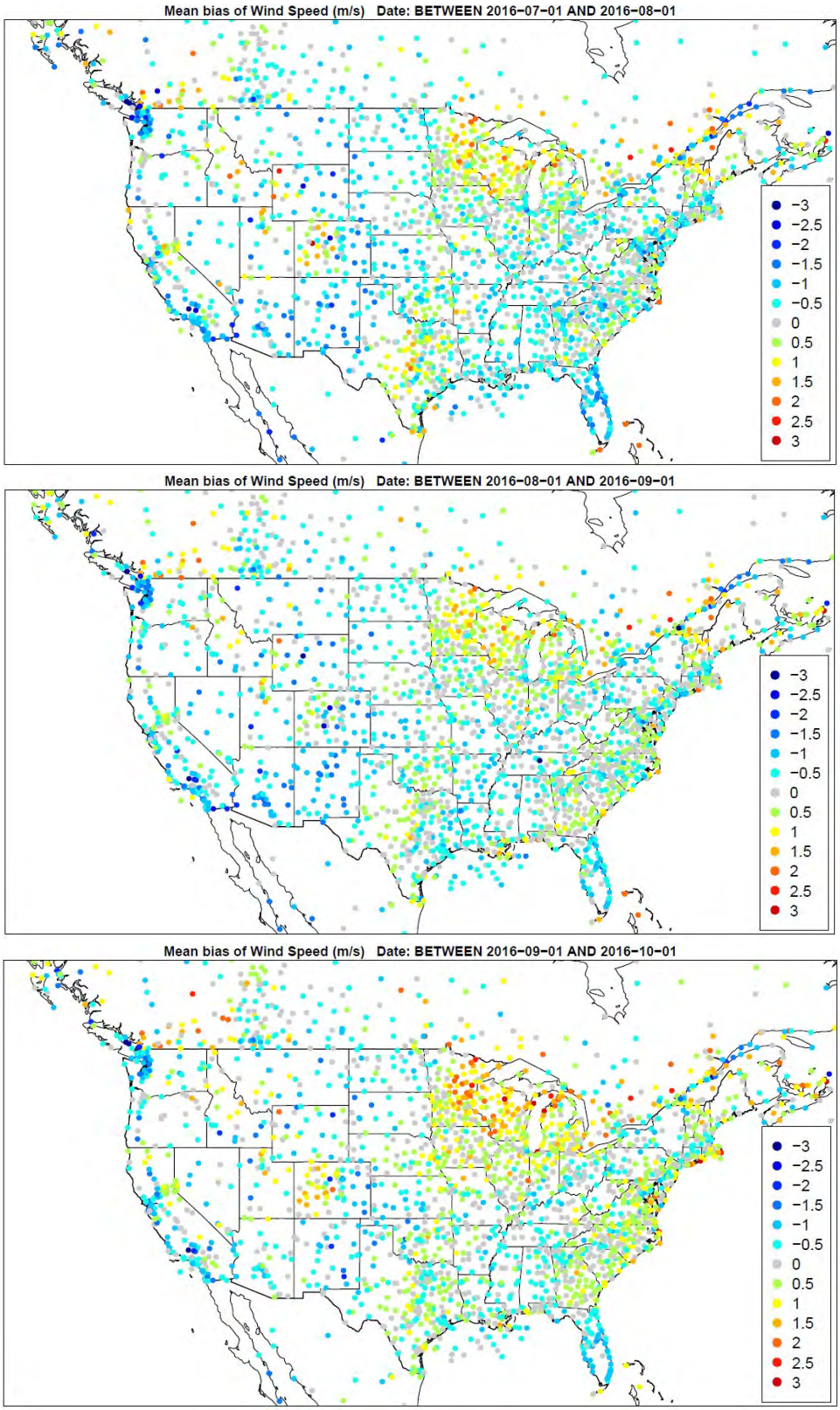

Figure 3.1.13. Spatial distribution of wind speed bias (m/s) across daytime hours for the months of July, August, and September (top to bottom) for the 36NOAM domain.

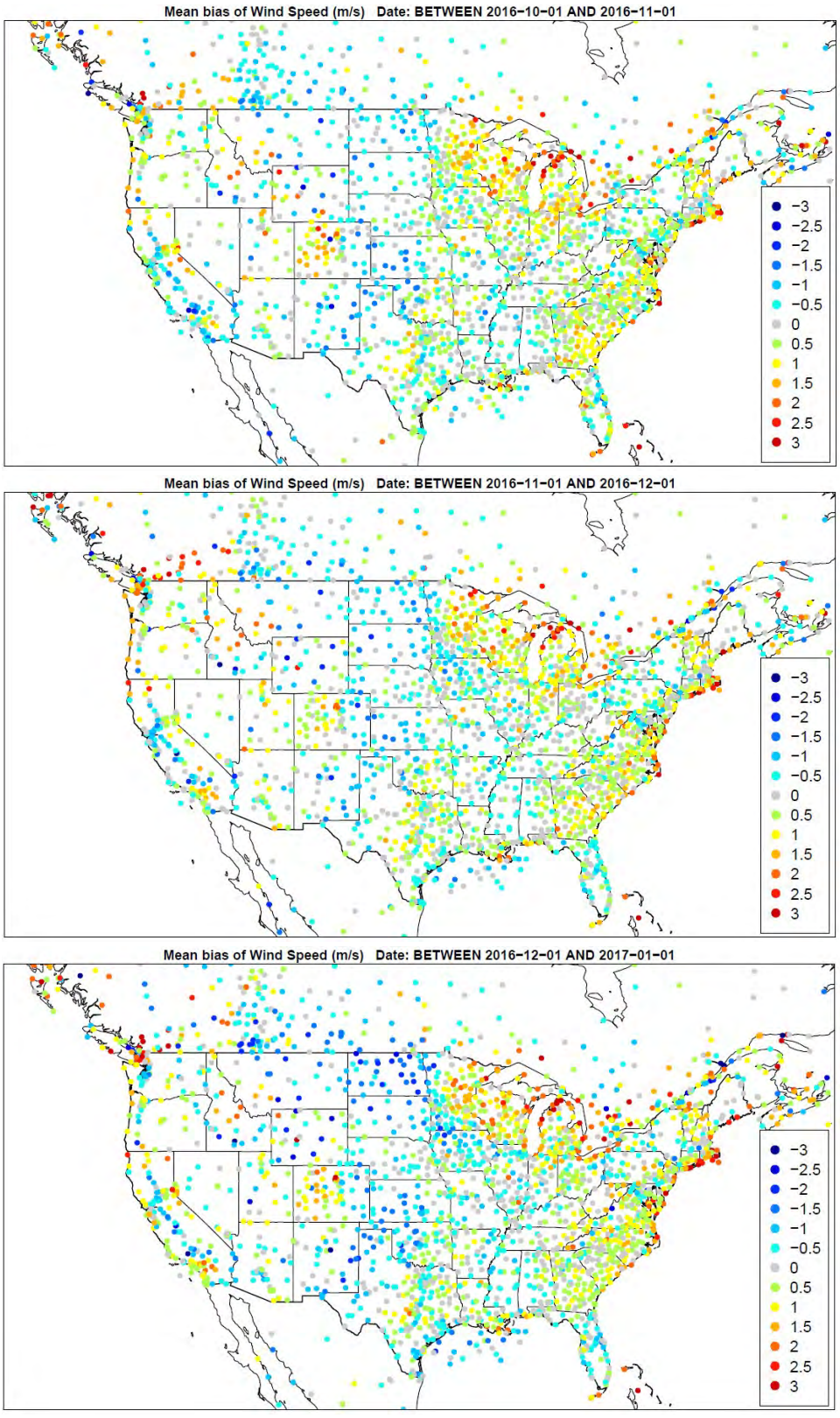

Figure 3.1.14. Spatial distribution of wind speed bias (m/s) across daytime hours for the months of October, November, and December (top to bottom) for the 36NOAM domain.

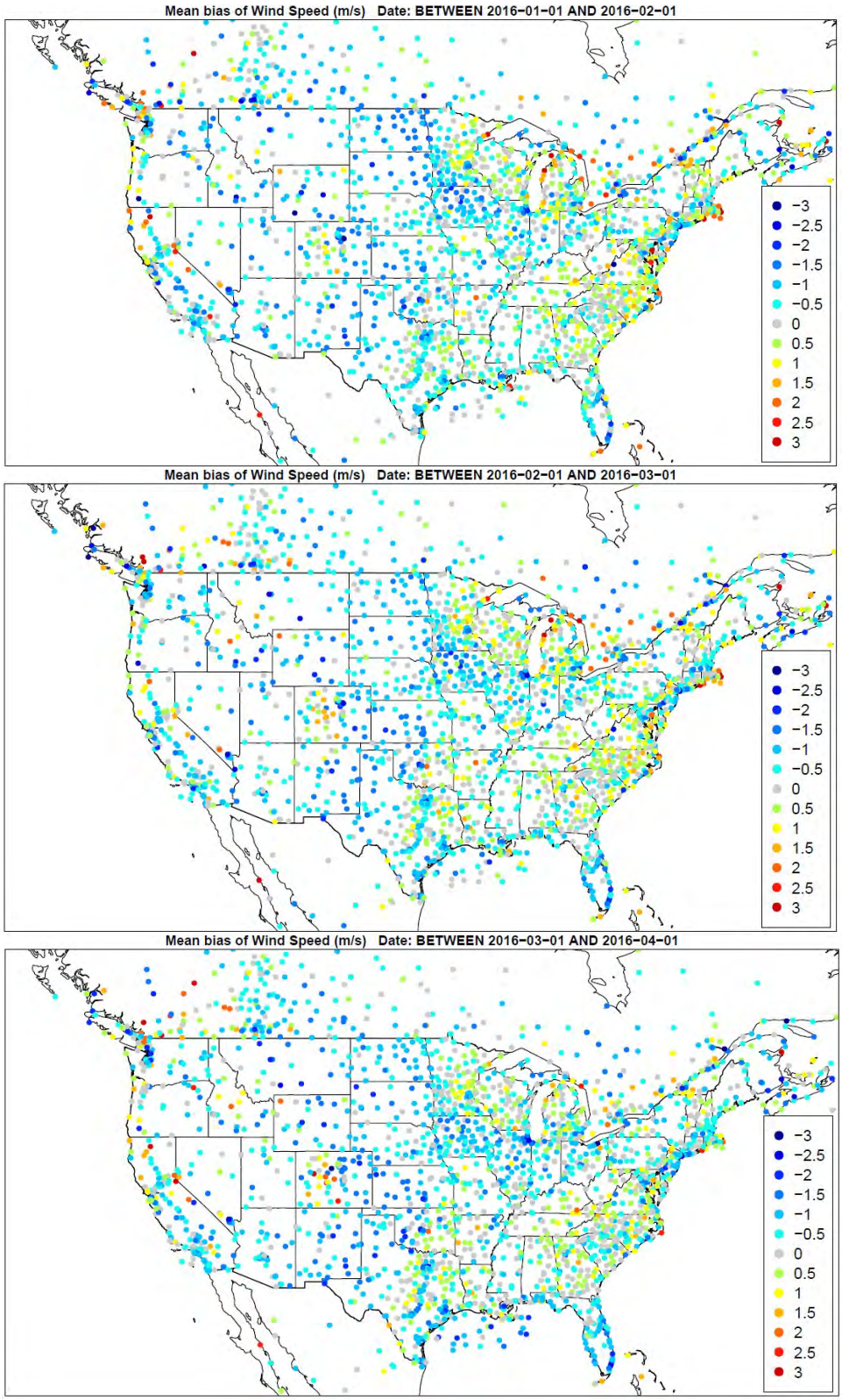

Figure 3.1.15. Spatial distribution of wind speed bias (m/s) across daytime hours for the months of January, February, and March (top to bottom) for the 12US domain.

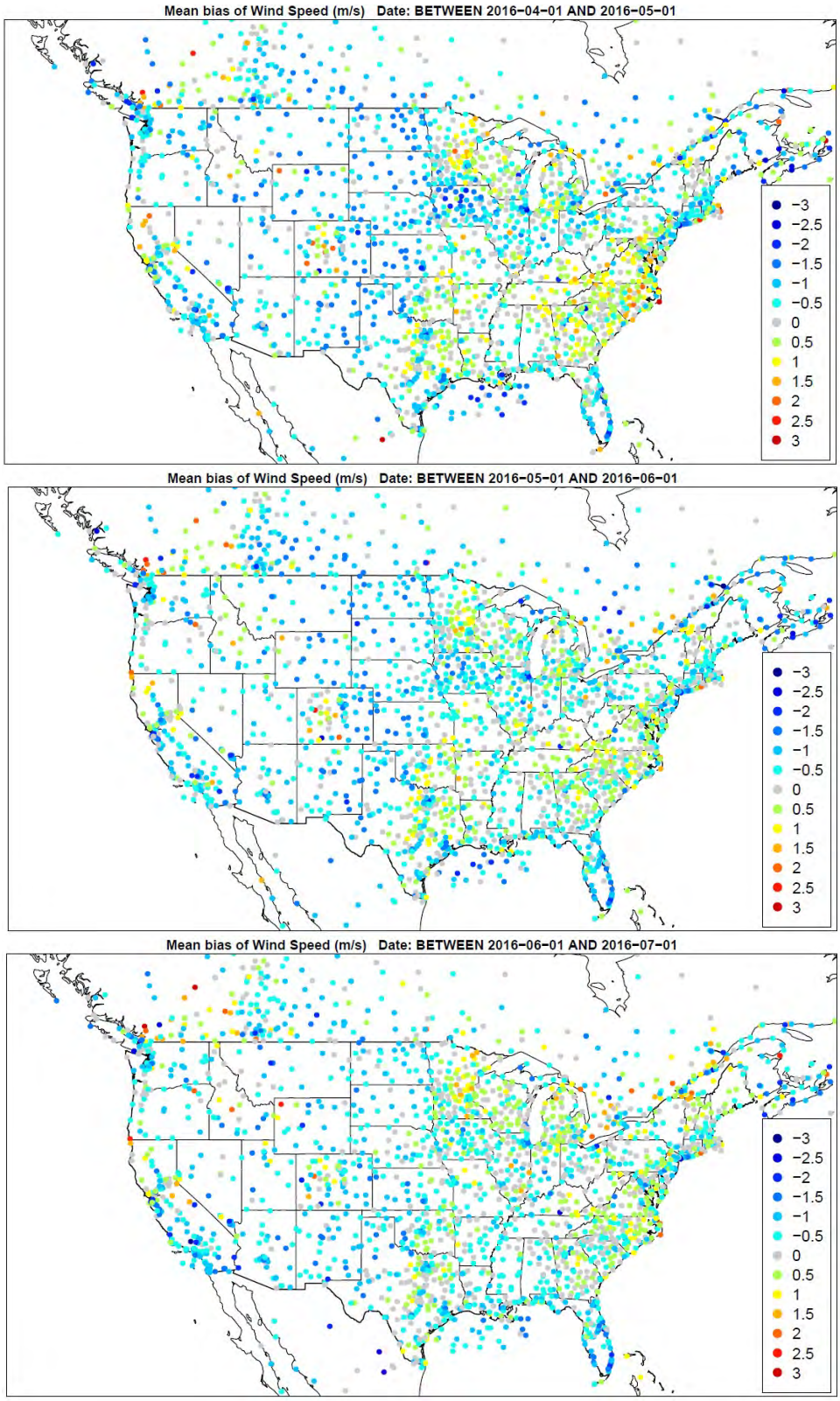

Figure 3.1.16. Spatial distribution of wind speed bias (m/s) across daytime hours for the months of April, May, and June (top to bottom) for the 12US domain.

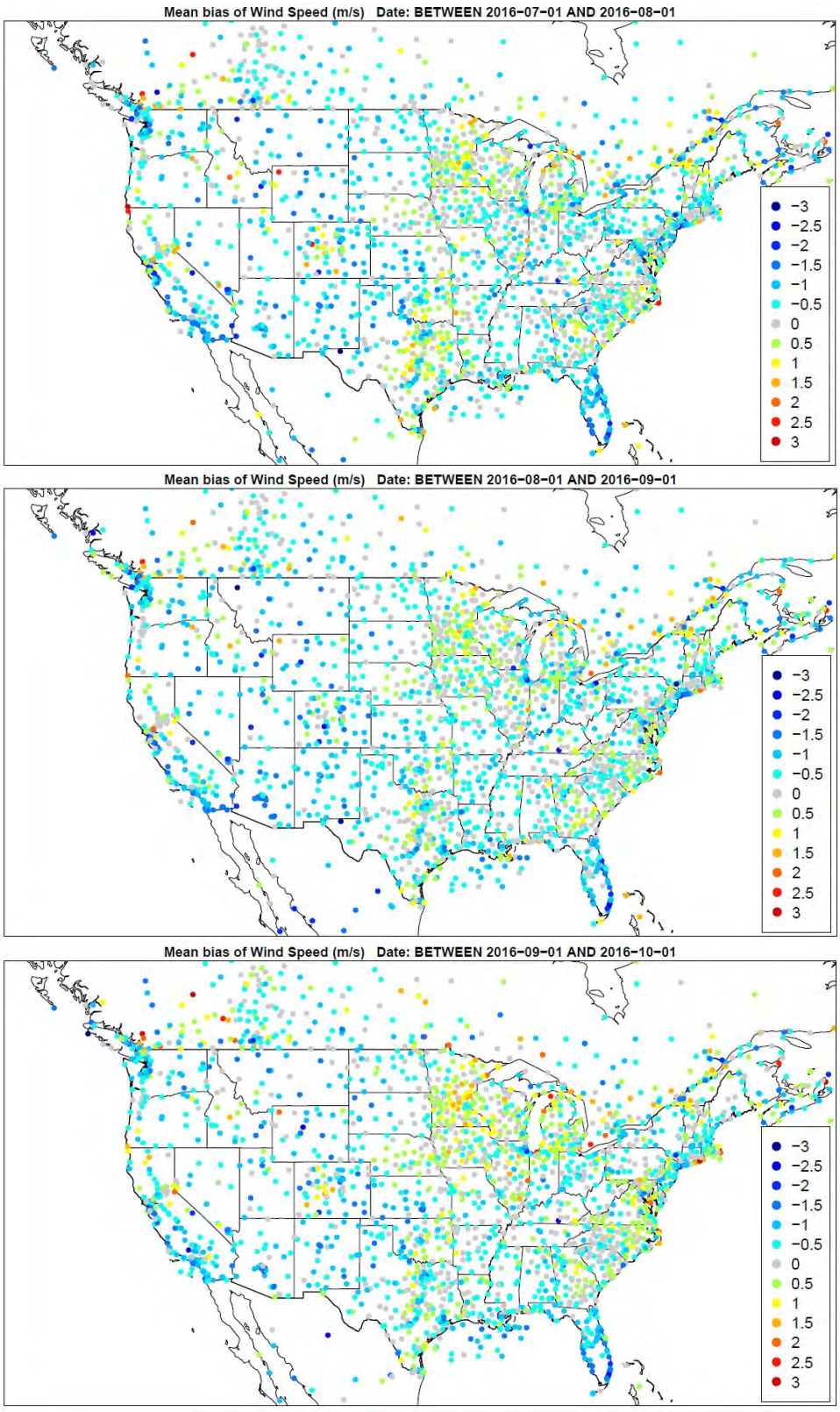

Figure 3.1.17. Spatial distribution of wind speed bias (m/s) across daytime hours for the months of July, August, and September (top to bottom) for the 12US domain.

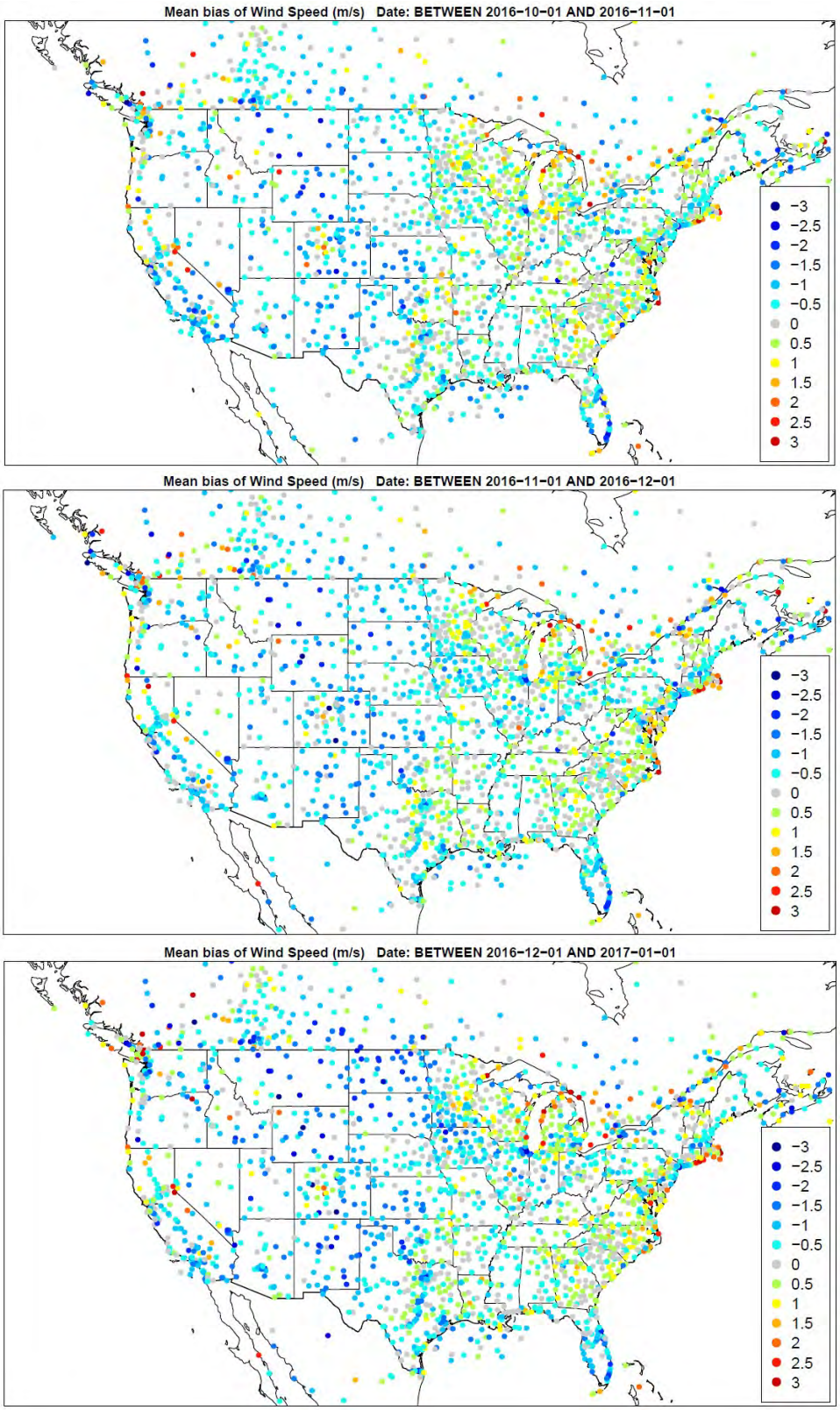

Figure 3.1.18. Spatial distribution of wind speed bias (m/s) across daytime hours for the months of October, November, and December (top to bottom) for the 12US domain.

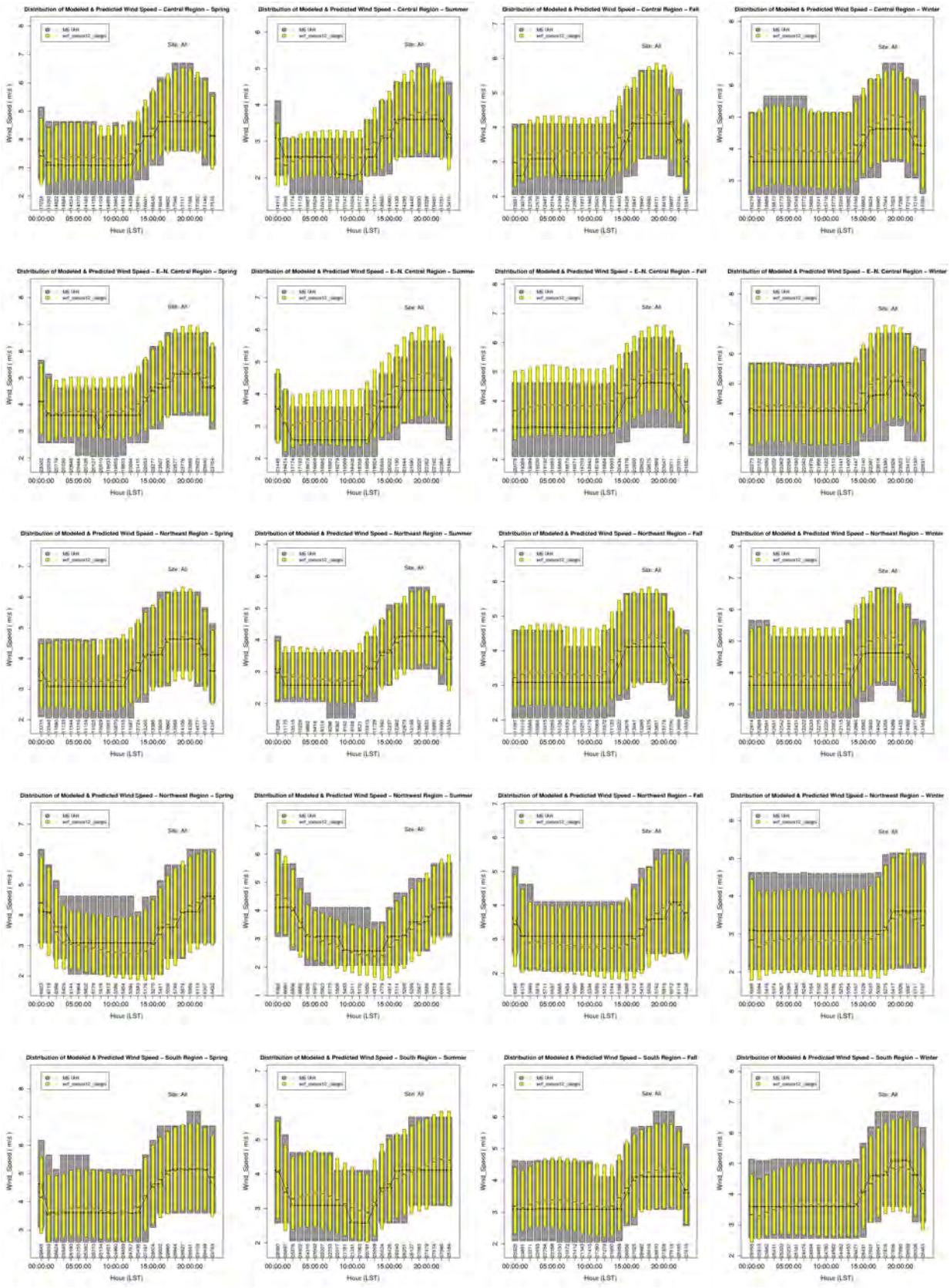
Distribution of Modeled & Predicted Wind Speed – Central Region – Spring
Distribution of Modeled & Predicted Wind Speed – Central Region – Summer
Distribution of Modeled & Predicted Wind Speed – Central Region – Fall
Distribution of Modeled & Predicted Wind Speed – Central Region – Winter
Distribution of Modeled & Predicted Wind Speed – E.-N. Central Region – Spring
Distribution of Modeled & Predicted Wind Speed – E.-N. Central Region – Summer
Distribution of Modeled & Predicted Wind Speed – E.-N. Central Region – Fall
Distribution of Modeled & Predicted Wind Speed – E.-N. Central Region – Winter
Distribution of Modeled & Predicted Wind Speed – Northeast Region – Spring
Distribution of Modeled & Predicted Wind Speed – Northeast Region – Summer
Distribution of Modeled & Predicted Wind Speed – Northeast Region – Fall
Distribution of Modeled & Predicted Wind Speed – Northeast Region – Winter
Distribution of Modeled & Predicted Wind Speed – Northwest Region – Spring
Distribution of Modeled & Predicted Wind Speed – Northwest Region – Summer
Distribution of Modeled & Predicted Wind Speed – Northwest Region – Fall
Distribution of Modeled & Predicted Wind Speed – Northwest Region – Winter
Distribution of Modeled & Predicted Wind Speed – South Region – Spring
Distribution of Modeled & Predicted Wind Speed – South Region – Summer
Distribution of Modeled & Predicted Wind Speed – South Region – Fall
Distribution of Modeled & Predicted Wind Speed – South Region – Winter
Wind_Speed (m/s)
Hour (LST)

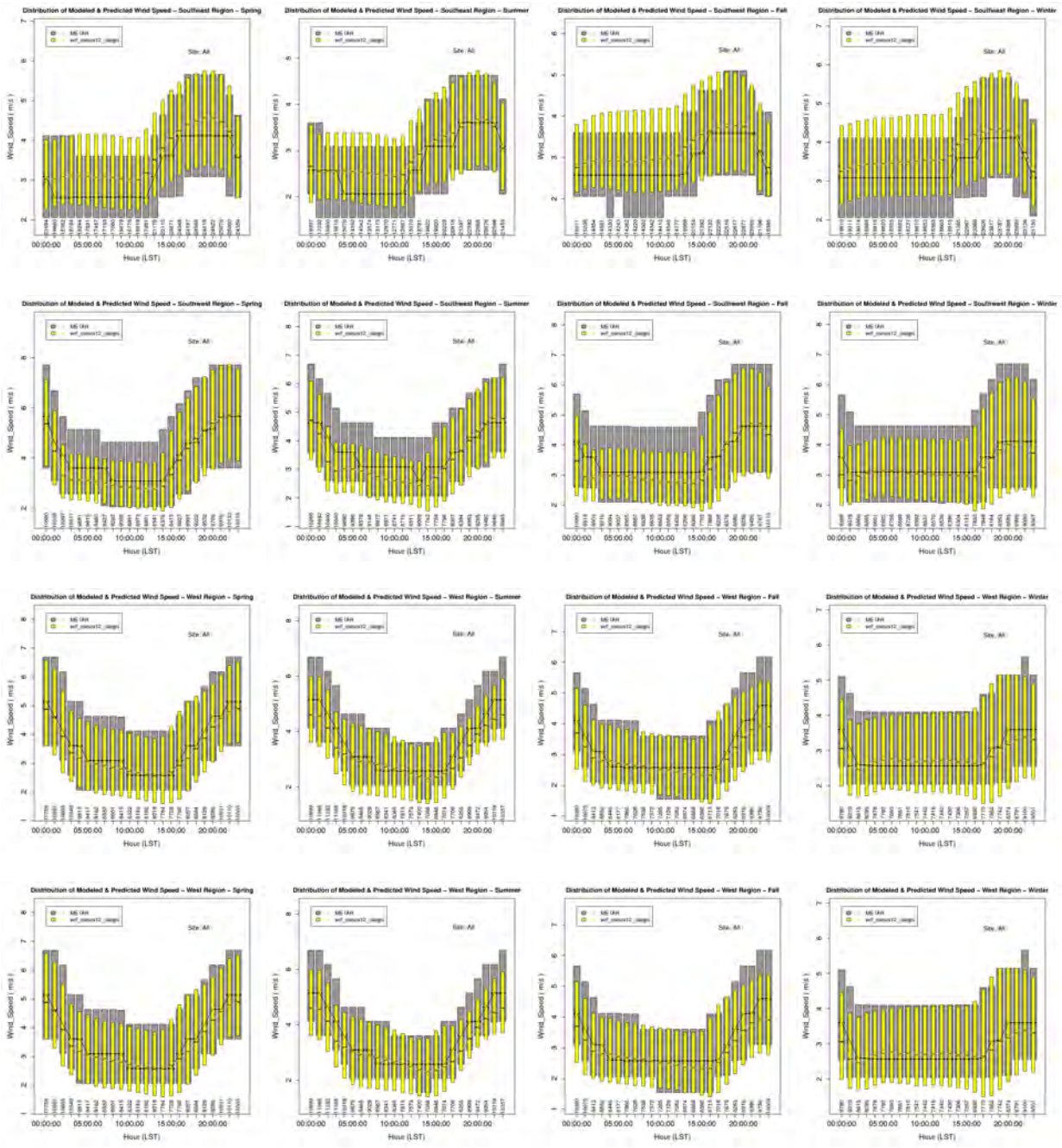

Figure 3.1.19. Hourly average distribution of observed and predicted wind speeds for the 12US domain in the Central, East-North Central, Northeast, Northwest, South, Southeast, Southwest, West, and West-North Central (top to bottom) regions for each season (Spring, Summer, Fall, Winter, L-R).

Climate Region	Season	Mean Obs	Mean Mod	MB	MAE	NMB	NME	RMSE
Northeast	Spring	5.09	5.69	0.60	0.82	11.79	16.12	1.09
Northeast	Summer	11.95	12.12	0.17	1.05	1.42	8.79	1.45
Northeast	Fall	7.35	7.54	0.19	0.70	2.57	9.47	0.96
Northeast	Winter	2.74	3.14	0.40	0.51	14.55	18.50	0.71
West-North Central	Spring	4.77	4.89	0.12	0.63	2.50	13.16	0.87
West-North Central	Summer	9.97	10.14	0.18	1.19	1.77	11.97	1.64
West-North Central	Fall	5.85	5.87	0.02	0.65	0.36	11.12	0.91
West-North Central	Winter	2.34	2.45	0.10	0.34	4.44	14.68	0.47
Northwest	Spring	5.37	5.45	0.09	0.65	1.61	12.15	0.87
Northwest	Summer	7.07	7.06	-0.01	0.83	-0.11	11.77	1.14
Northwest	Fall	6.05	6.11	0.06	0.68	0.92	11.25	0.89
Northwest	Winter	3.87	4.09	0.22	0.49	5.80	12.59	0.64
Central	Spring	6.72	7.23	0.50	0.88	7.51	13.15	1.20
Central	Summer	14.81	15.07	0.25	1.25	1.71	8.46	1.70
Central	Fall	8.74	8.64	-0.10	0.80	-1.13	9.10	1.08
Central	Winter	3.20	3.42	0.22	0.45	6.77	14.22	0.63
South	Spring	9.53	9.74	0.21	1.02	2.22	10.68	1.45
South	Summer	16.37	16.44	0.07	1.41	0.40	8.61	1.98
South	Fall	11.21	10.94	-0.27	1.05	-2.43	9.34	1.48
South	Winter	5.14	5.03	-0.10	0.63	-2.02	12.20	0.88
Southeast	Spring	9.15	9.35	0.20	0.97	2.16	10.57	1.31
Southeast	Summer	16.55	16.71	0.17	1.45	1.00	8.74	1.91
Southeast	Fall	10.81	10.67	-0.14	1.06	-1.31	9.80	1.43
Southeast	Winter	5.62	5.69	0.07	0.70	1.29	12.50	0.98
Southwest	Spring	3.93	4.09	0.16	0.68	4.08	17.40	0.95
Southwest	Summer	7.94	8.41	0.46	1.34	5.85	16.91	1.81
Southwest	Fall	5.37	5.55	0.17	0.84	3.23	15.67	1.17
Southwest	Winter	2.88	2.94	0.06	0.50	2.25	17.45	0.68
East-North Central	Spring	5.05	5.47	0.42	0.71	8.39	14.07	1.01
East-North Central	Summer	12.11	12.42	0.32	1.10	2.62	9.08	1.53
East-North Central	Fall	7.30	7.35	0.05	0.64	0.68	8.74	0.88
East-North Central	Winter	2.32	2.43	0.11	0.29	4.54	12.54	0.39
West	Spring	6.22	6.20	-0.02	0.78	-0.34	12.54	1.14
West	Summer	7.67	7.84	0.17	1.08	2.23	14.04	1.55
West	Fall	6.43	6.54	0.10	0.95	1.60	14.79	1.34
West	Winter	5.02	4.93	-0.08	0.71	-1.68	14.12	0.98

Table 3.1.1. Mean observed, mean modeled, mean bias (MB), mean absolute error (MAE), normalized mean bias (NMB), normalized mean error (NME), and root mean square error (RMSE) for wind speed (m/s) for the 12US simulation.

Wind vector displacement (km) is presented below for the 36NOAM (Figure 3.1.20) and 12US (Figure 3.1.21) domains utilizing the ds472 observation network described earlier. These plots show the entire distribution of hourly wind displacement by month and by hour of the day. Overall, model performance is adequate in terms of wind vector differences. The average wind displacement for the WRF simulation is around 5km for all months and hours of the day. The interquartile ranges are roughly 2-10km. As the displacement is generally less than the resolution of the model, minimal impacts due to displacement of wind vectors are expected.

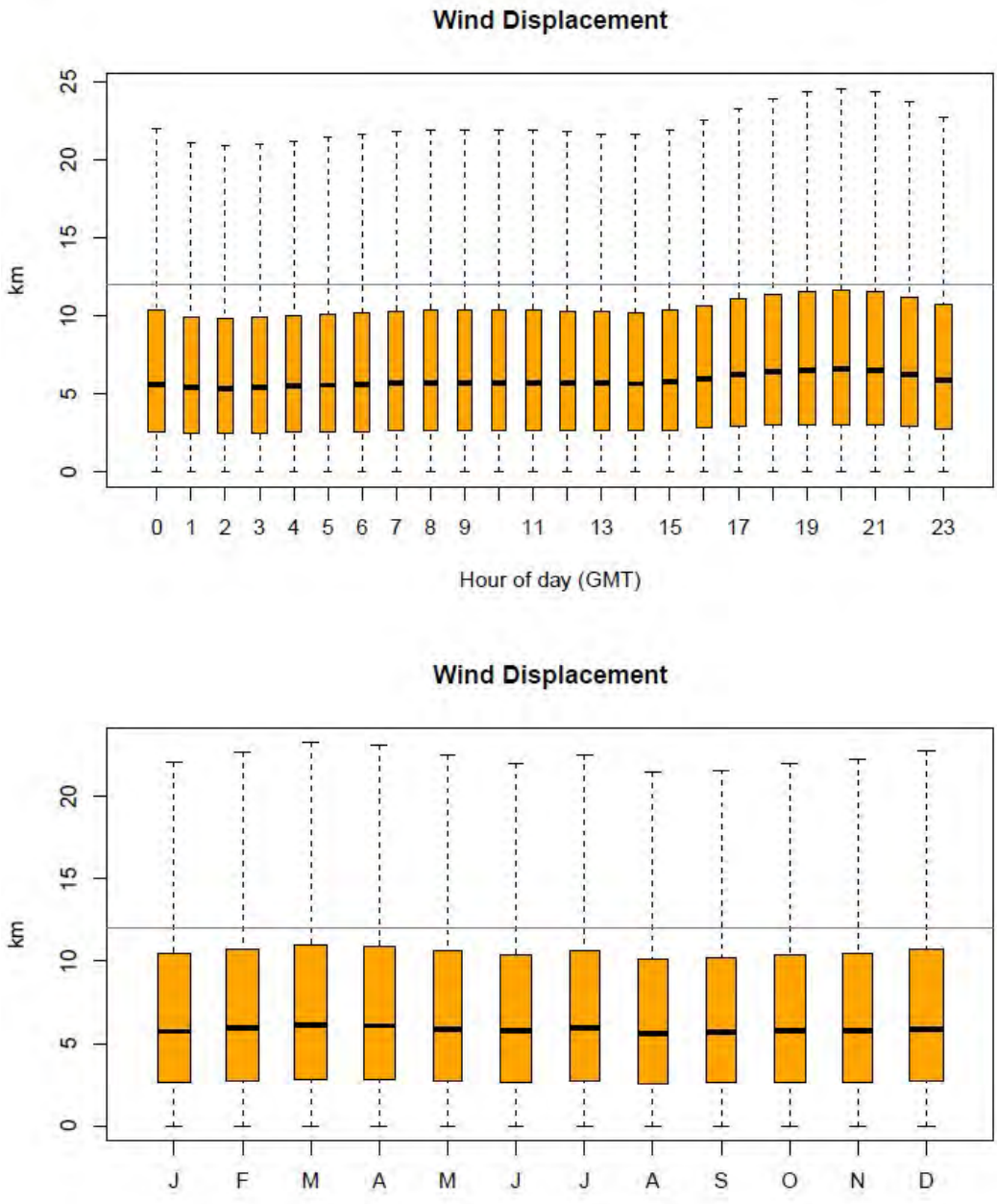

Figure 3.1.20. Distribution of hourly wind displacement by hour and month for the 36NOAM domain.

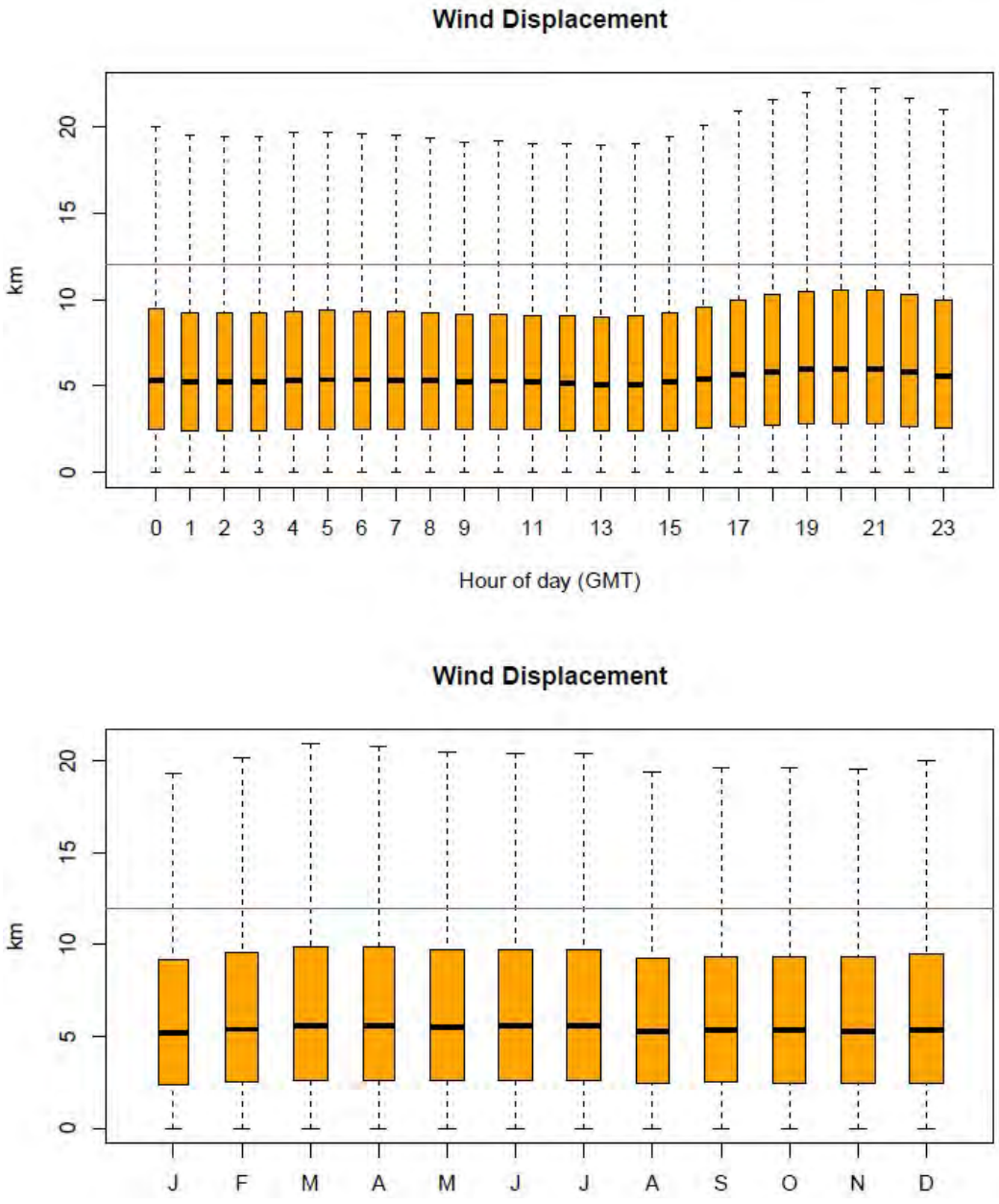

Figure 3.1.21. Distribution of hourly wind displacement by hour and month for the 12US domain.

3.2 Temperature

Temperature estimates are compared to the ds472 observation network described earlier and are presented below for the 36NOAM (Figure 3.2.1) and 12US (Figure 3.2.2) domains.

Overall, WRF slightly underpredicts temperatures at both 36km and 12km across most hours and months, with a small underprediction during the mid-afternoon hours. The range of biases decreases slightly during the summer months compared to the rest of the year, with the inner-quartile range (IQR) becoming more tightly centered around zero. Overall, with an average IQR of +/- 1 degree, this is considered adequate model performance.

In Figures 3.2.3-3.2.6 and 3.2.7-3.2.10, spatial distribution of monthly biases is presented across all hours for the 36km and 12km simulations, respectively. In 3.2.11-3.2.14 and 3.2.15-3.2.18, the monthly spatial distributions of the temperature bias for the 36km and 12km simulations is presented for daytime hours only, respectively. Additionally, the hourly average distribution of observed and predicted temperatures for each season and region is presented in Figure 3.2.19. Overall, a persistent slight underprediction of temperature is noted for most of the year, with a transition to a slight overprediction in some areas during the summer months. A more persistent underprediction of temperature is noted during daytime hours specifically, with a slight improvement in that underprediction observed during the summer months. In areas of the western US, performance for temperature is mixed, with persistent significant overpredictions and underpredictions observed in varying locations.

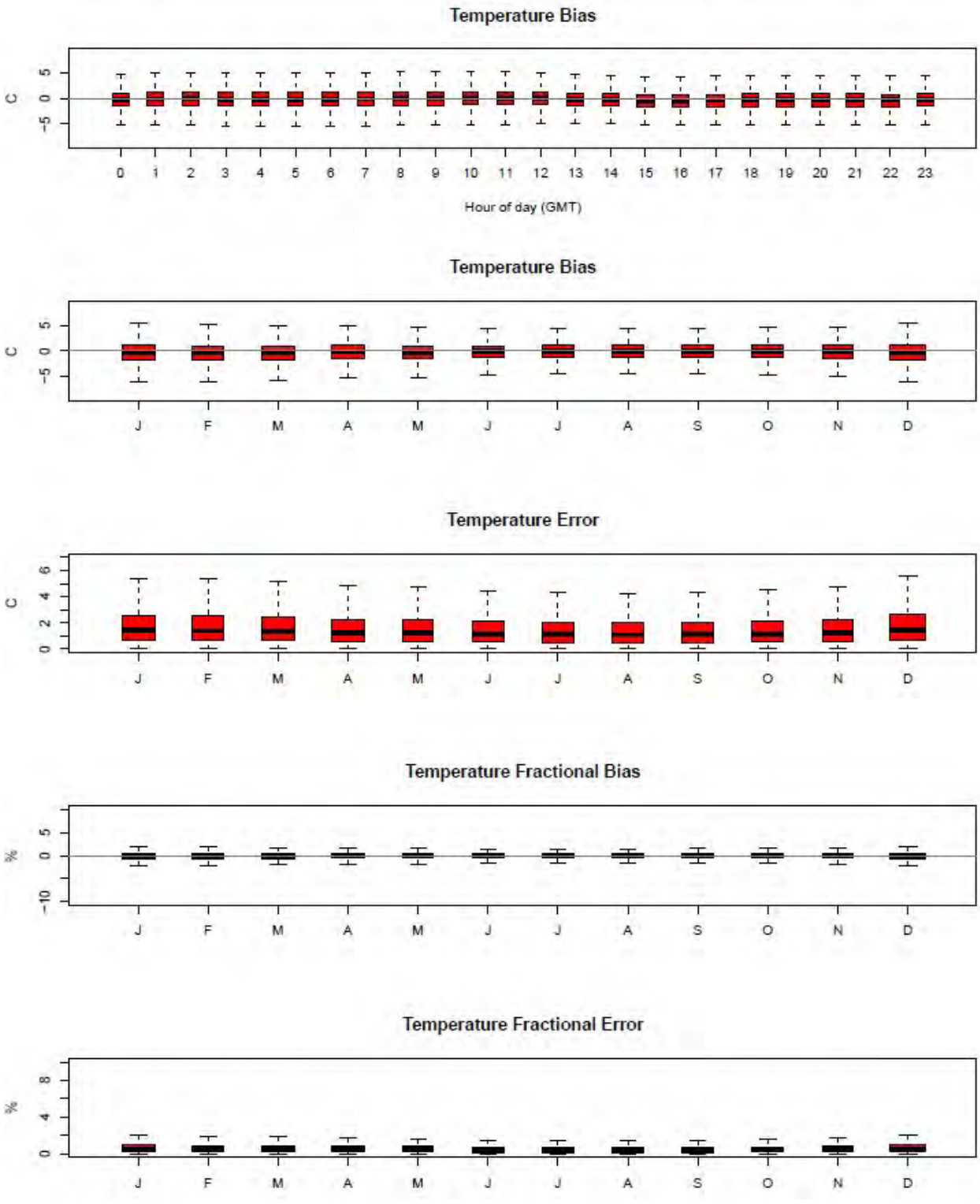

Figure 3.2.1. Distribution of hourly bias by hour and hourly bias, error, fractional bias, and fractional error for temperature by month for the 36NOAM domain.

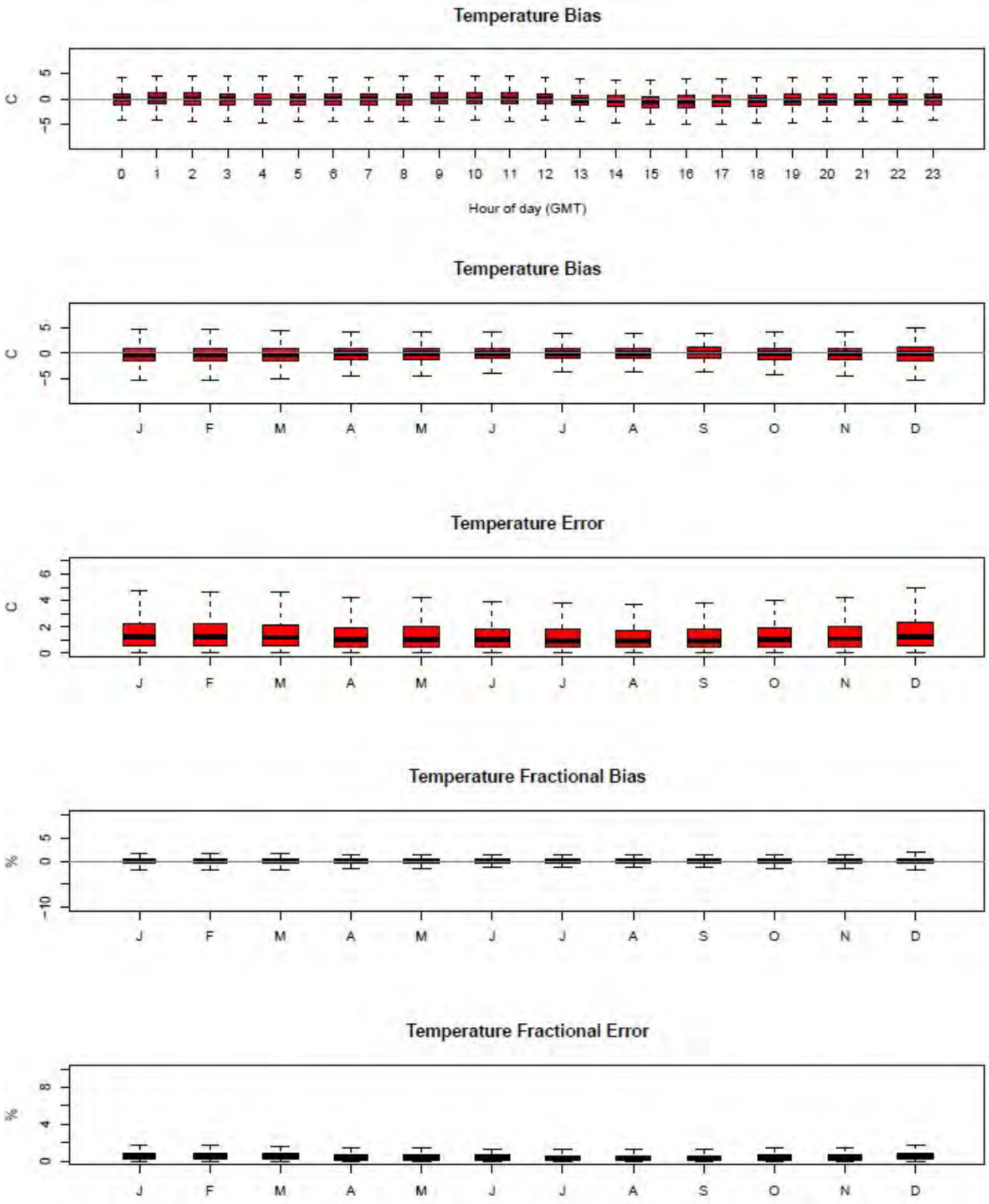

Figure 3.2.2. Distribution of hourly bias by hour and hourly bias, error, fractional bias, and fractional error for temperature by month for the 12US domain.

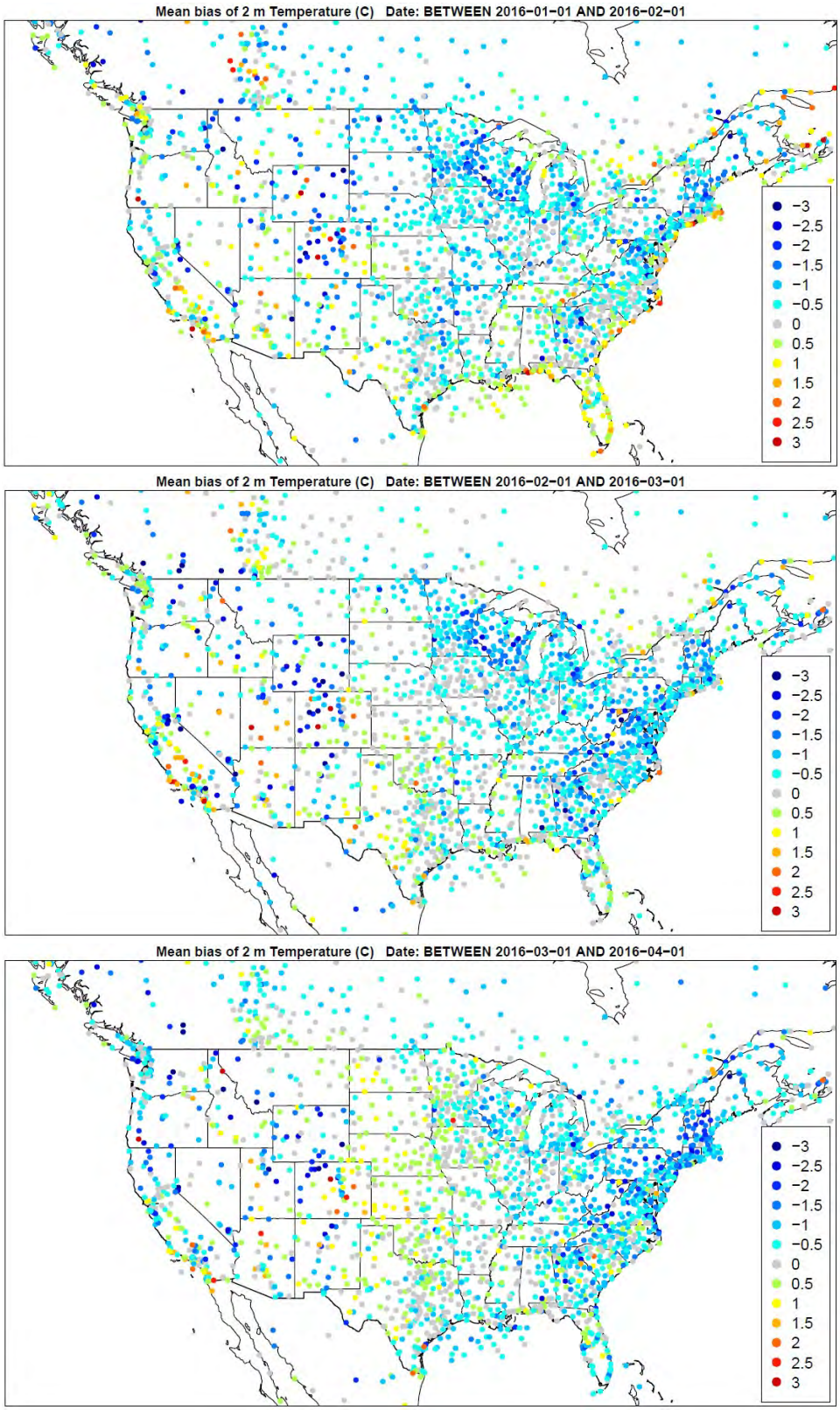

Figure 3.2.3. Spatial distribution of temperature bias (C) across all hours for the months of January, February, and March (top to bottom) for the 36NOAM domain.

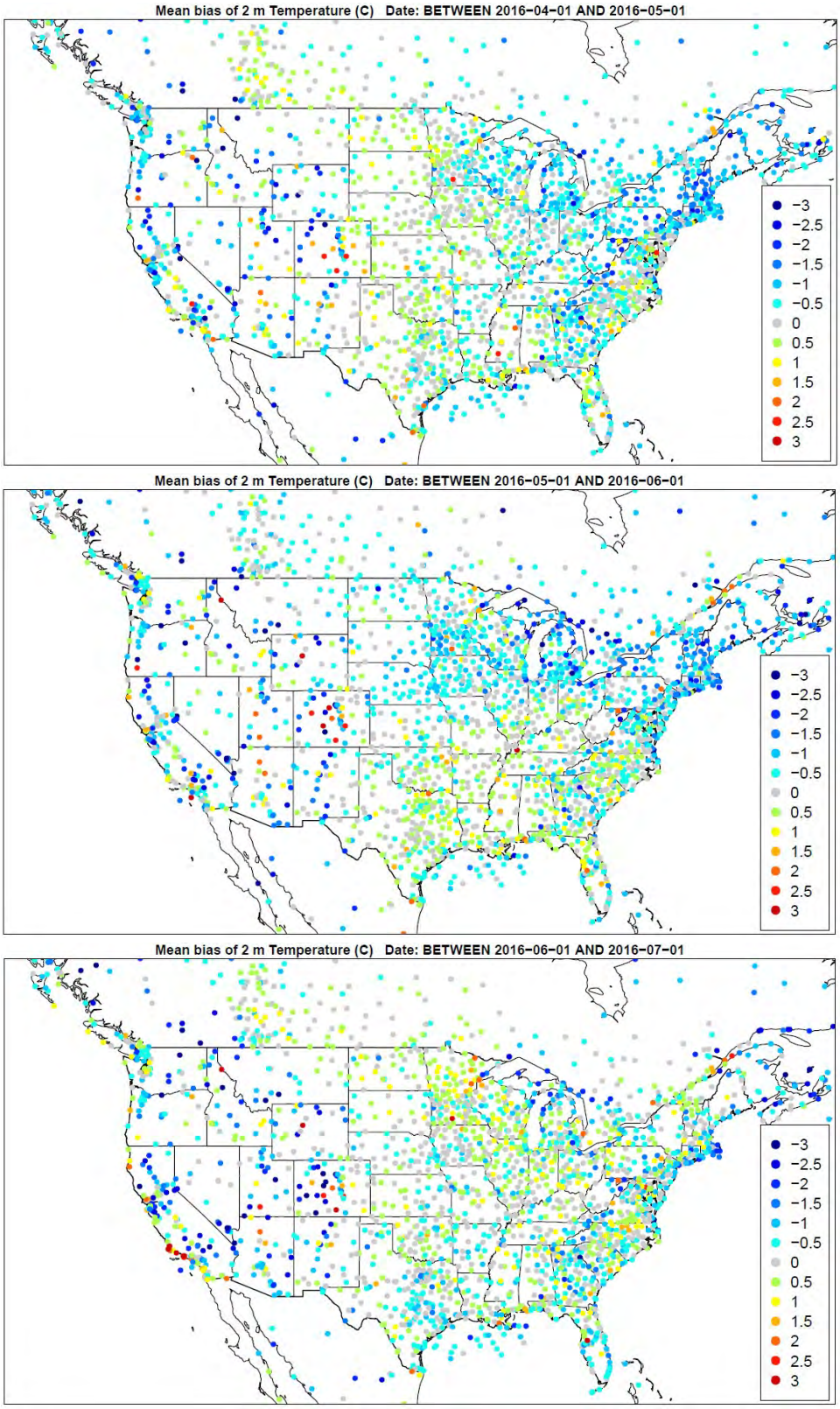

Figure 3.2.4. Spatial distribution of temperature bias (C) across all hours for the months of April, May, and June (top to bottom) for the 36NOAM domain.

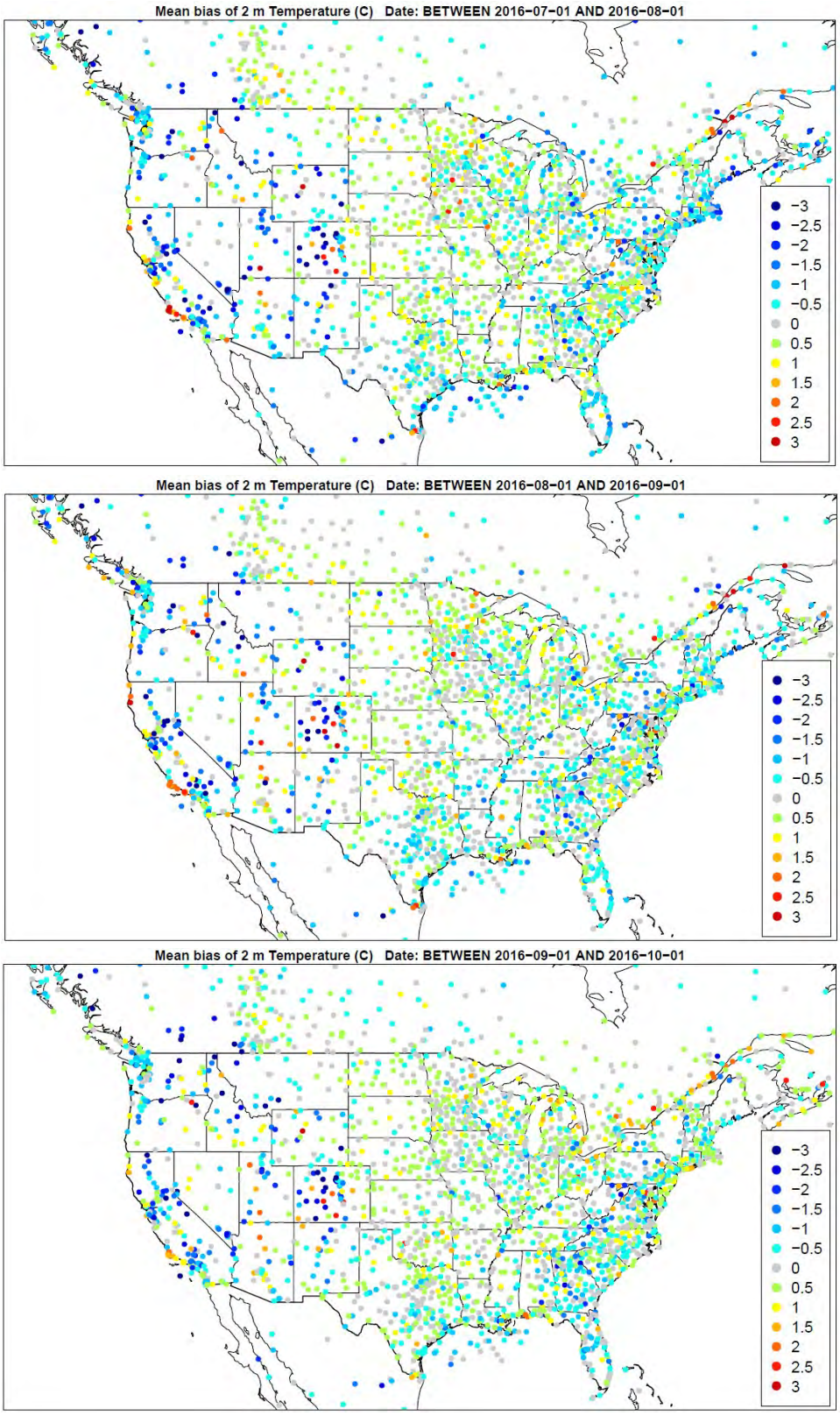

Figure 3.2.5. Spatial distribution of temperature bias (C) across all hours for the months of July, August, and September (top to bottom) for the 36NOAM domain.

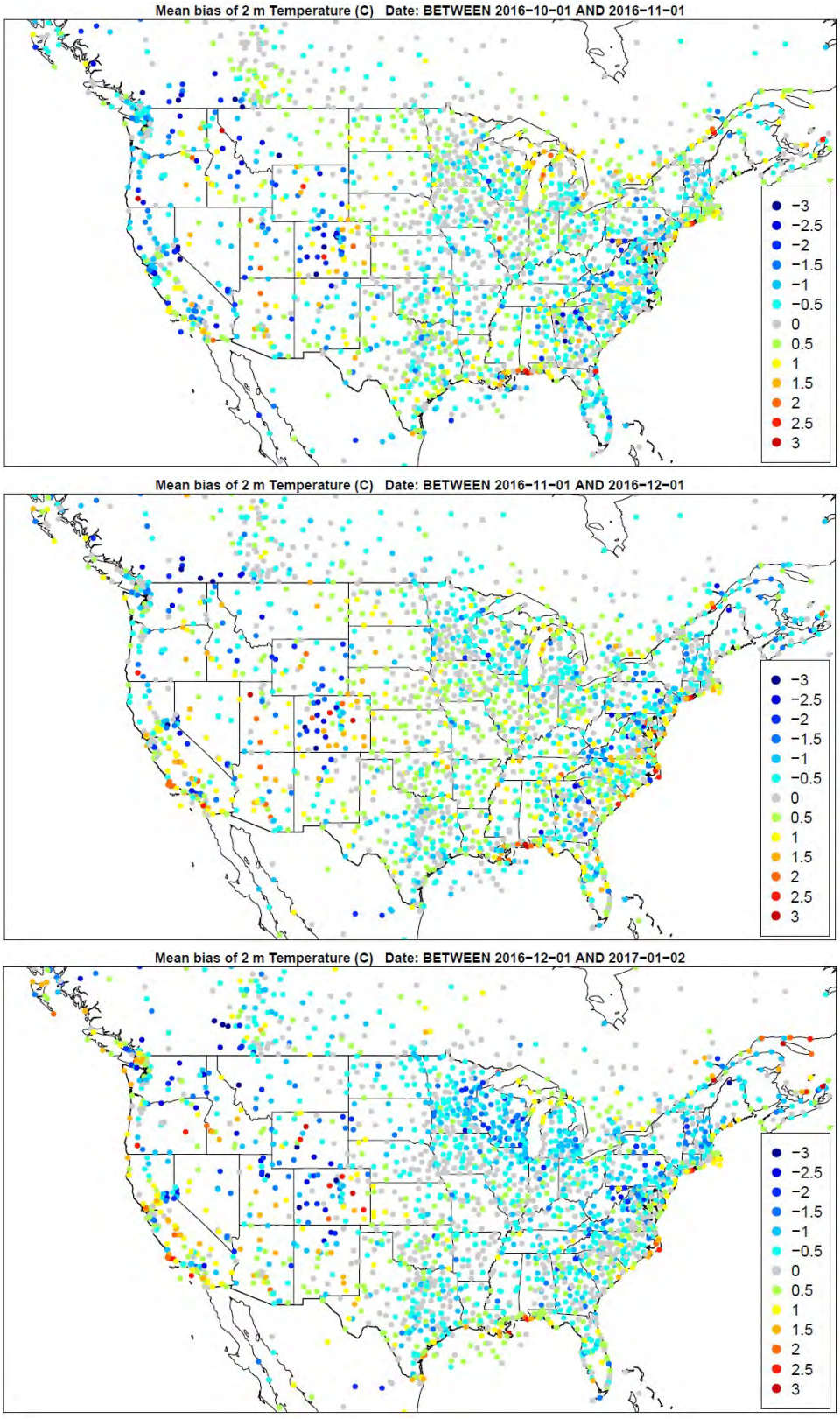

Figure 3.2.6. Spatial distribution of temperature bias (C) across all hours for the months of October, November, and December (top to bottom) for the 36NOAM domain.

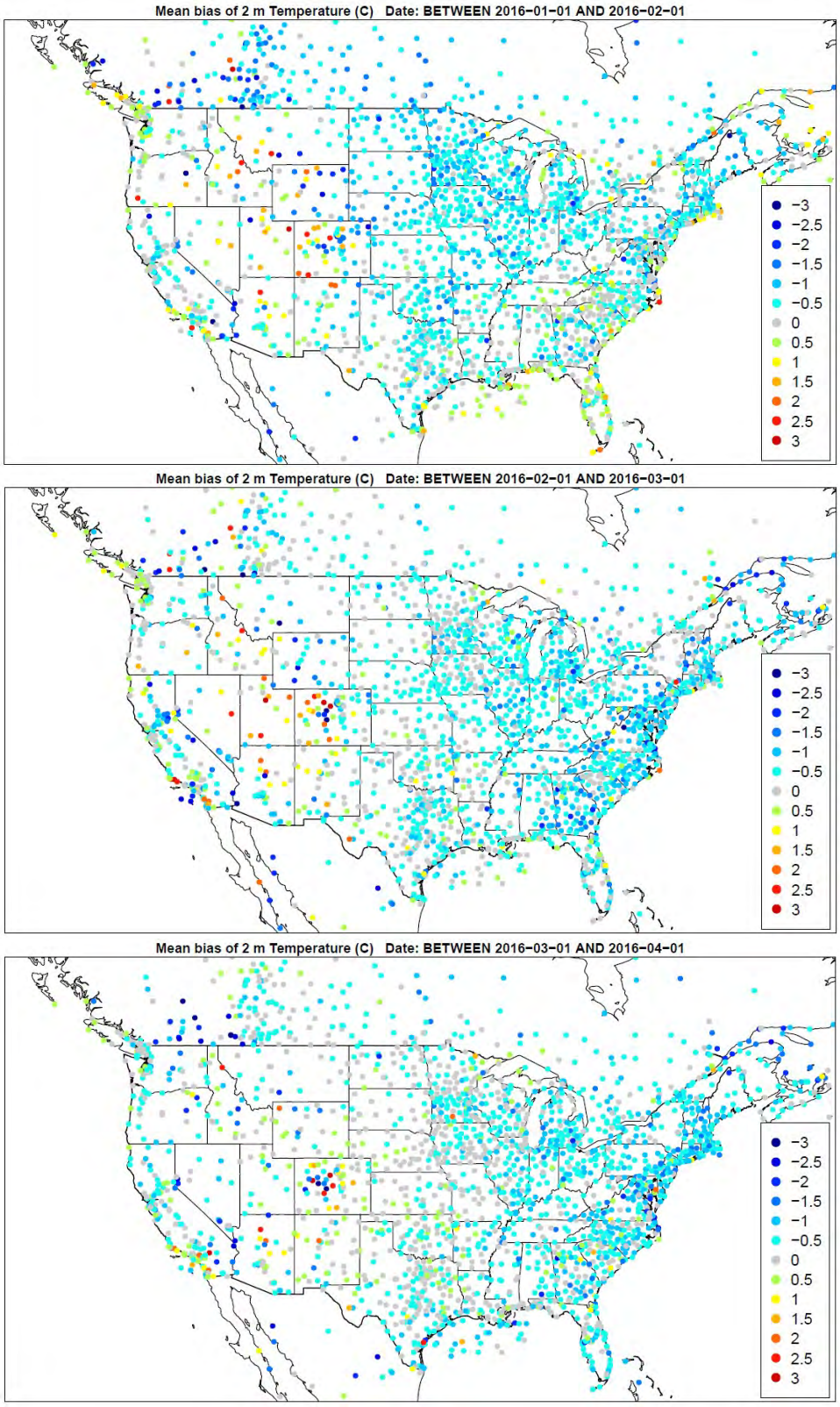

Figure 3.2.7. Spatial distribution of temperature bias (C) across all hours for the months of January, February, and March (top to bottom) for the 12US domain.

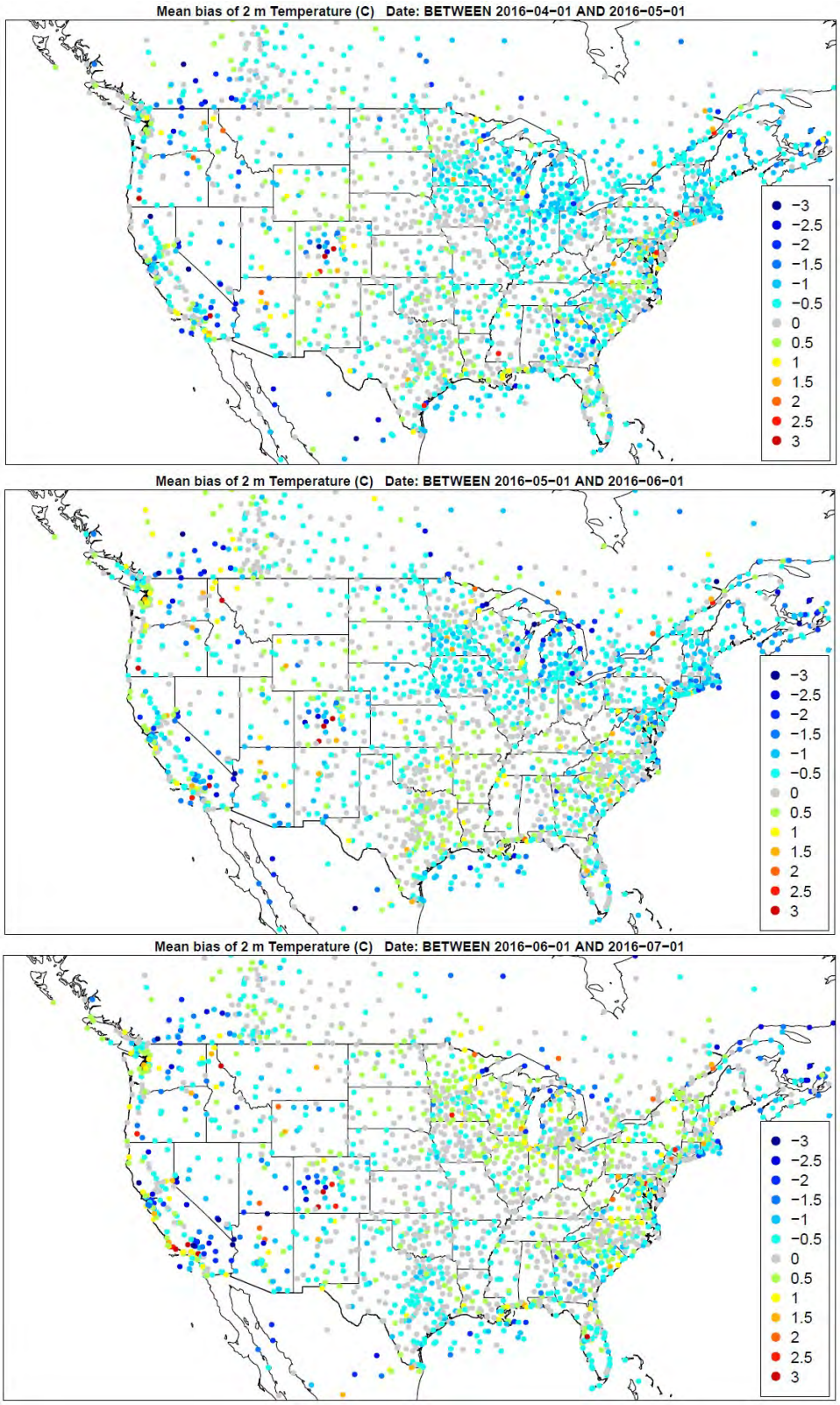

Figure 3.2.8. Spatial distribution of temperature bias (C) across all hours for the months of April, May, and June (top to bottom) for the 12US domain.

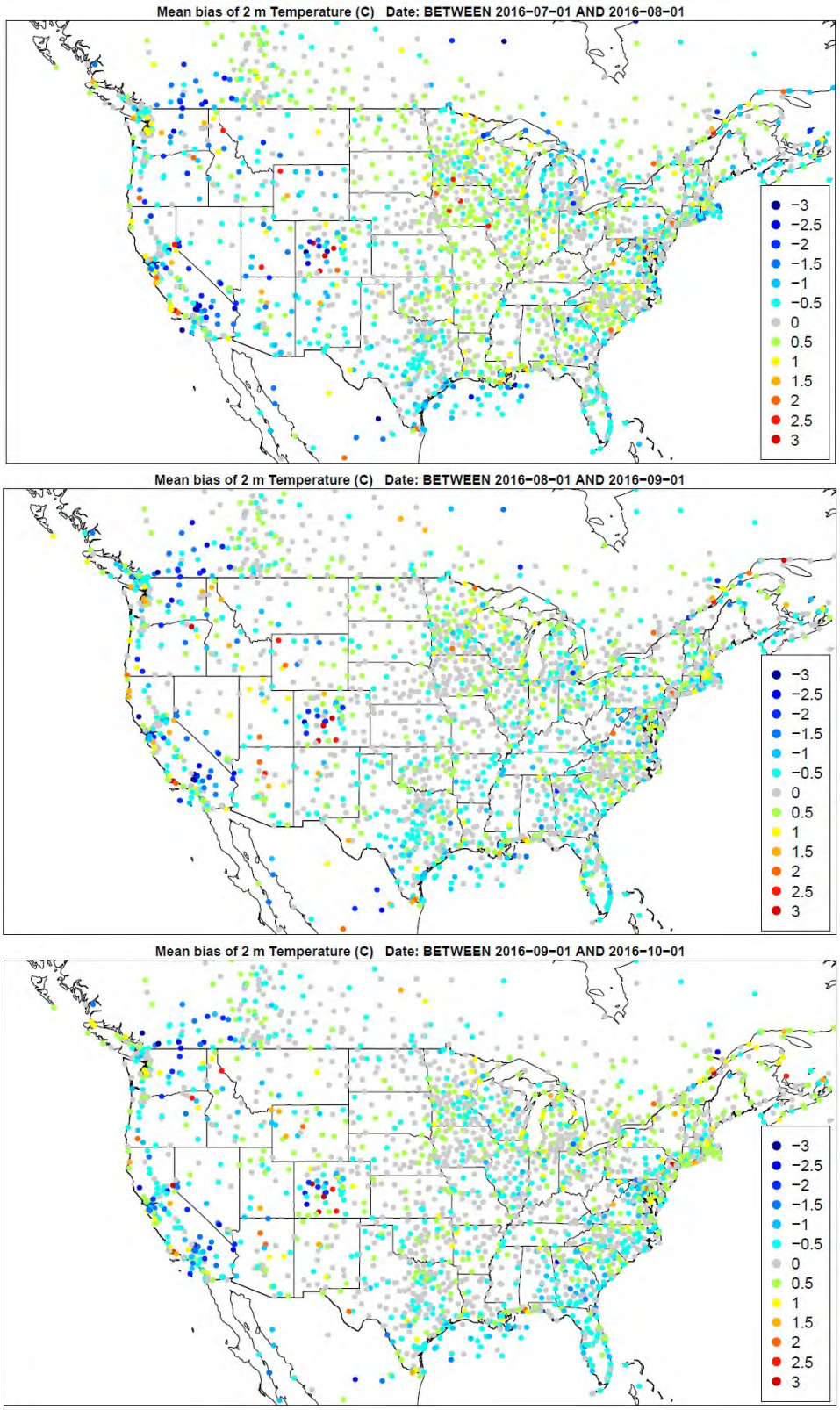

Figure 3.2.9. Spatial distribution of temperature bias (C) across all hours for the months of July, August, and September (top to bottom) for the 12US domain.

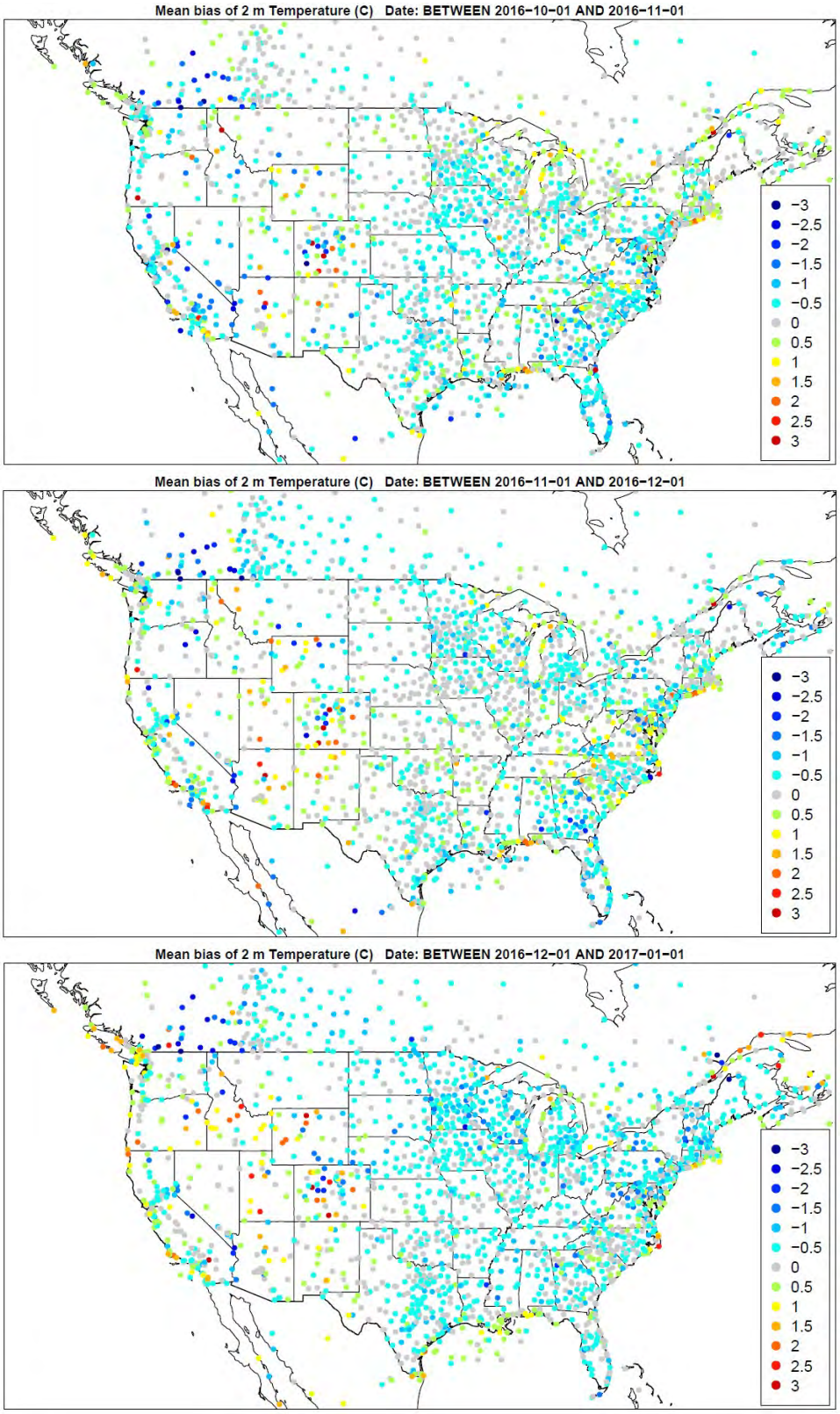

Figure 3.2.10. Spatial distribution of temperature bias (C) across all hours for the months of October, November, and December (top to bottom) for the 12US domain.

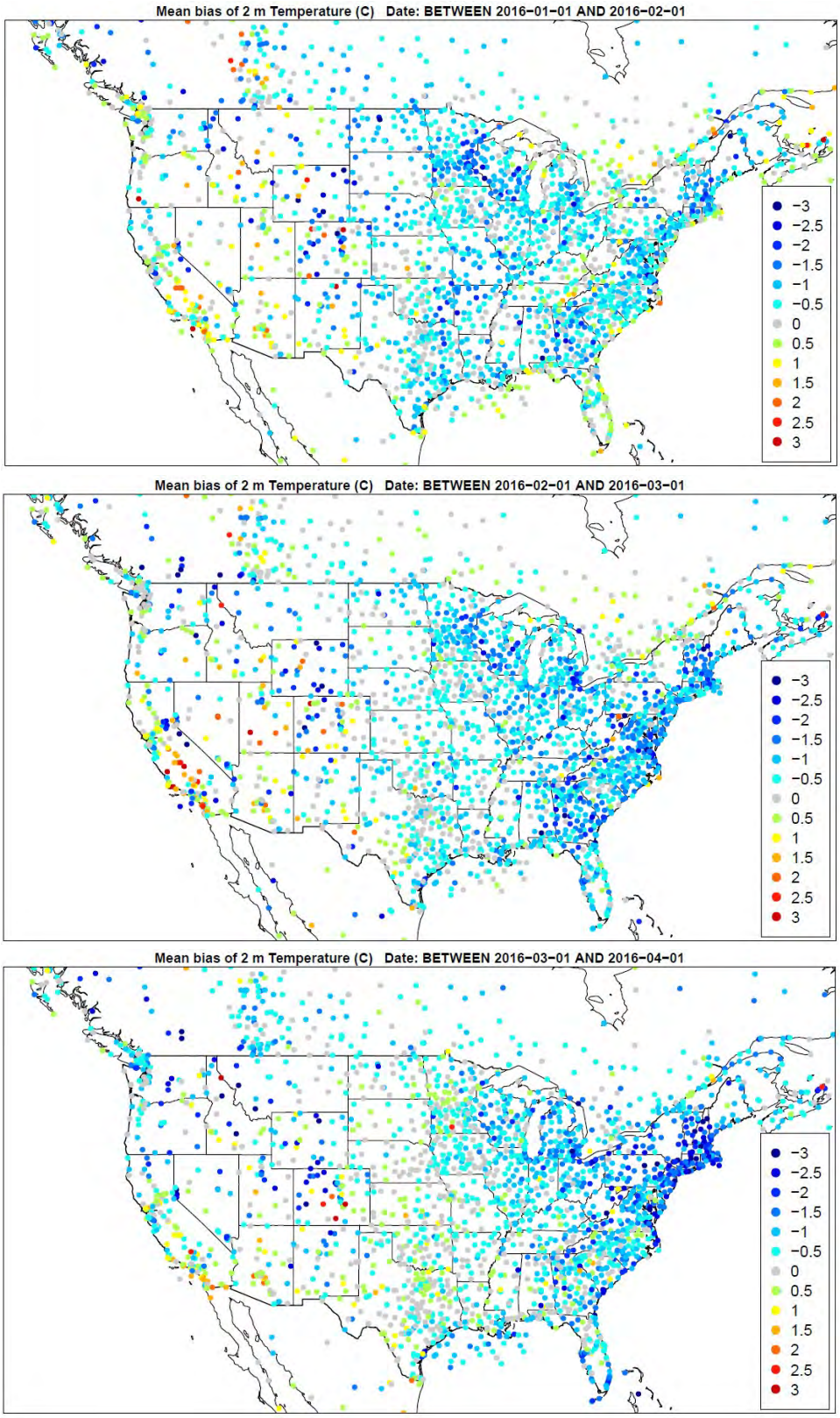

Figure 3.2.11. Spatial distribution of temperature bias (C) across daytime hours for the months of January, February, and March (top to bottom) for the 36NOAM domain.

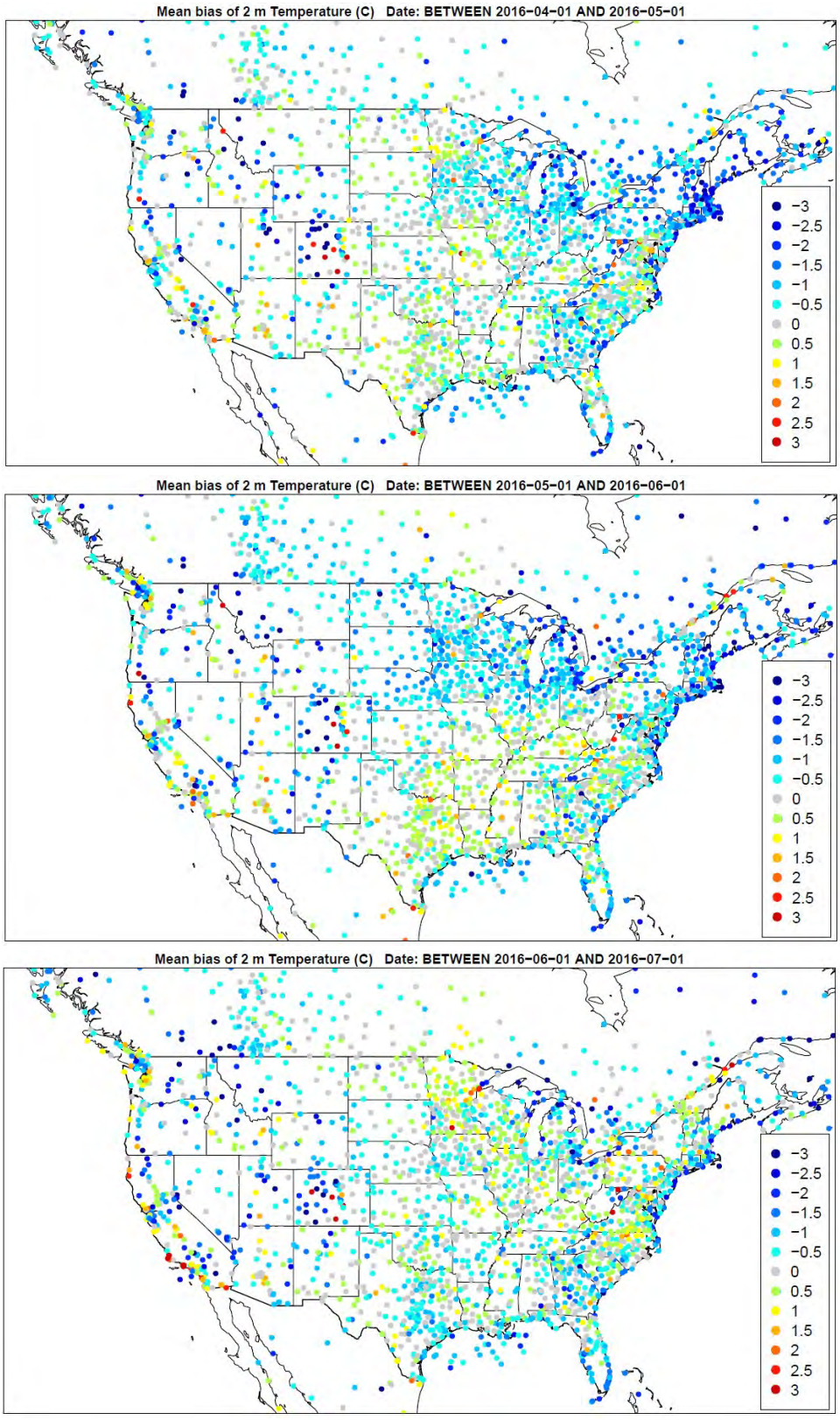

Figure 3.2.12. Spatial distribution of temperature bias (C) across daytime hours for the months of April, May, and June (top to bottom) for the 36NOAM domain.

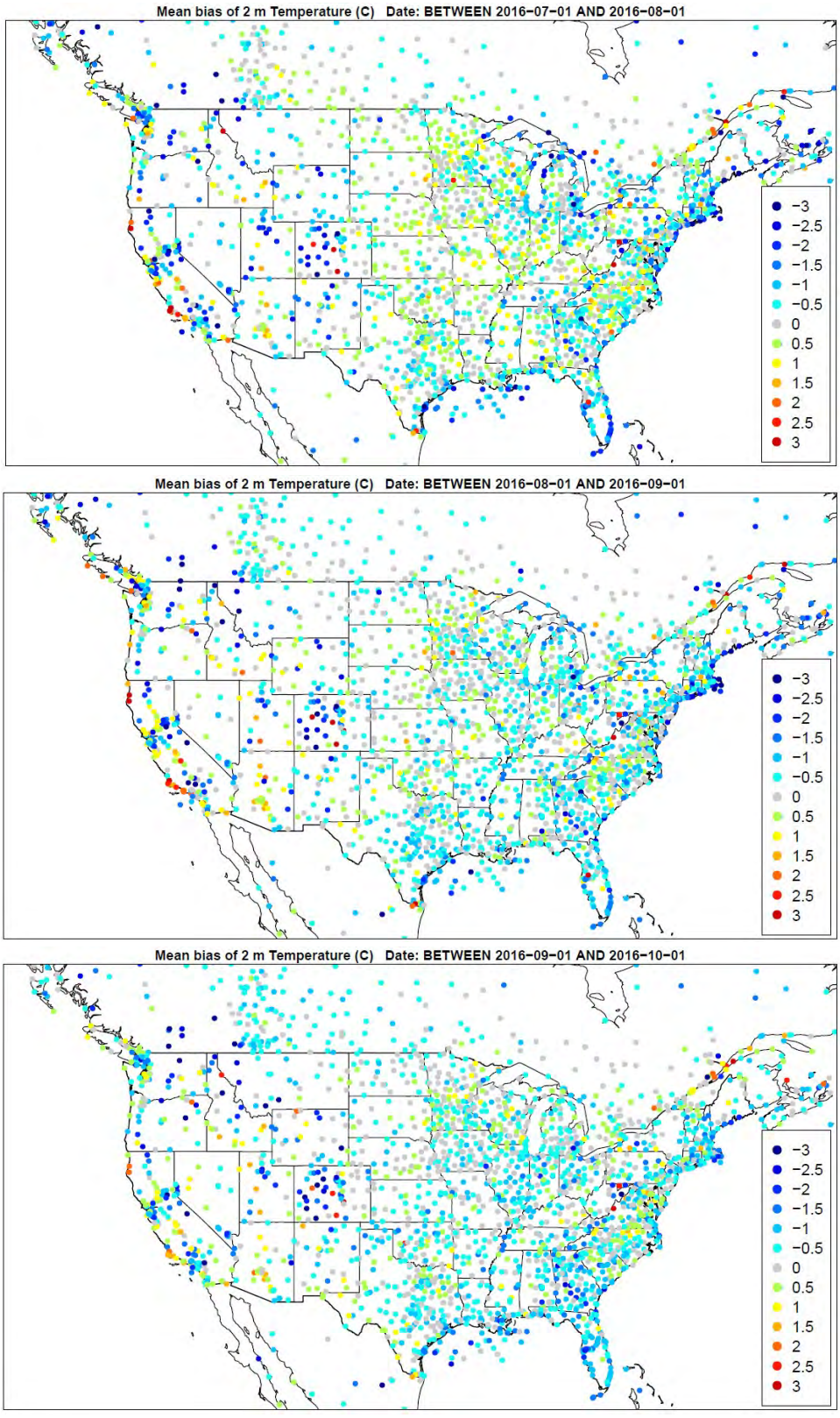

Figure 3.2.13. Spatial distribution of temperature bias (C) across daytime hours for the months of July, August, and September (top to bottom) for the 36NOAM domain.

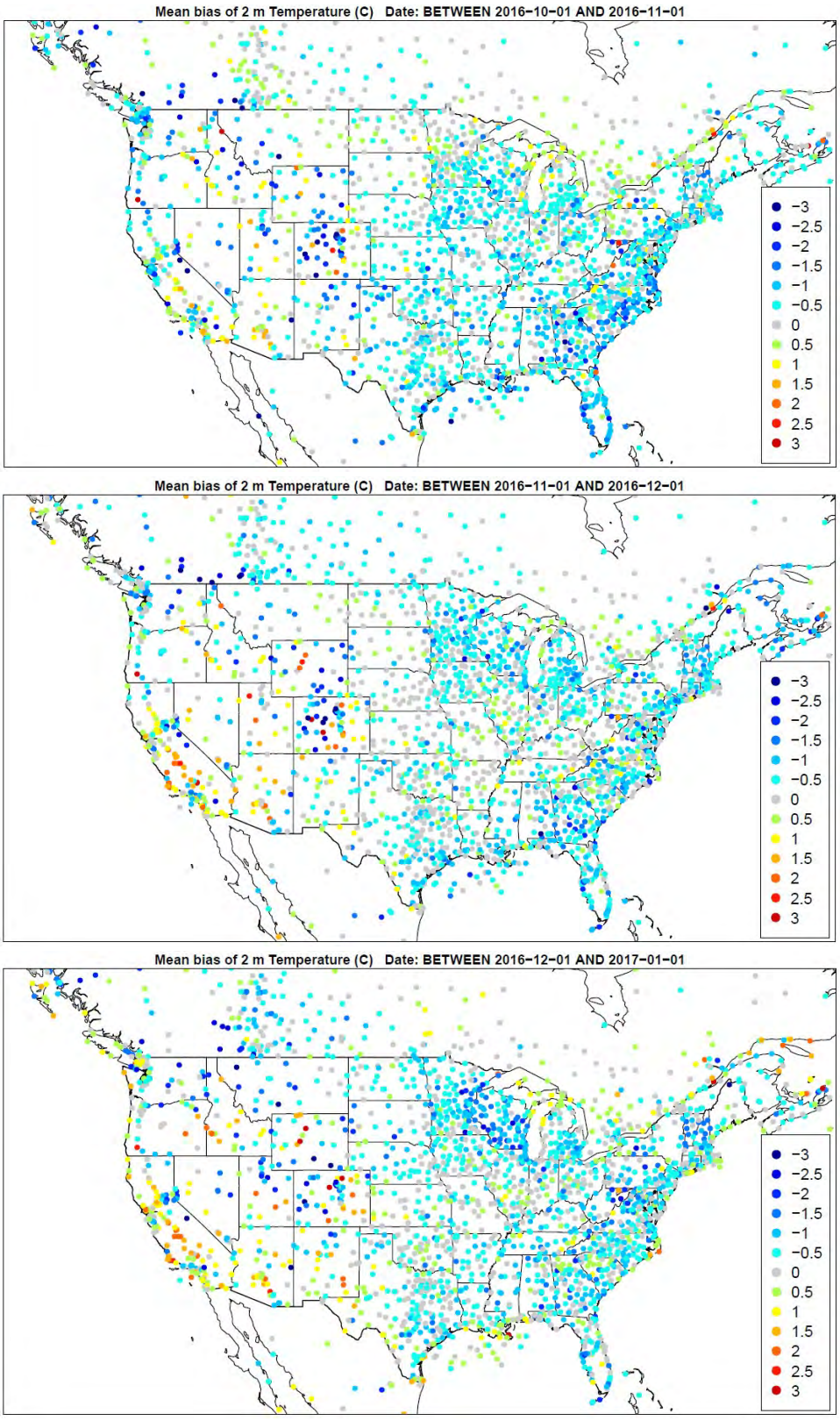

Figure 3.2.14. Spatial distribution of temperature bias (C) across daytime hours for the months of October, November, and December (top to bottom) for the 36NOAM domain.

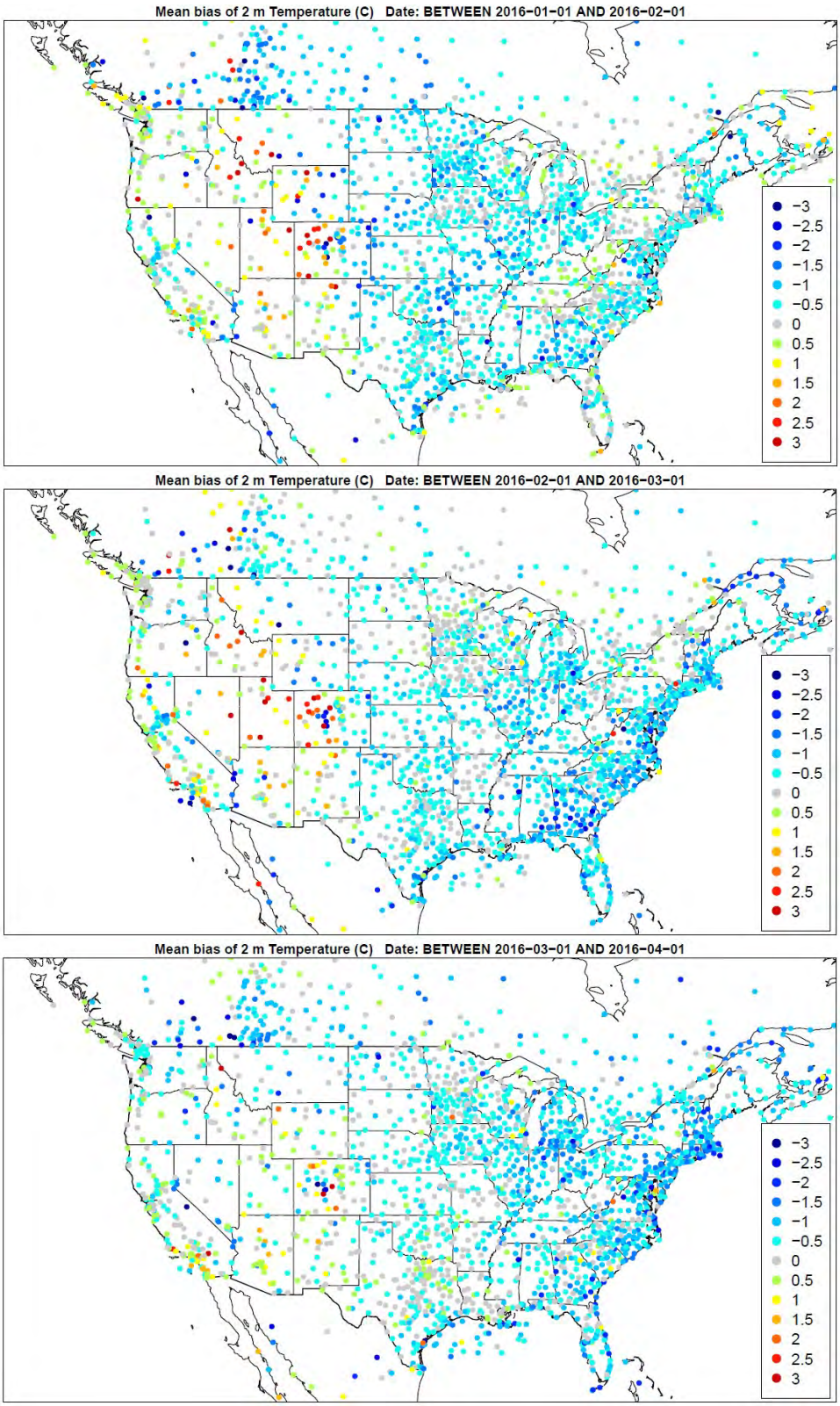

Figure 3.2.15. Spatial distribution of temperature bias (C) across daytime hours for the months of January, February, and March (top to bottom) for the 12US domain.

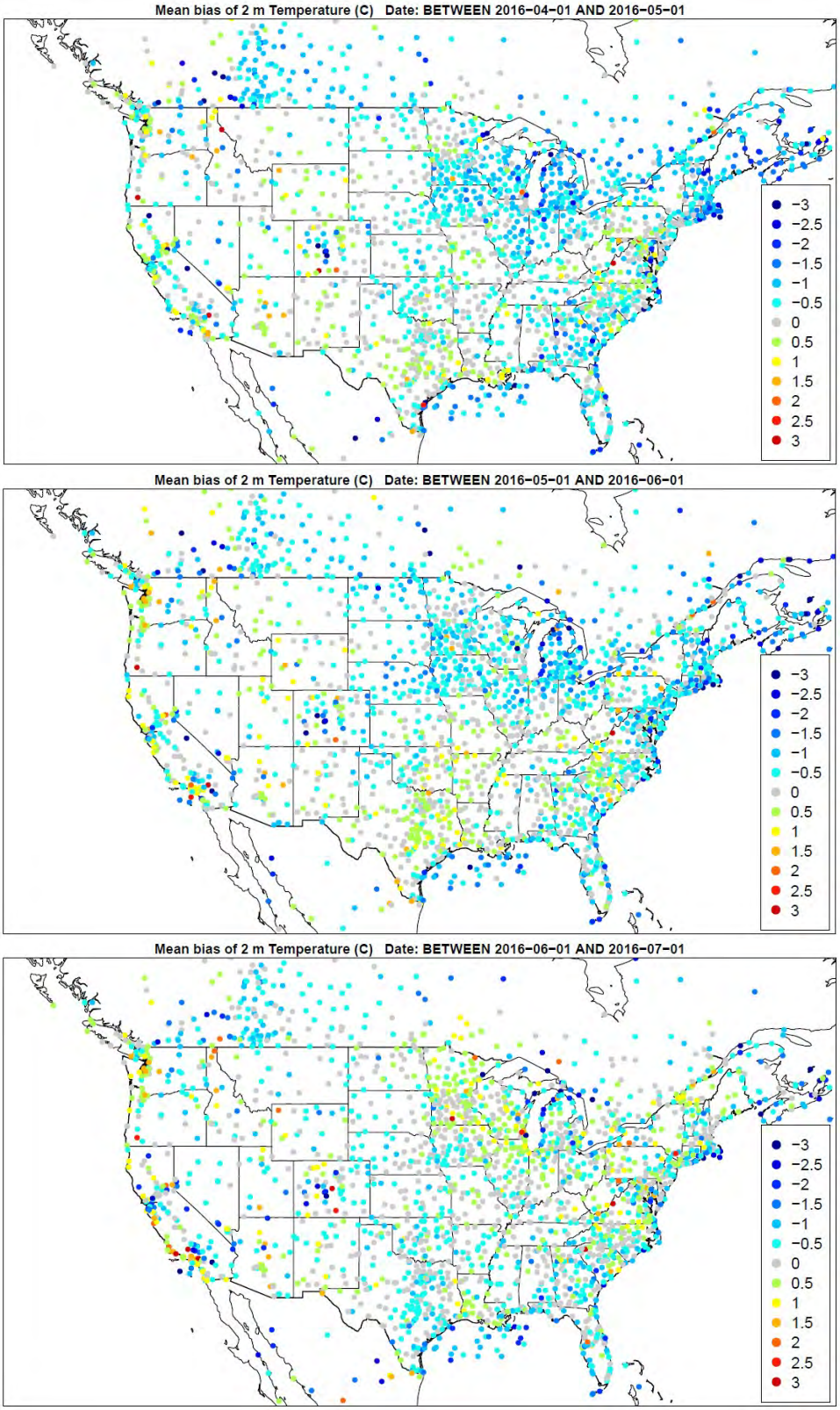

Figure 3.2.16. Spatial distribution of temperature bias (C) across daytime hours for the months of April, May, and June (top to bottom) for the 12US domain.

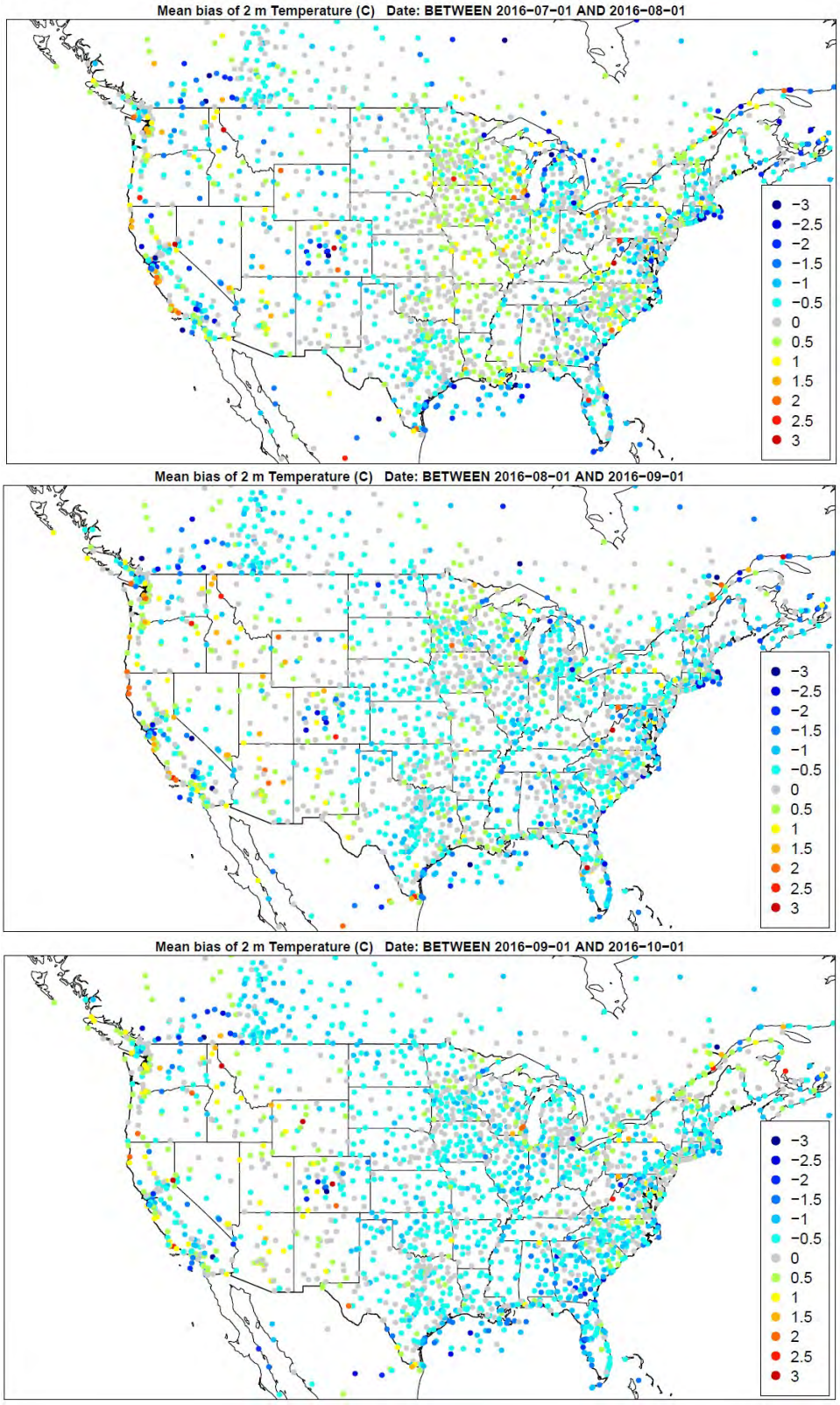

Figure 3.2.17. Spatial distribution of temperature bias (C) across daytime hours for the months of July, August, and September (top to bottom) for the 12US domain.

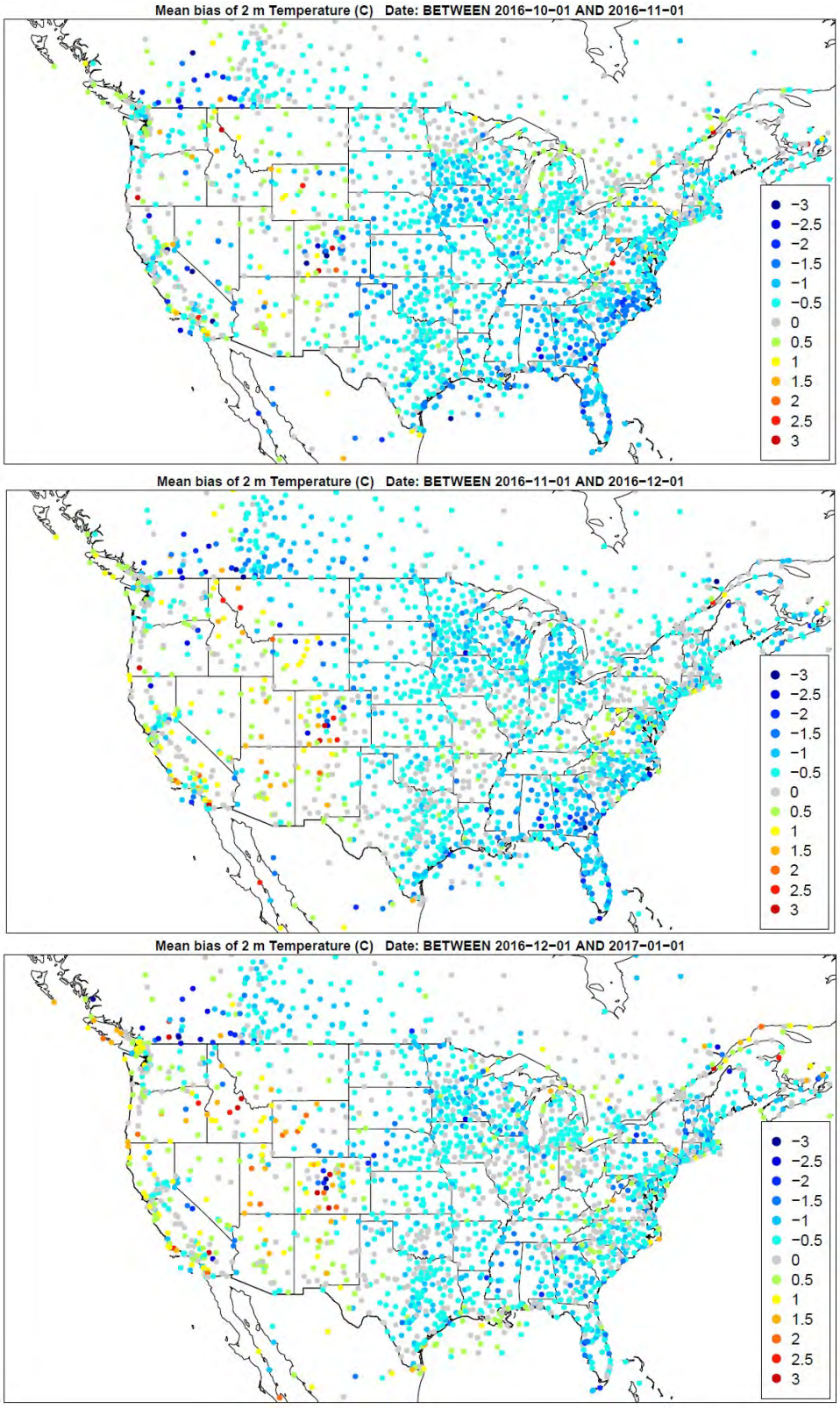

Figure 3.2.18. Spatial distribution of temperature bias (C) across daytime hours for the months of October, November, and December (top to bottom) for the 12US domain.

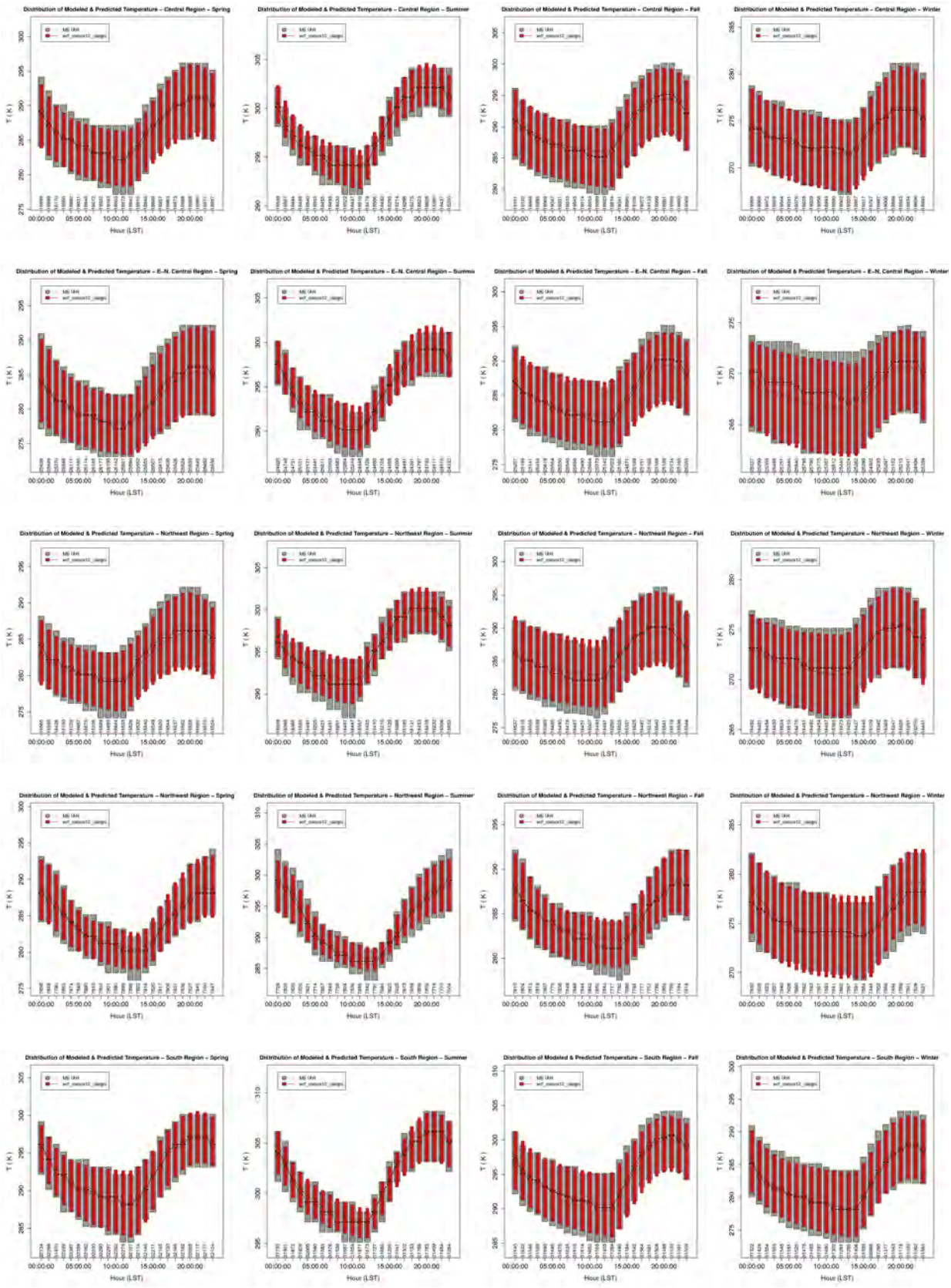
Distribution of Modeled & Predicted Temperature – Central Region – Spring
Distribution of Modeled & Predicted Temperature – Central Region – Summer
Distribution of Modeled & Predicted Temperature – Central Region – Fall
Distribution of Modeled & Predicted Temperature – Central Region – Winter
Distribution of Modeled & Predicted Temperature – E.-N. Central Region – Spring
Distribution of Modeled & Predicted Temperature – E.-N. Central Region – Summer
Distribution of Modeled & Predicted Temperature – E.-N. Central Region – Fall
Distribution of Modeled & Predicted Temperature – E.-N. Central Region – Winter
Distribution of Modeled & Predicted Temperature – Northeast Region – Spring
Distribution of Modeled & Predicted Temperature – Northeast Region – Summer
Distribution of Modeled & Predicted Temperature – Northeast Region – Fall
Distribution of Modeled & Predicted Temperature – Northeast Region – Winter
Distribution of Modeled & Predicted Temperature – Northwest Region – Spring
Distribution of Modeled & Predicted Temperature – Northwest Region – Summer
Distribution of Modeled & Predicted Temperature – Northwest Region – Fall
Distribution of Modeled & Predicted Temperature – Northwest Region – Winter
Distribution of Modeled & Predicted Temperature – South Region – Spring
Distribution of Modeled & Predicted Temperature – South Region – Summer
Distribution of Modeled & Predicted Temperature – South Region – Fall
Distribution of Modeled & Predicted Temperature – South Region – Winter
T (K)
Hour (LST)
00:00:00
05:00:00
10:00:00
15:00:00
20:00:00

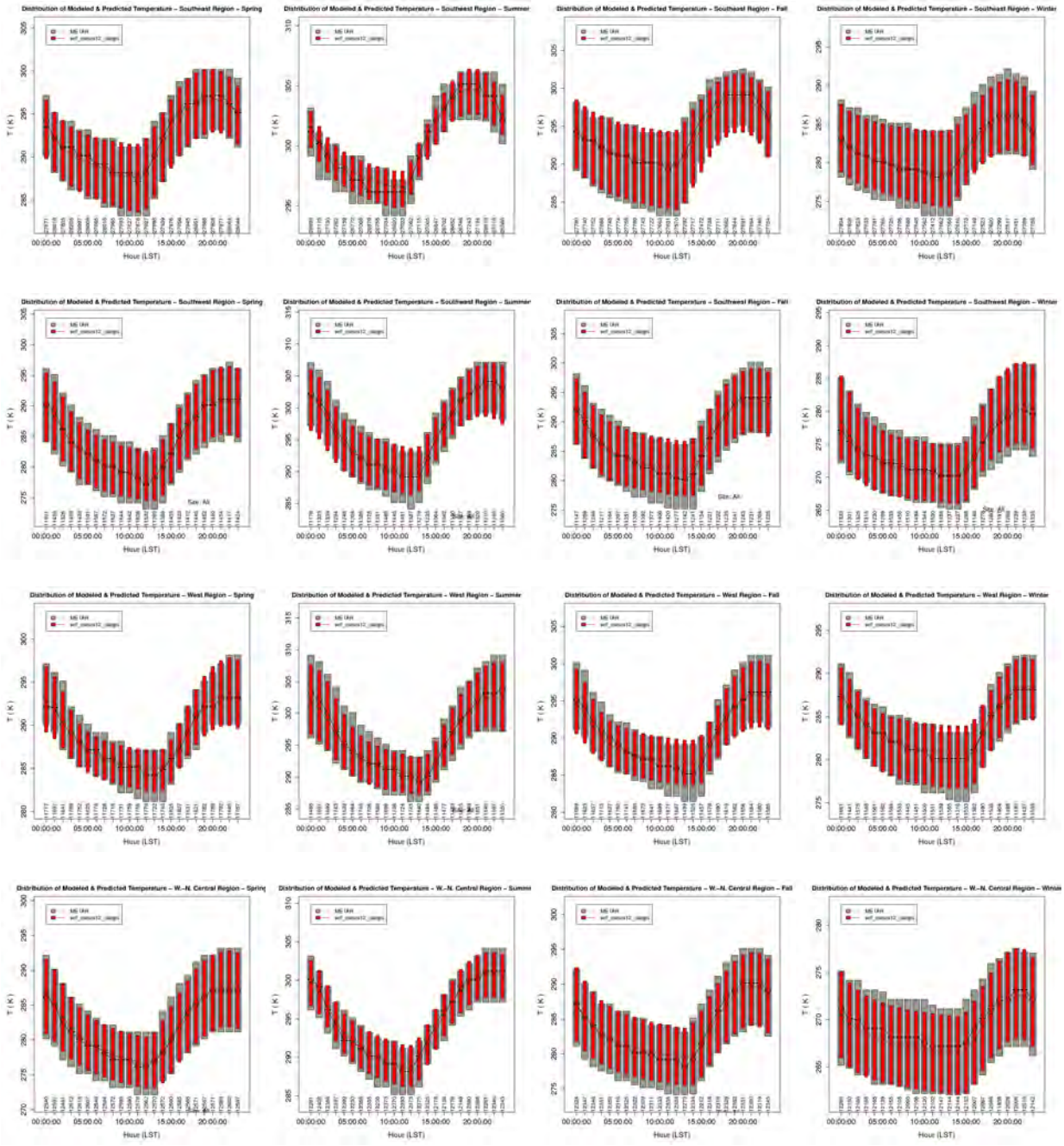

Figure 3.2.19. Hourly average distribution of observed and predicted temperature for the 12US domain in the Central, East-North Central, Northeast, Northwest, South, Southeast, Southwest, West, and West-North Central (top to bottom) regions for each season (Spring, Summer, Fall, Winter, L-R).

Climate Region	Season	Mean Obs	Mean Mod	MB	MAE	NMB	NME	RMSE
Northeast	Spring	282.51	282.26	-0.25	1.59	-0.09	0.56	2.13
Northeast	Summer	295.16	295.46	0.30	1.35	0.10	0.46	1.85
Northeast	Fall	285.68	285.95	0.27	1.52	0.09	0.53	2.05
Northeast	Winter	272.41	272.20	-0.21	1.74	-0.08	0.64	2.33
West-North Central	Spring	281.38	281.48	0.10	1.57	0.03	0.56	2.05
West-North Central	Summer	294.20	294.44	0.24	1.44	0.08	0.49	1.94
West-North Central	Fall	283.30	283.45	0.15	1.64	0.05	0.58	2.15
West-North Central	Winter	268.53	268.25	-0.29	1.92	-0.11	0.72	2.56
Northwest	Spring	283.93	283.99	0.06	1.51	0.02	0.53	2.00
Northwest	Summer	292.38	292.45	0.07	1.61	0.02	0.55	2.15
Northwest	Fall	284.15	284.27	0.12	1.57	0.04	0.55	2.08
Northwest	Winter	274.55	274.85	0.30	1.79	0.11	0.65	2.44
Central	Spring	286.08	285.99	-0.09	1.47	-0.03	0.51	1.94
Central	Summer	297.50	297.77	0.27	1.18	0.09	0.40	1.61
Central	Fall	288.66	288.77	0.12	1.39	0.04	0.48	1.80
Central	Winter	273.75	273.54	-0.21	1.53	-0.08	0.56	1.99
South	Spring	291.40	291.57	0.18	1.38	0.06	0.48	1.83
South	Summer	300.64	300.82	0.18	1.09	0.06	0.36	1.53
South	Fall	293.40	293.52	0.12	1.32	0.04	0.45	1.76
South	Winter	281.71	281.65	-0.06	1.60	-0.02	0.57	2.06
Southeast	Spring	291.16	291.10	-0.06	1.39	-0.02	0.48	1.82
Southeast	Summer	299.70	299.89	0.19	1.18	0.06	0.39	1.60
Southeast	Fall	292.44	292.42	-0.02	1.43	-0.01	0.49	1.88
Southeast	Winter	281.87	281.74	-0.13	1.65	-0.05	0.58	2.13
Southwest	Spring	284.65	284.75	0.10	1.79	0.03	0.63	2.36
Southwest	Summer	296.61	296.70	0.09	1.87	0.03	0.63	2.54
Southwest	Fall	286.91	287.20	0.29	1.91	0.10	0.67	2.52
Southwest	Winter	274.86	275.13	0.27	2.30	0.10	0.84	3.13
East-North Central	Spring	281.56	281.39	-0.16	1.50	-0.06	0.53	1.99
East-North Central	Summer	294.26	294.60	0.34	1.27	0.12	0.43	1.71
East-North Central	Fall	284.74	284.85	0.12	1.36	0.04	0.48	1.81
East-North Central	Winter	267.78	267.51	-0.27	1.52	-0.10	0.57	2.02
West	Spring	288.61	288.40	-0.21	1.61	-0.07	0.56	2.17
West	Summer	296.97	296.75	-0.22	1.81	-0.07	0.61	2.46
West	Fall	290.17	290.06	-0.11	1.84	-0.04	0.63	2.47
West	Winter	282.54	282.58	0.03	1.81	0.01	0.64	2.47

Table 3.2.1. Mean observed, mean modeled, mean bias (MB), mean absolute error (MAE), normalized mean bias (NMB), normalized mean error (NME), and root mean square error (RMSE) for temperature (K) for the 12US simulation.

3.3 Mixing Ratio

Water mixing ratio estimates are compared to the ds472 observation network described earlier and are presented below for the 36NOAM (Figure 3.3.1) and 12US (Figure 3.3.2) domains.

In either simulation, no significant positive or negative bias is observed. However, WRF tends to be slightly drier in the morning and early afternoon hours relative to the rest of the day. Additionally, there is more uncertainty in model predictions during the spring and summer months. This increase in error is explained by the increased convective activity and influx of moist air masses that are typical of that time of year. In general, WRF performance was adequate for water vapor mixing ratio.

The monthly spatial distributions of the mixing ratio bias across all hours for the 36km and 12km simulation are shown in Figures 3.3.3-3.3.6 and 3.3.7-3.3.10, respectively. The spatial distribution of the mean bias during daytime hours for the 36km and 12km simulations are shown in Figures 3 3.3.11-3.3.14 and 3.3.15-3.3.18, respectively. Lastly, the hourly average distribution of observed and predicted water vapor mixing ratio for each season and region is presented in Figure 3.3.19. Little appreciable difference is observed in the biases either across all hours or just daytime. This is to be expected since water vapor mixing ratio has less temporal variability when compared to other variables (i.e., temperature). A slight overprediction persists across the eastern US during the late Winter through late Summer before transitioning to a slight underprediction through early Winter. Mixing ratio performance is generally unbiased to slightly underpredicted across the western states throughout the year.

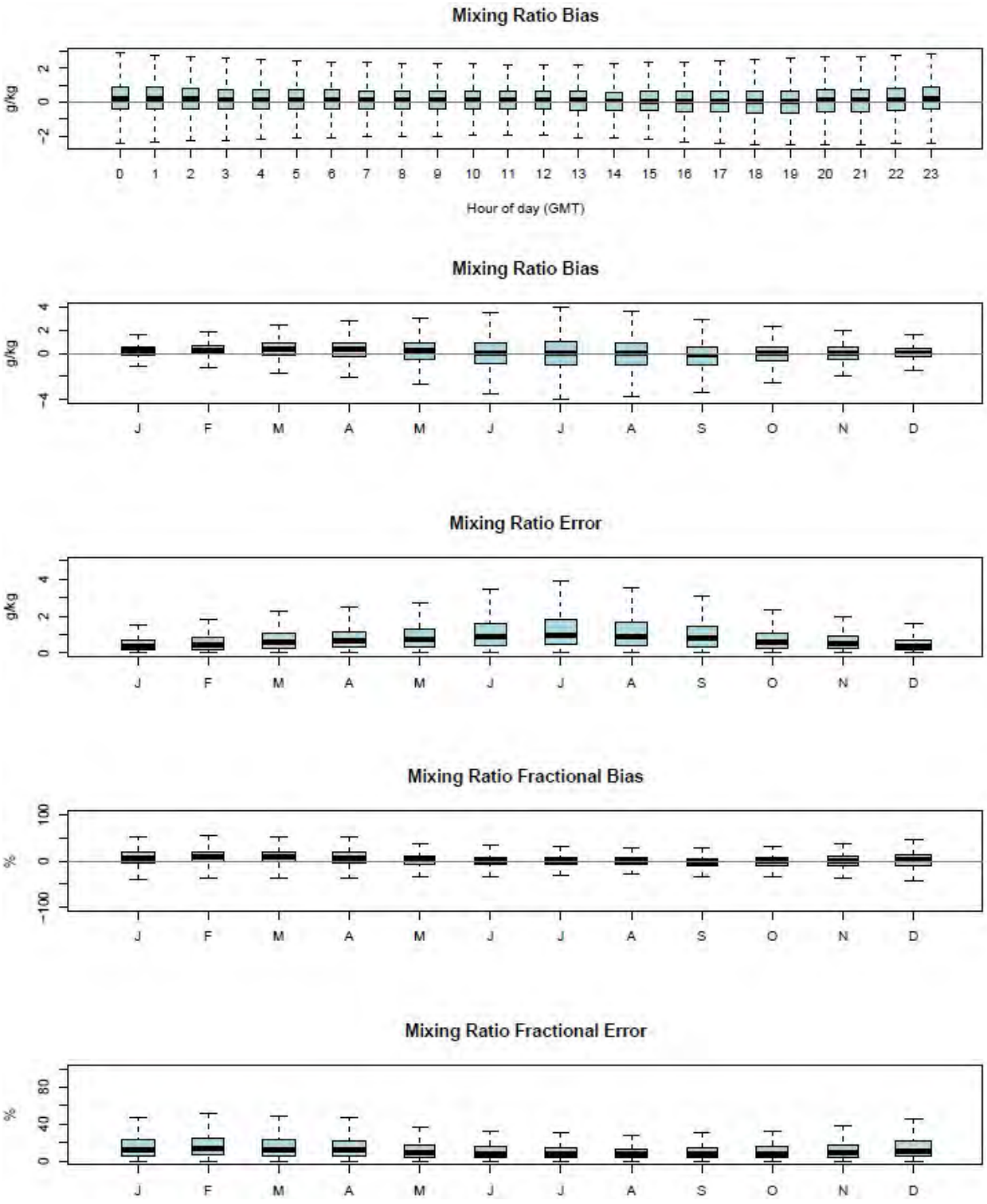

Figure 3.3.1. Distribution of hourly bias by hour and hourly bias, error, fractional bias, and fractional error for water vapor mixing ratio by month for the 36NOAM domain.

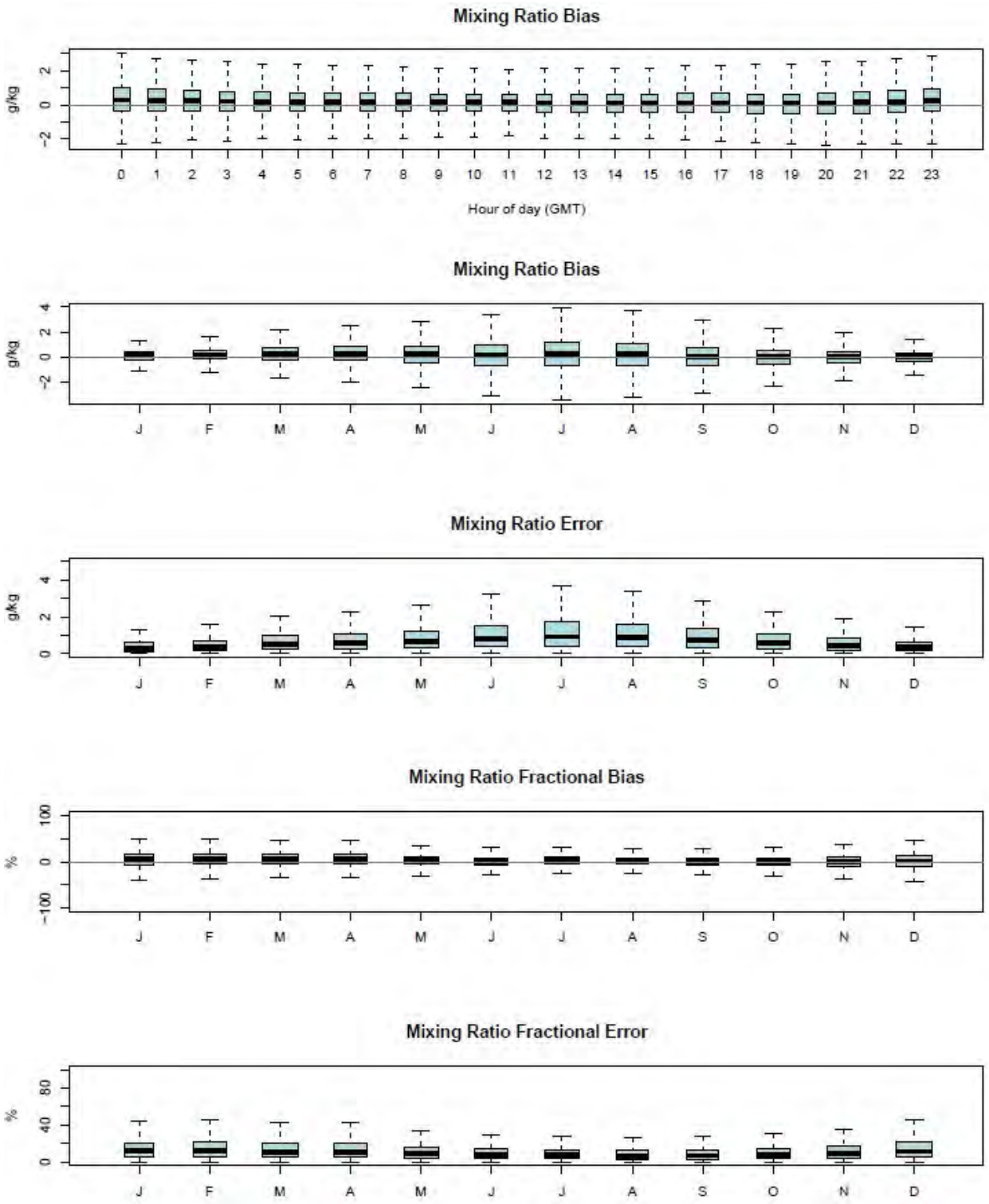

Figure 3.3.2. Distribution of hourly bias by hour and hourly bias, error, fractional bias, and fractional error for water vapor mixing ratio by month for the 12US domain.

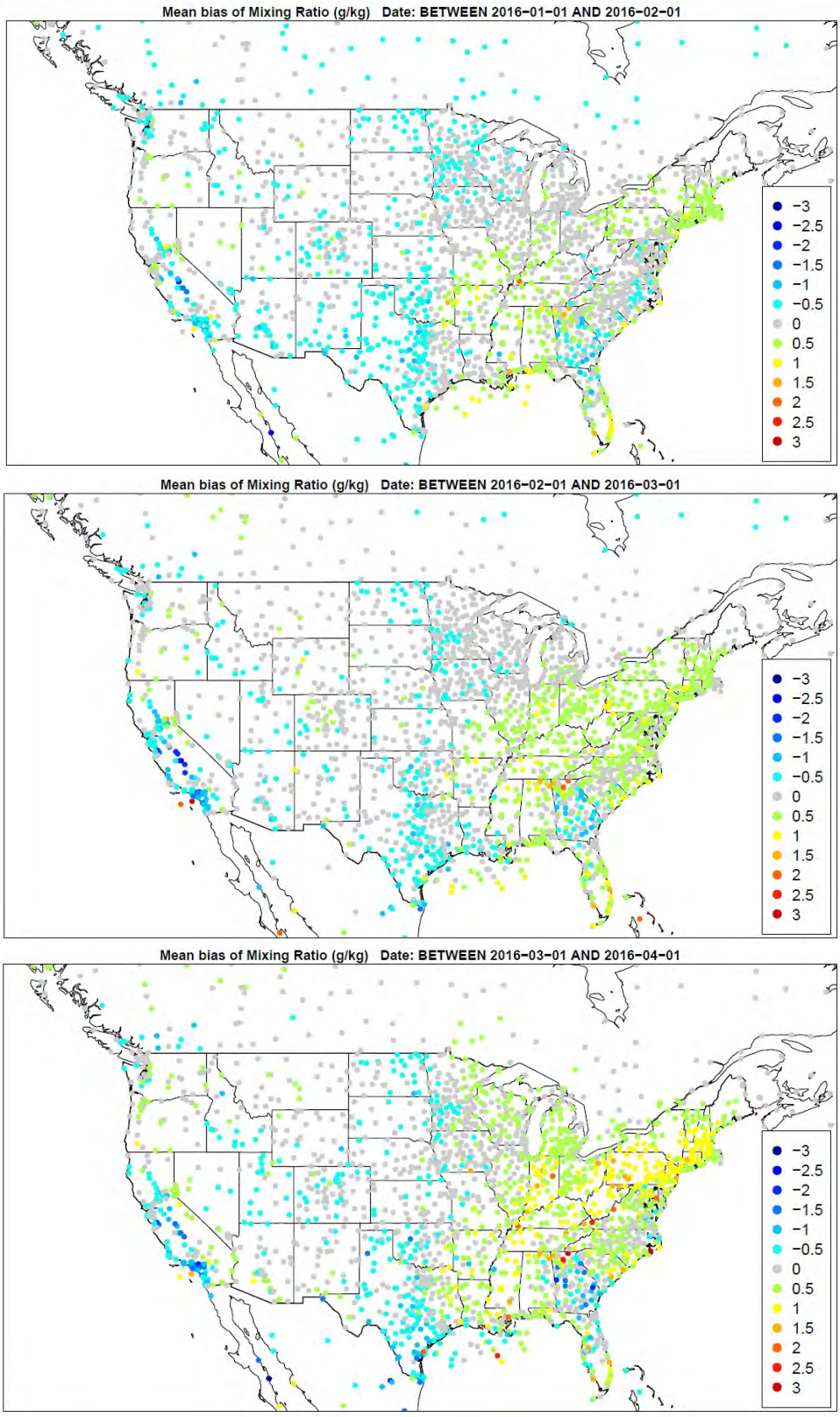

Figure 3.3.3. Spatial distribution of water vapor mixing ratio bias (g/kg) across all hours for the months of January, February, and March (top to bottom) for the 36NOAM domain.

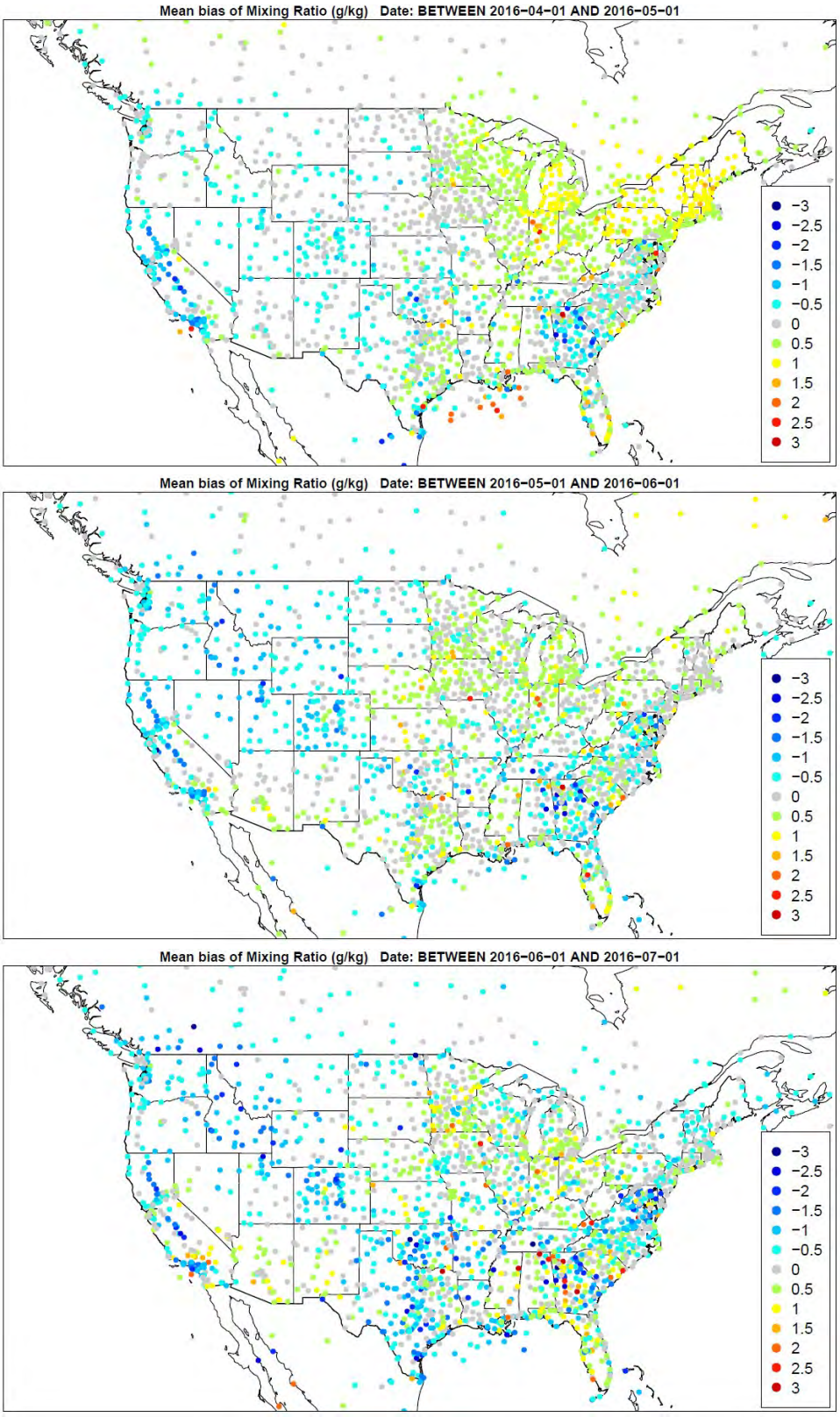

Figure 3.3.4. Spatial distribution of water vapor mixing ratio bias (g/kg) across all hours for the months of April, May, and June (top to bottom) for the 36NOAM domain.

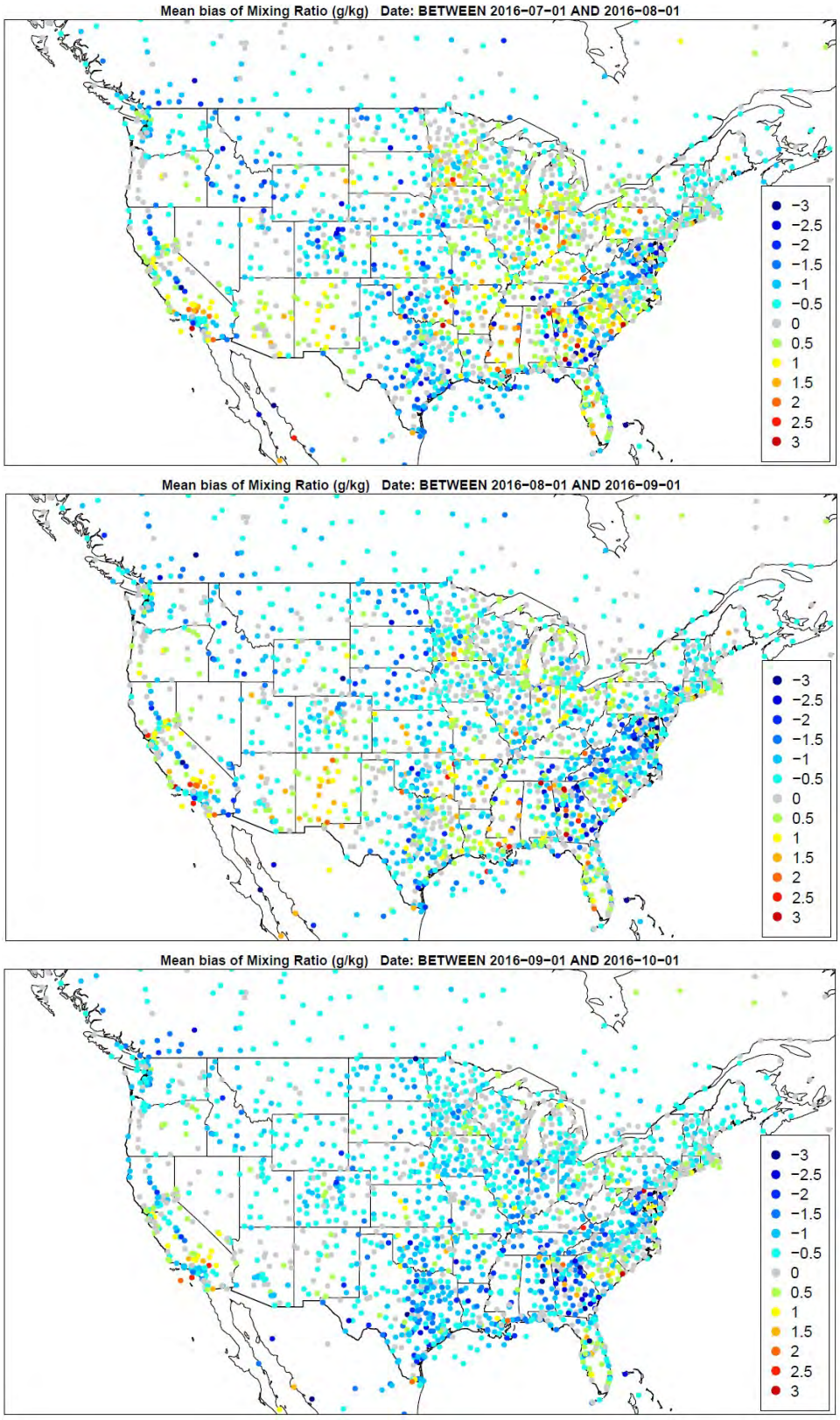

Figure 3.3.5. Spatial distribution of water vapor mixing ratio bias (g/kg) across all hours for the months of July, August, and September (top to bottom) for the 36NOAM domain.

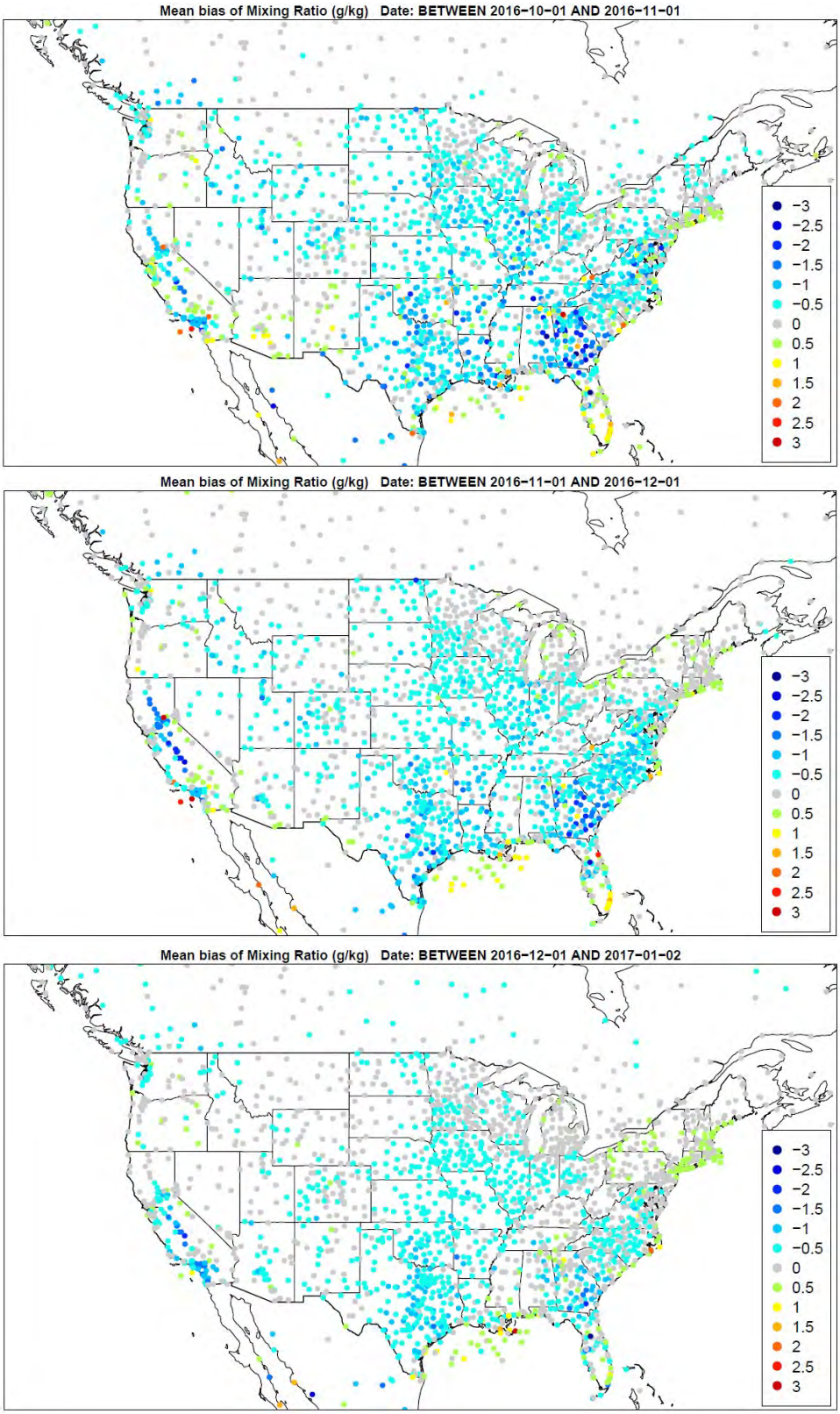

Figure 3.3.6. Spatial distribution of water vapor mixing ratio bias (g/kg) across all hours for the months of October, November, and December (top to bottom) for the 36NOAM domain.

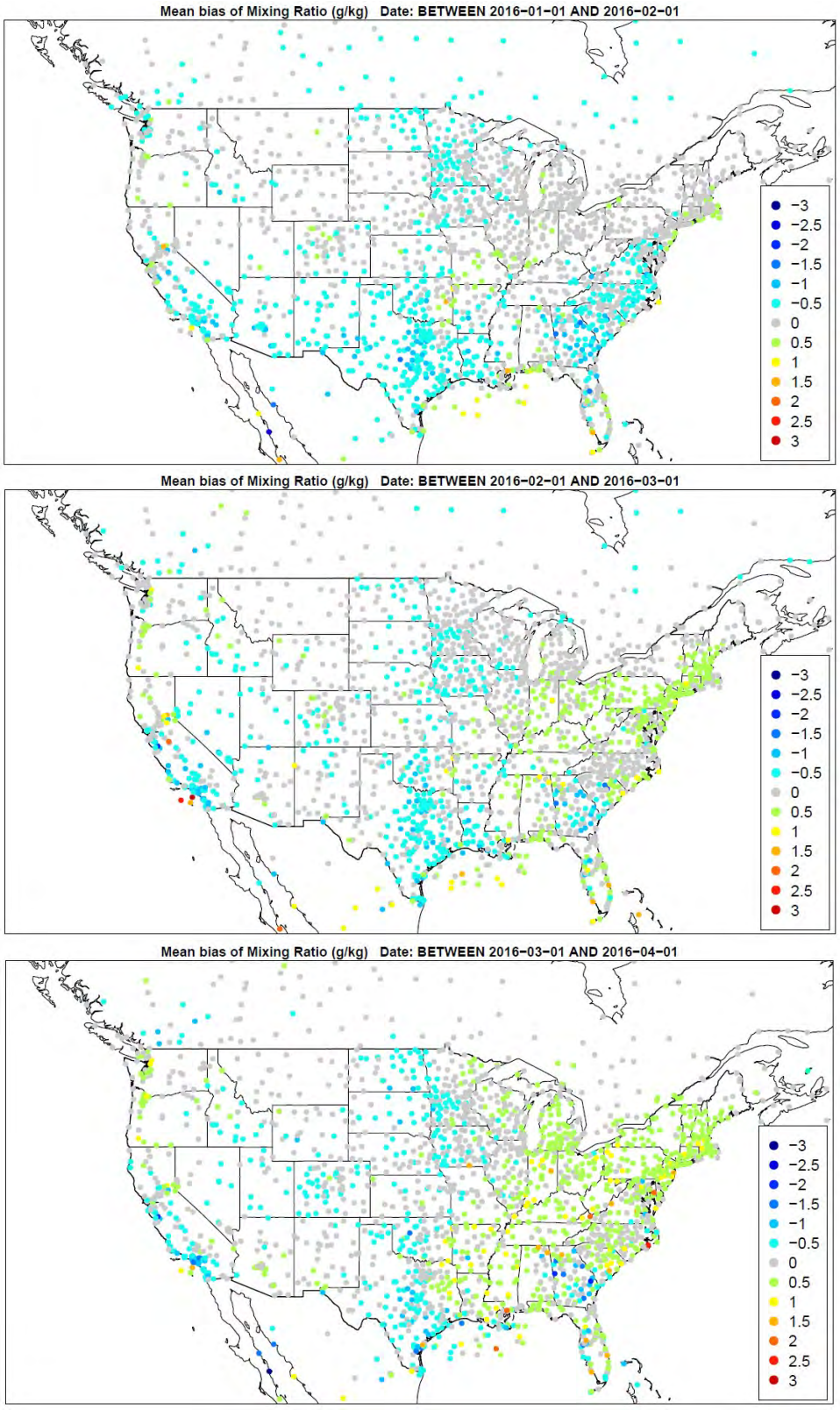

Figure 3.3.7. Spatial distribution of water vapor mixing ratio bias (g/kg) across all hours for the months of January, February, and March (top to bottom) for the 12US domain.

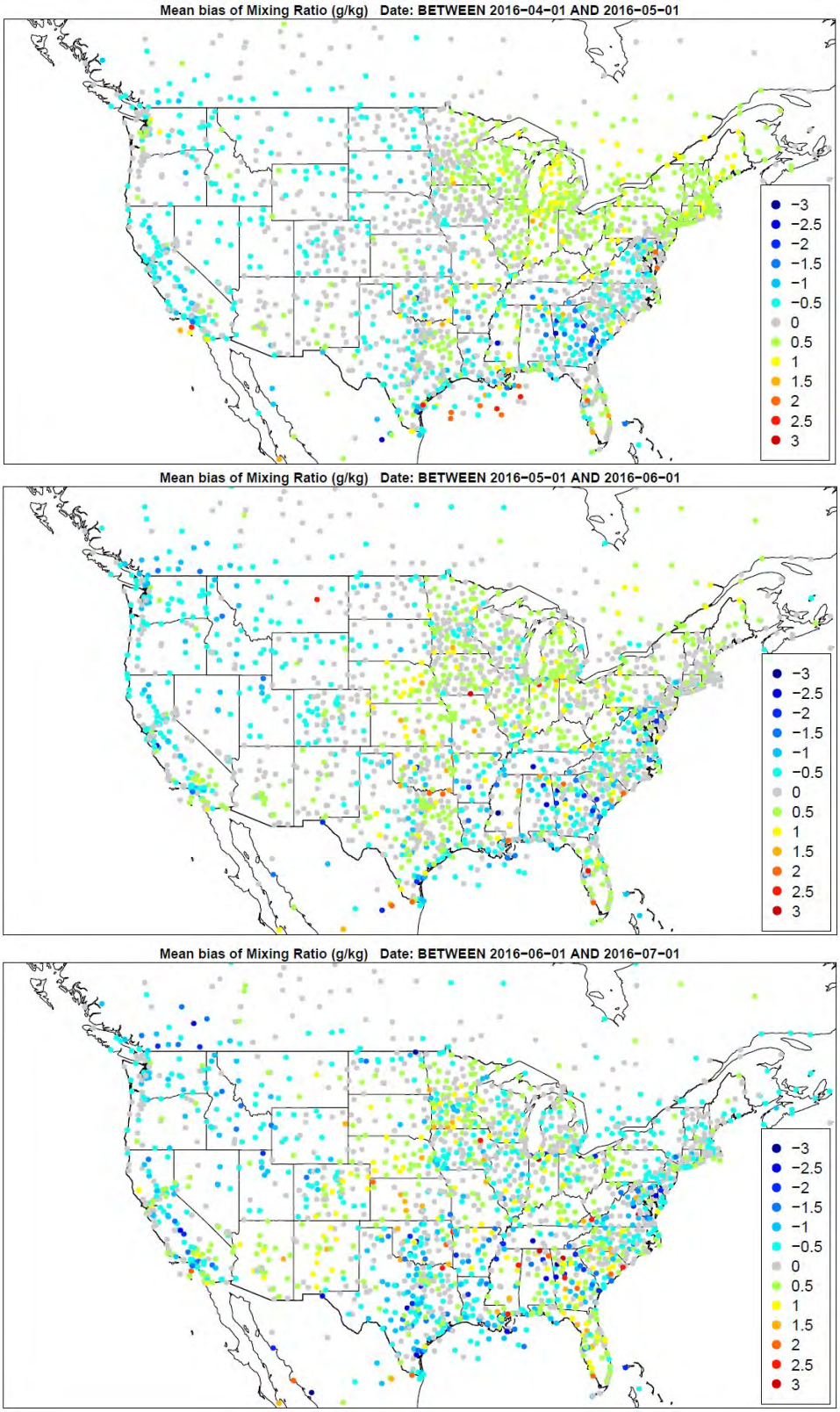

Figure 3.3.8. Spatial distribution of water vapor mixing ratio bias (g/kg) across all hours for the months of April, May, and June (top to bottom) for the 12US domain.

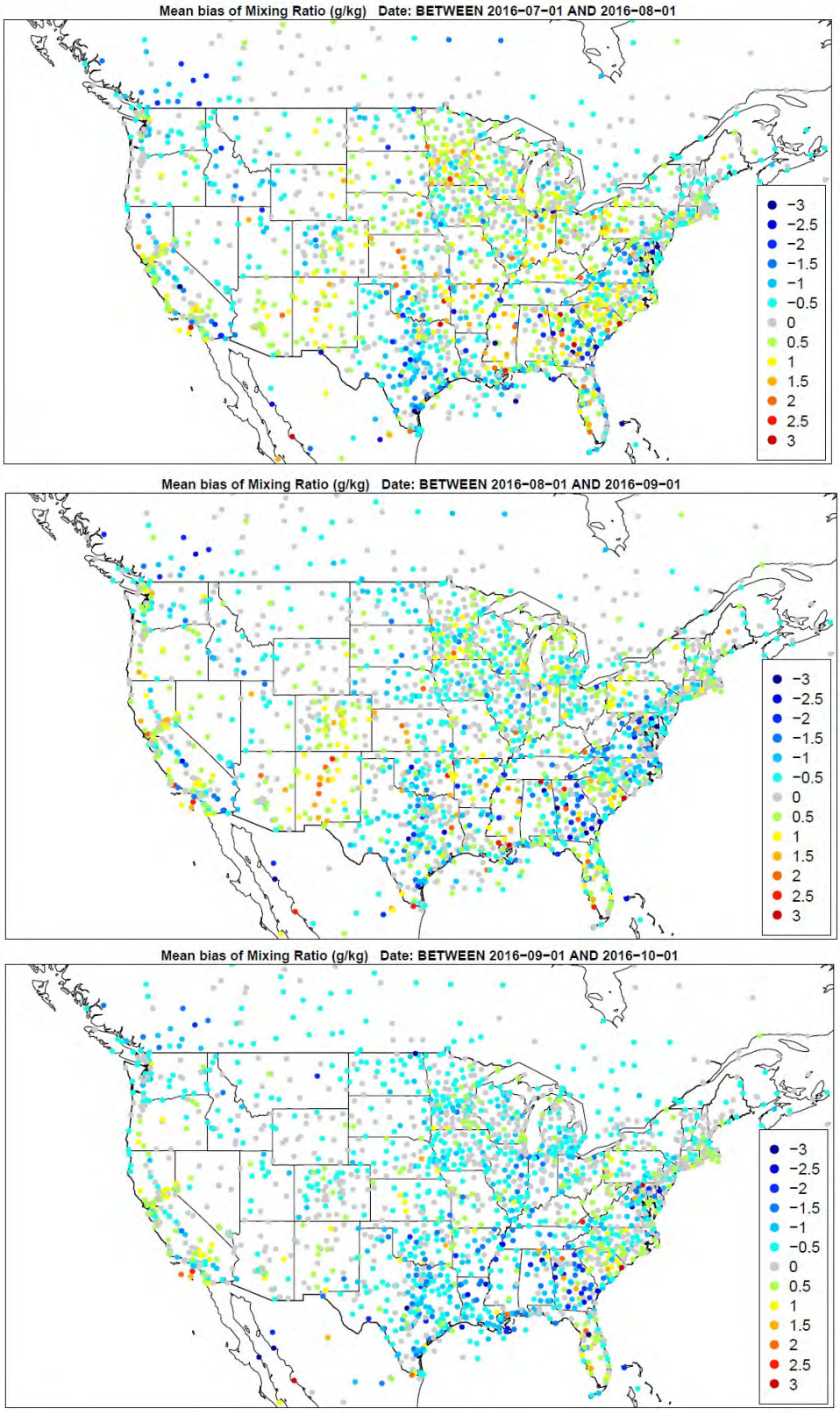

Figure 3.3.9. Spatial distribution of water vapor mixing ratio bias (g/kg) across all hours for the months of July, August, and September (top to bottom) for the 12US domain.

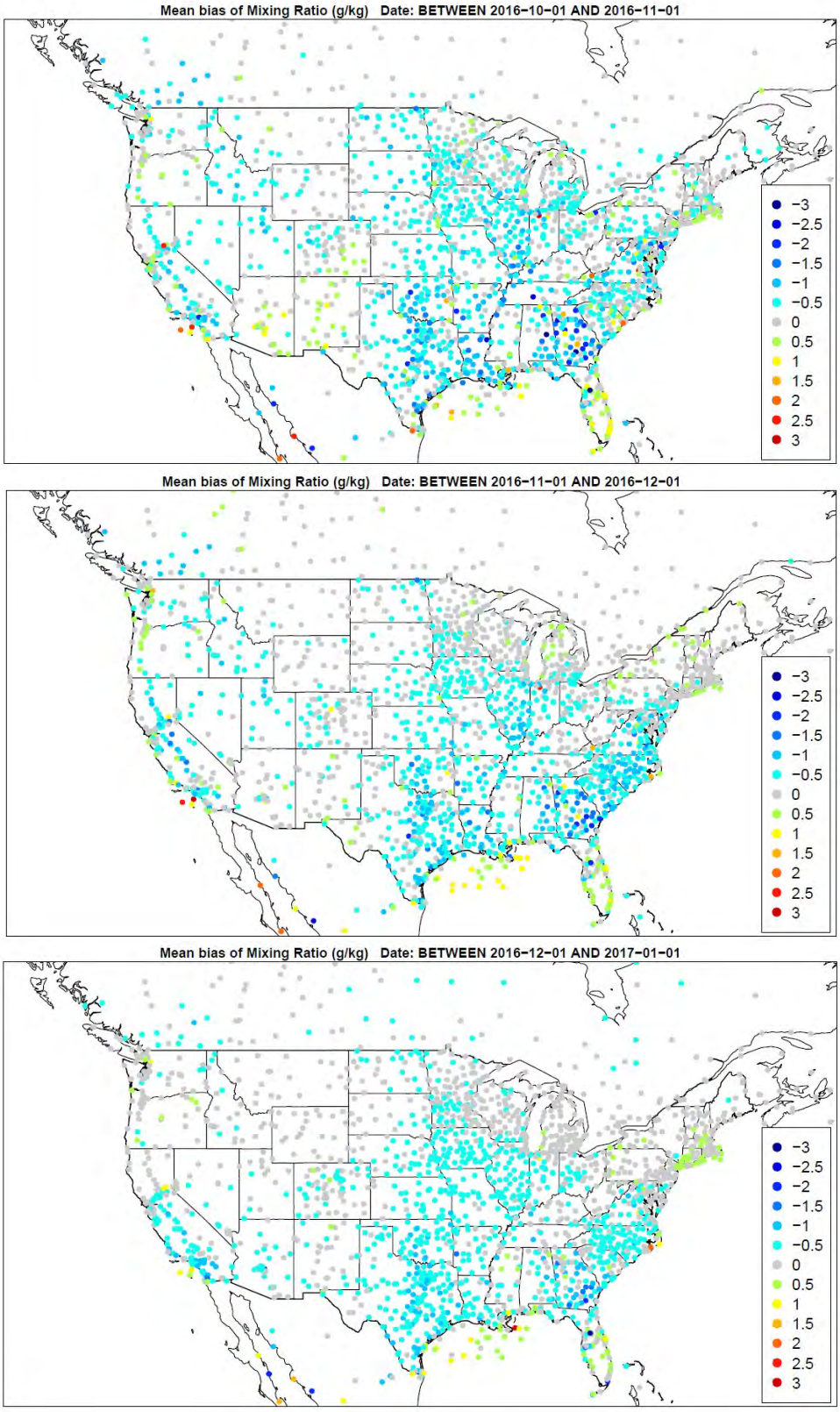

Figure 3.3.10. Spatial distribution of water vapor mixing ratio bias (g/kg) across all hours for the months of October, November, and December (top to bottom) for the 12US domain.

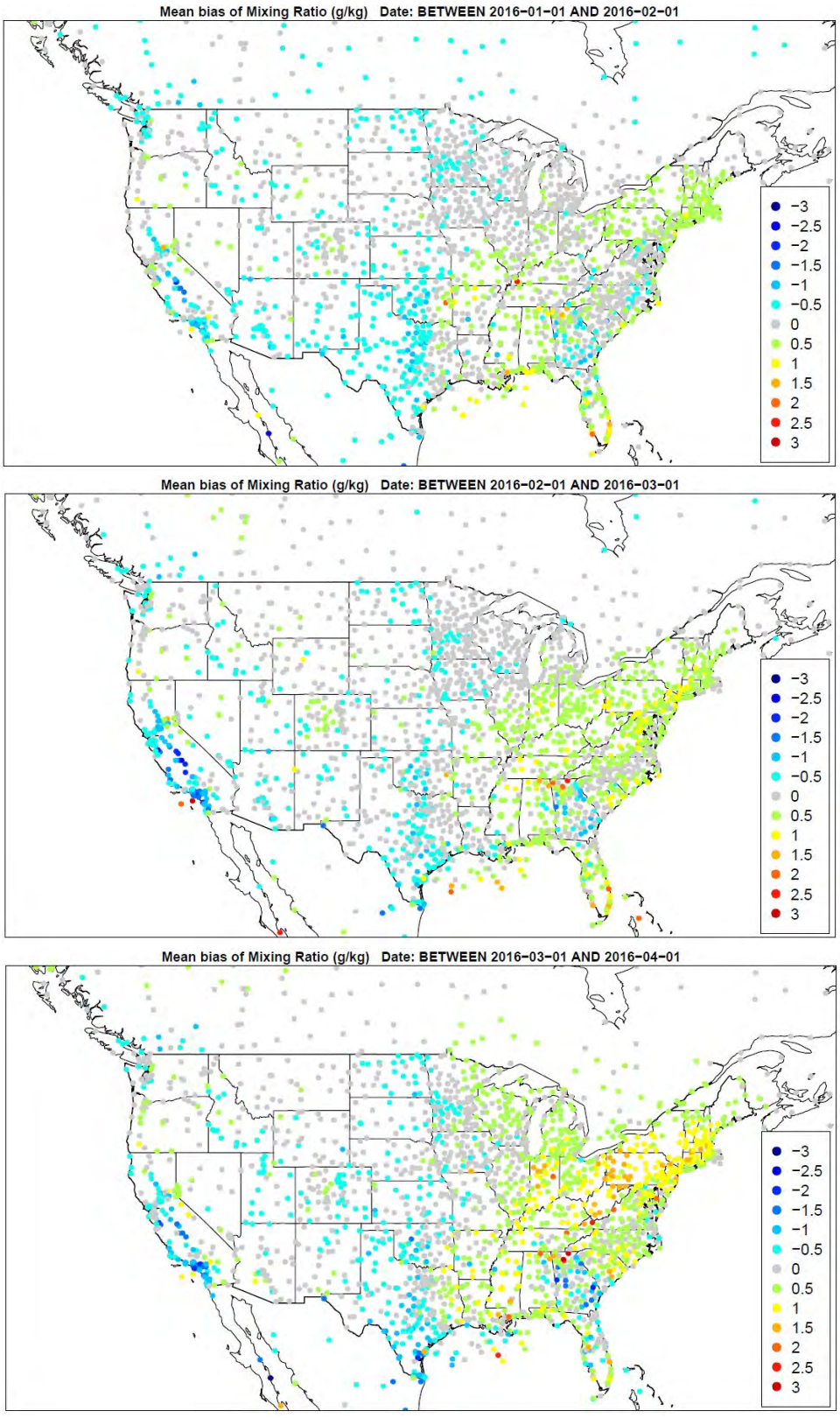

Figure 3.3.11. Spatial distribution of water vapor mixing ratio bias (g/kg) across daytime hours for the months of January, February, and March (top to bottom) for the 36NOAM domain.

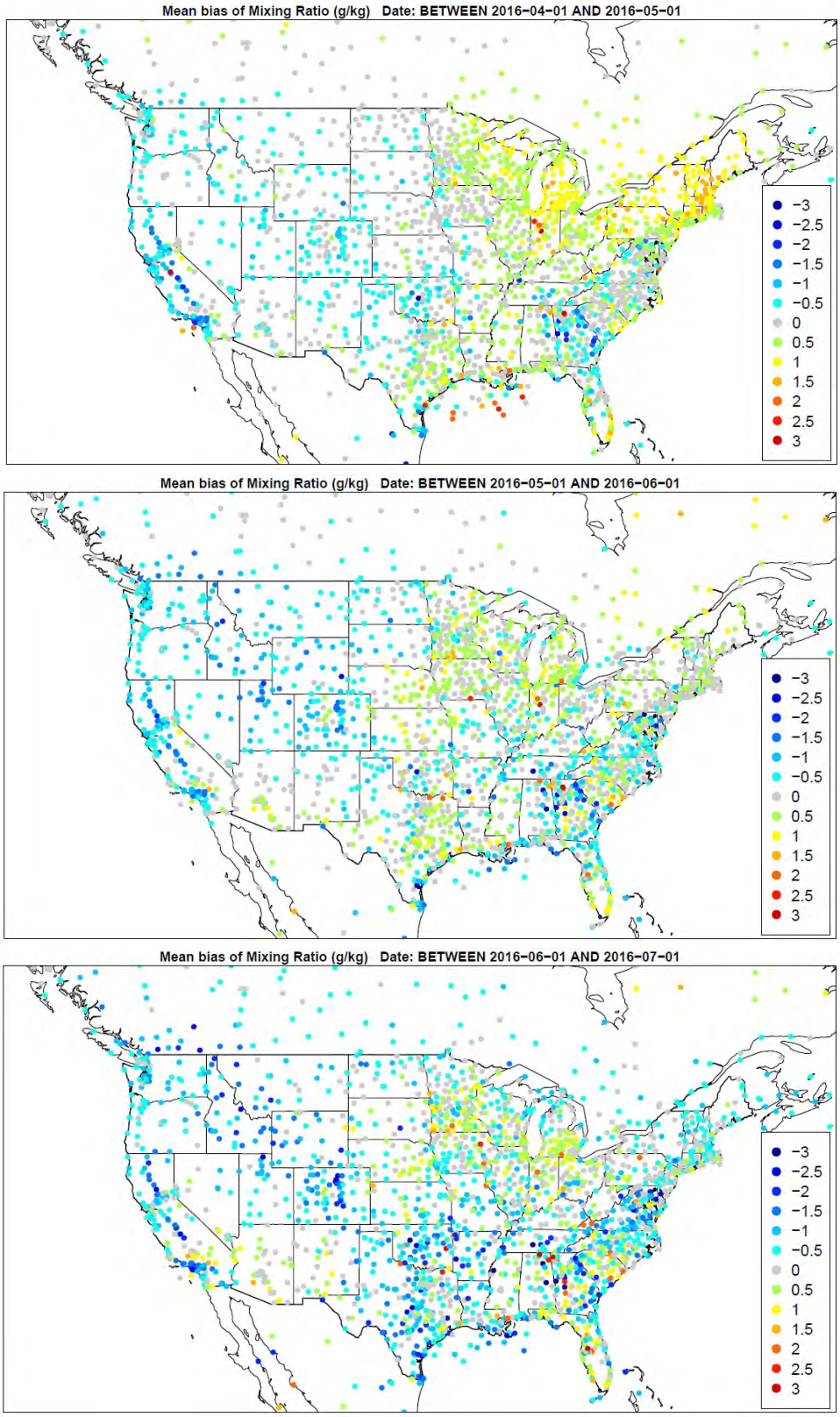

Figure 3.3.12. Spatial distribution of water vapor mixing ratio bias (g/kg) across daytime hours for the months of April, May, and June (top to bottom) for the 36NOAM domain.

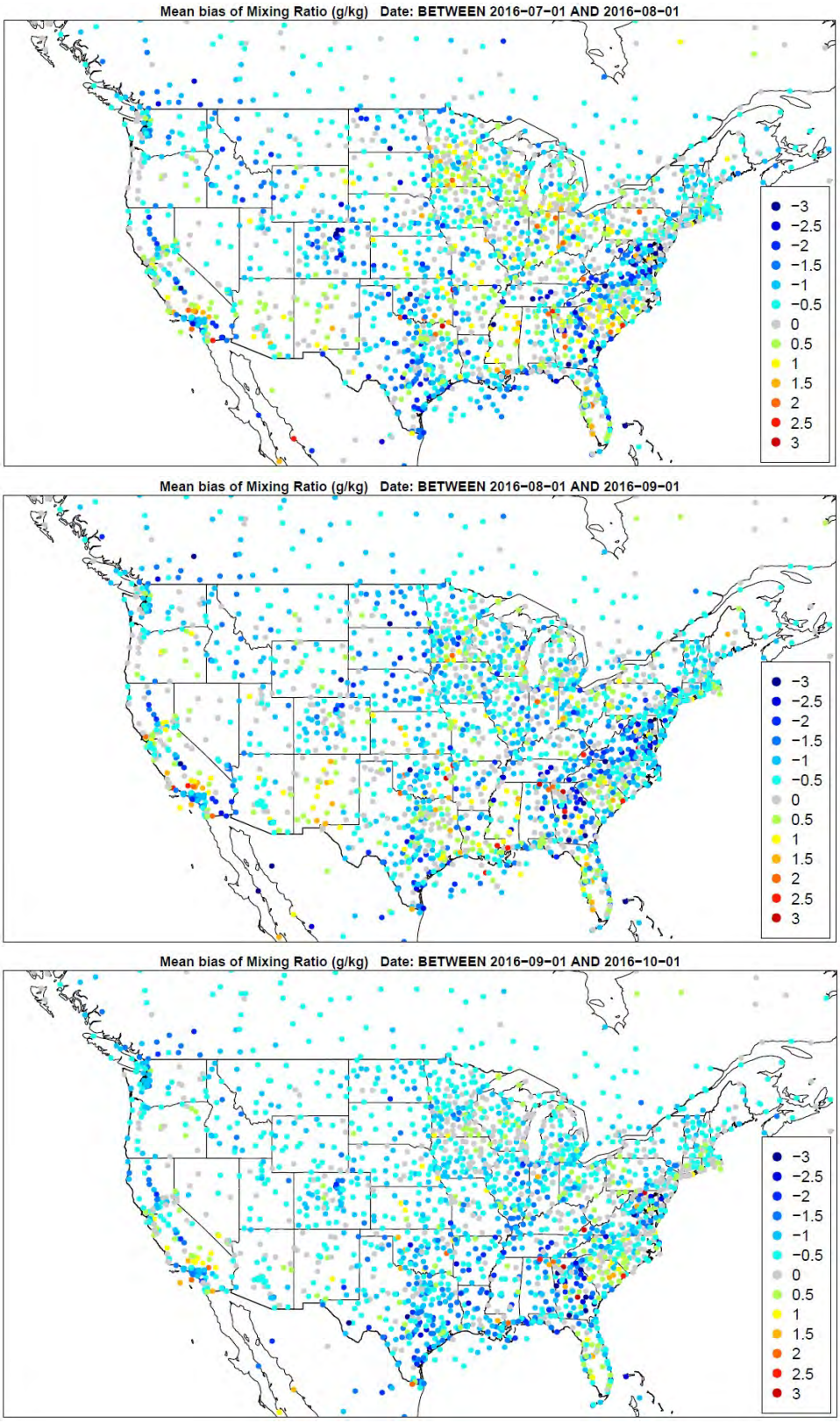

Figure 3.3.13. Spatial distribution of water vapor mixing ratio bias (g/kg) across daytime hours for the months of July, August, and September (top to bottom) for the 36NOAM domain.

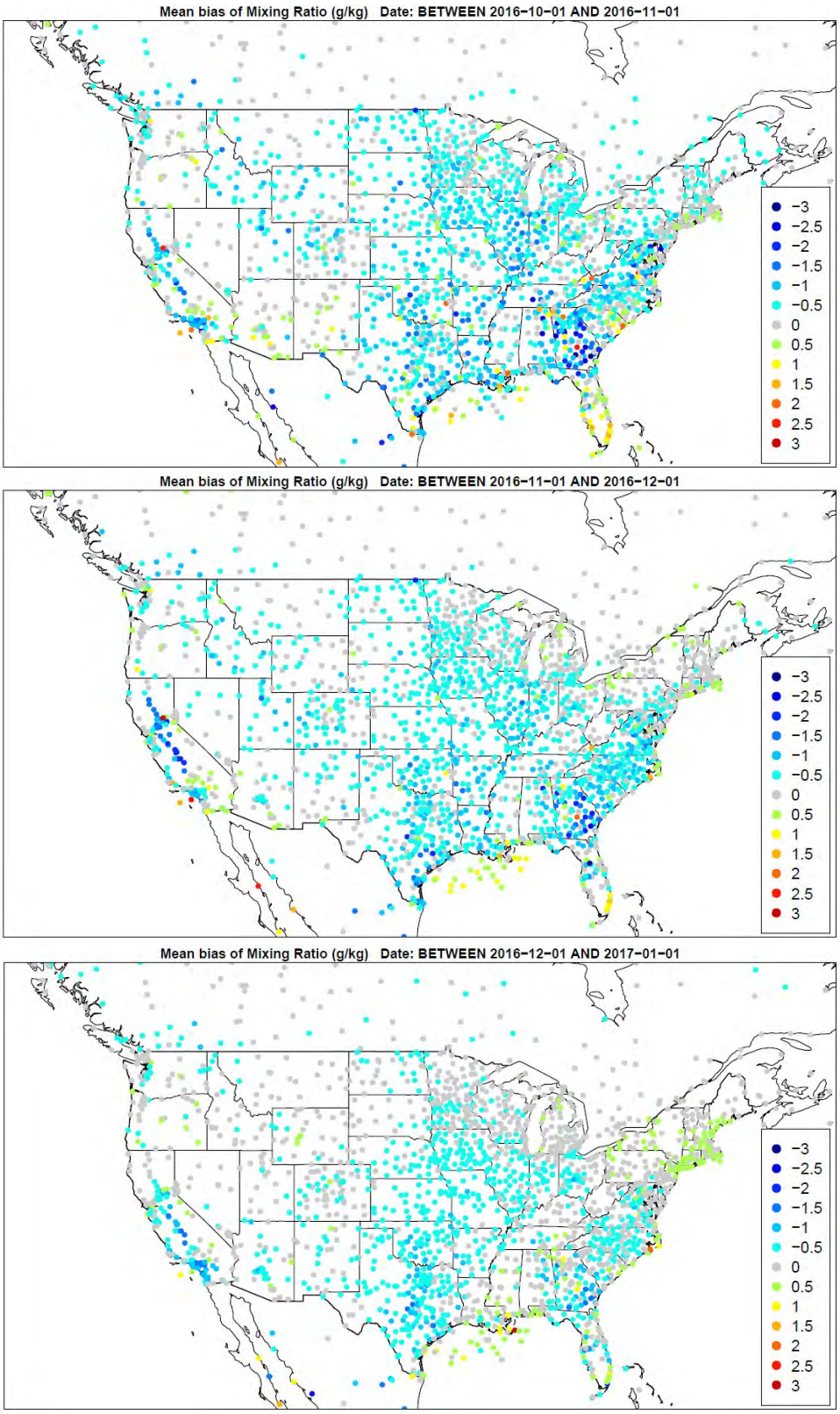

Figure 3.3.14. Spatial distribution of water vapor mixing ratio bias (g/kg) across daytime hours for October, November, and December (top to bottom) for the 36NOAM domain.

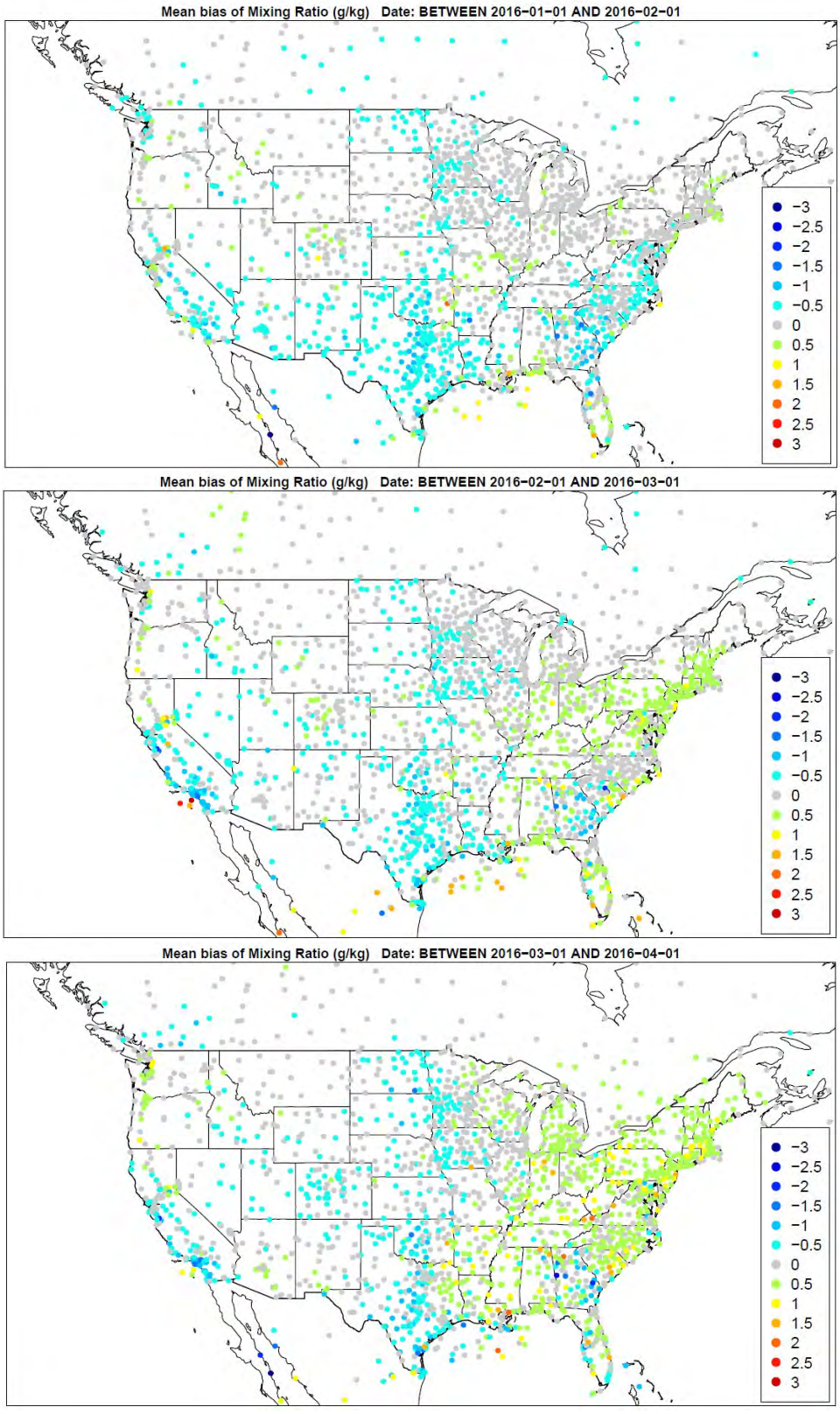

Figure 3.3.15. Spatial distribution of water vapor mixing ratio bias (g/kg) across daytime hours for the months of January, February, and March (top to bottom) for the 12US domain.

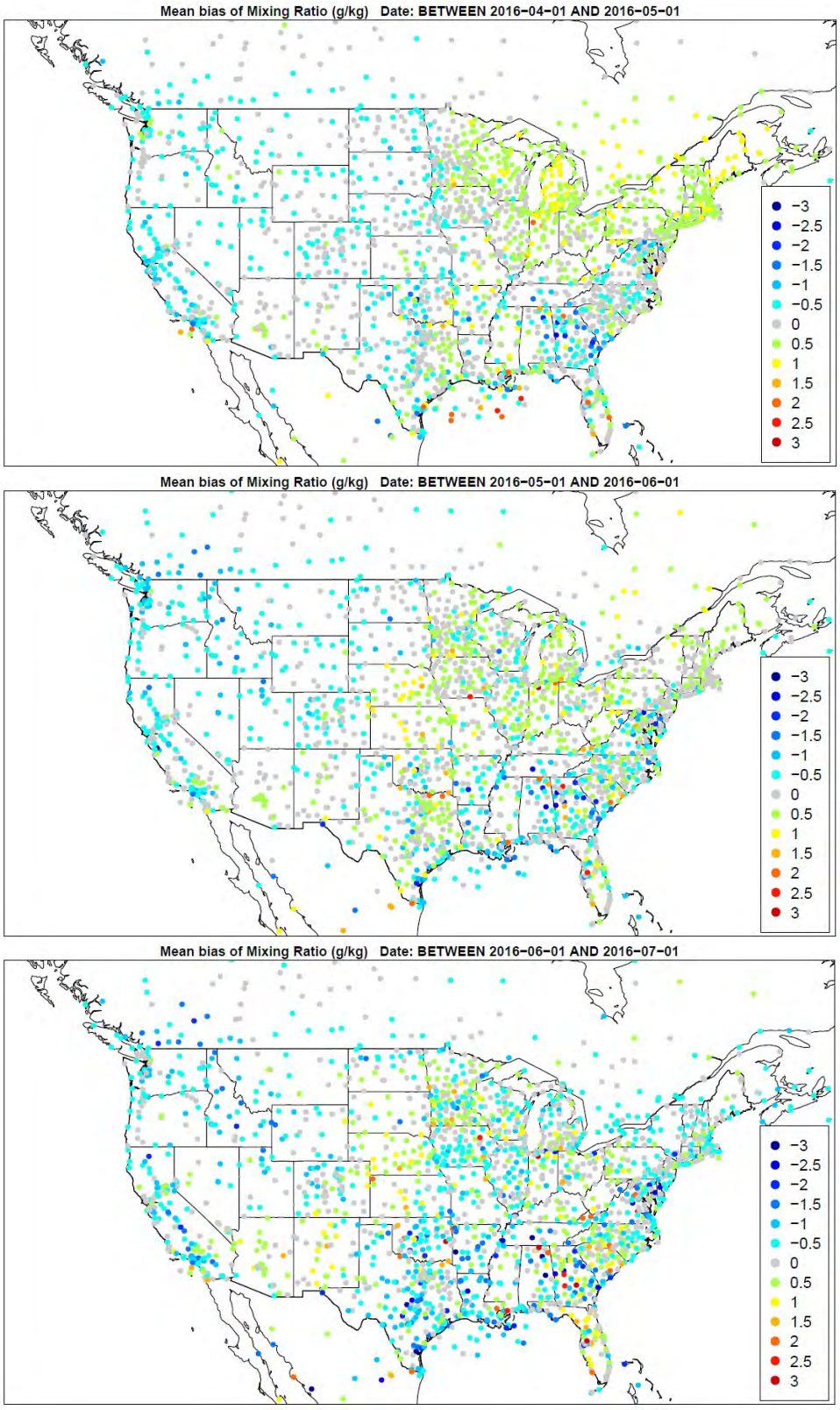

Figure 3.3.16. Spatial distribution of water vapor mixing ratio bias (g/kg) across daytime hours for the months of April, May, and June (top to bottom) for the 12US domain.

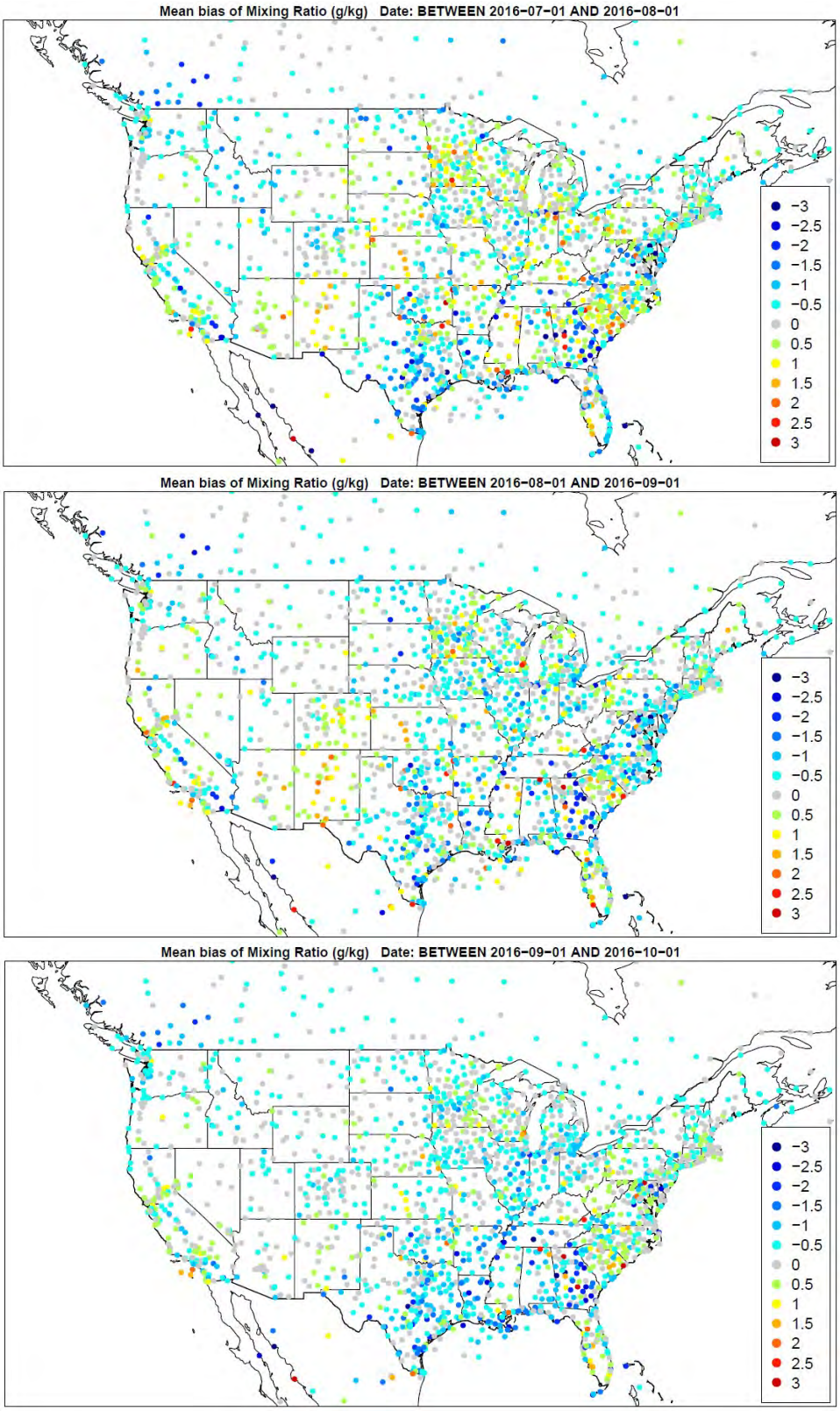

Figure 3.3.17. Spatial distribution of water vapor mixing ratio bias (g/kg) across daytime hours for the months of July, August, and September (top to bottom) for the 12US domain.

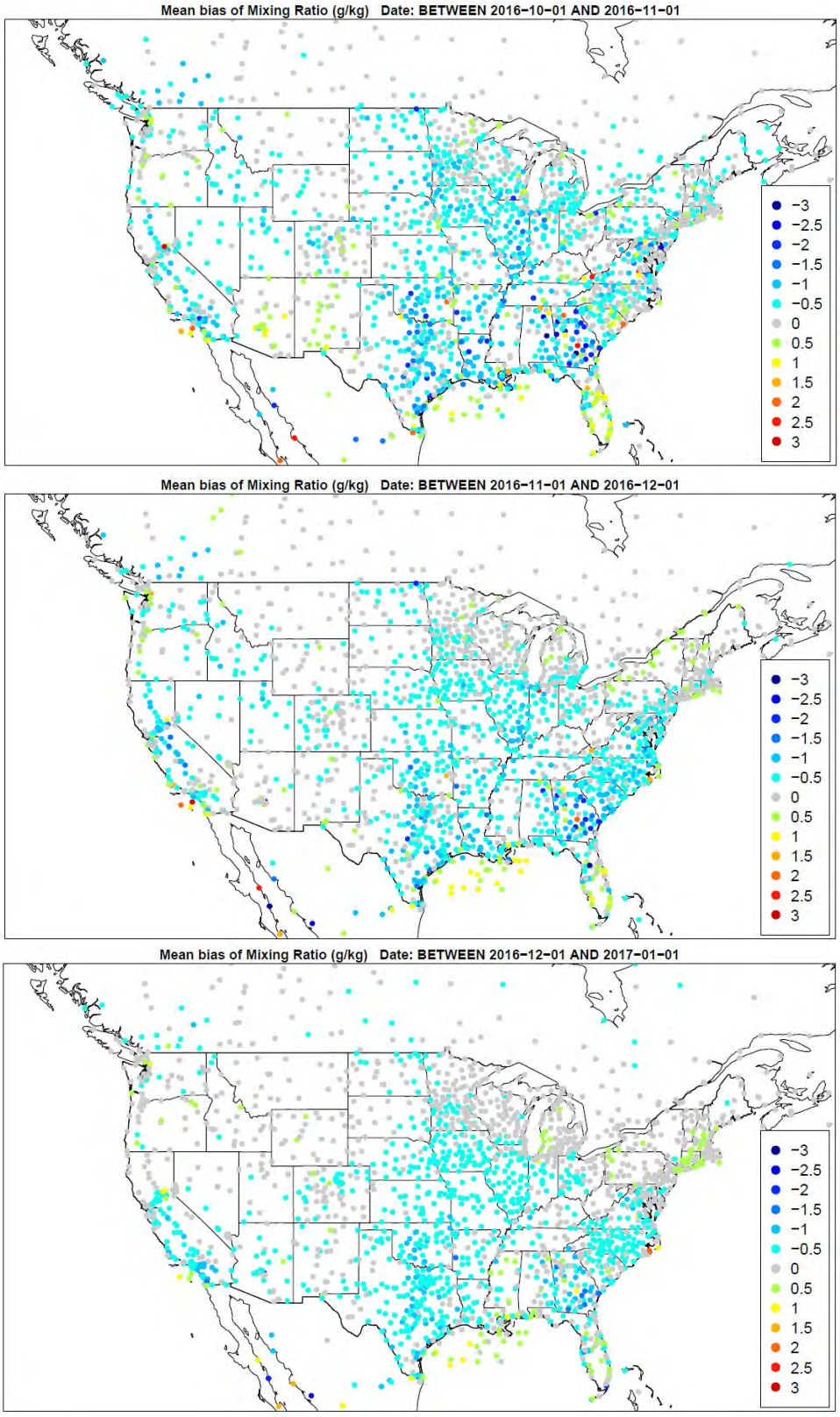

Figure 3.3.18. Spatial distribution of water vapor mixing ratio bias (g/kg) across daytime hours for the months of October, November, and December (top to bottom) for the 12US domain.

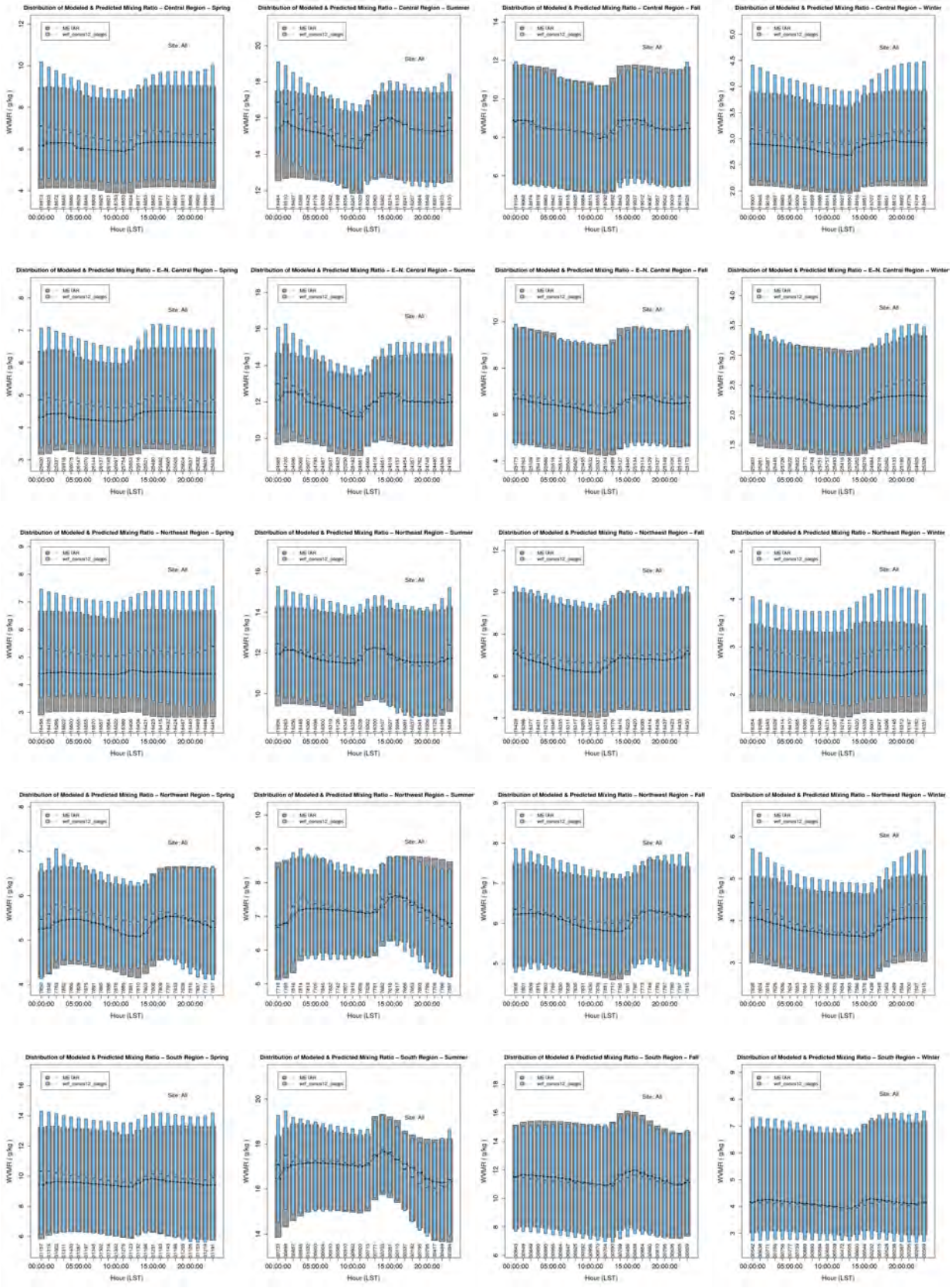
Distribution of Modeled & Predicted Mixing Ratio – Central Region – Spring
Distribution of Modeled & Predicted Mixing Ratio – Central Region – Summer
Distribution of Modeled & Predicted Mixing Ratio – Central Region – Fall
Distribution of Modeled & Predicted Mixing Ratio – Central Region – Winter
Distribution of Modeled & Predicted Mixing Ratio – E.-N. Central Region – Spring
Distribution of Modeled & Predicted Mixing Ratio – E.-N. Central Region – Summe
Distribution of Modeled & Predicted Mixing Ratio – E.-N. Central Region – Fall
Distribution of Modeled & Predicted Mixing Ratio – E.-N. Central Region – Winter
Distribution of Modeled & Predicted Mixing Ratio – Northeast Region – Spring
Distribution of Modeled & Predicted Mixing Ratio – Northeast Region – Summer
Distribution of Modeled & Predicted Mixing Ratio – Northeast Region – Fall
Distribution of Modeled & Predicted Mixing Ratio – Northeast Region – Winter
Distribution of Modeled & Predicted Mixing Ratio – Northwest Region – Spring
Distribution of Modeled & Predicted Mixing Ratio – Northwest Region – Summer
Distribution of Modeled & Predicted Mixing Ratio – Northwest Region – Fall
Distribution of Modeled & Predicted Mixing Ratio – Northwest Region – Winter
Distribution of Modeled & Predicted Mixing Ratio – South Region – Spring
Distribution of Modeled & Predicted Mixing Ratio – South Region – Summer
Distribution of Modeled & Predicted Mixing Ratio – South Region – Fall
Distribution of Modeled & Predicted Mixing Ratio – South Region – Winter
MS IAH
wrf_conus12_jaegis
Site: All
WVMR (g/kg)
Hour (LST)

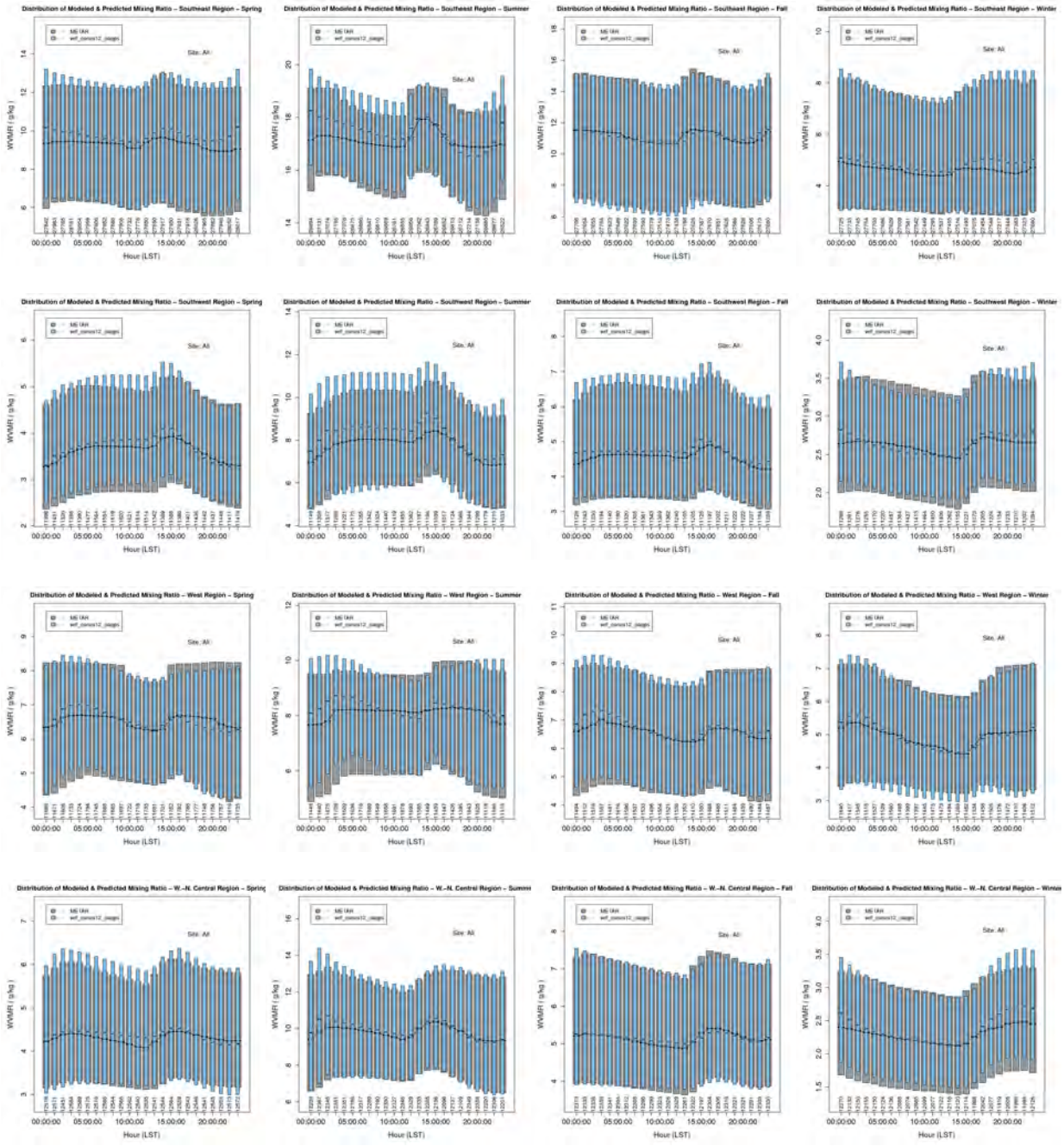

Figure 3.3.19. Hourly average distribution of observed and predicted water vapor mixing ratio for the 12US domain in the Central, East-North Central, Northeast, Northwest, South, Southeast, Southwest, West, and West-North Central (top to bottom) regions for each season (Spring, Summer, Fall, Winter, L-R).

Climate Region	Season	Mean Obs	Mean Mod	MB	MAE	NMB	NME	RMSE
Northeast	Spring	4.13	4.10	-0.03	1.26	-0.74	30.43	1.81
Northeast	Summer	3.57	3.57	0.00	1.11	0.12	31.21	1.63
Northeast	Fall	3.87	4.00	0.14	1.22	3.56	31.55	1.78
Northeast	Winter	4.46	4.59	0.13	1.40	2.89	31.42	2.01
West-North Central	Spring	5.32	4.75	-0.57	1.41	-10.67	26.42	1.88
West-North Central	Summer	4.49	4.18	-0.31	1.32	-6.90	29.36	1.81
West-North Central	Fall	4.75	4.45	-0.31	1.29	-6.46	27.18	1.74
West-North Central	Winter	5.31	4.63	-0.68	1.51	-12.81	28.42	2.06
Northwest	Spring	4.01	3.72	-0.29	1.33	-7.32	33.24	1.76
Northwest	Summer	3.80	3.53	-0.27	1.19	-7.08	31.36	1.56
Northwest	Fall	3.69	3.43	-0.26	1.31	-7.00	35.45	1.72
Northwest	Winter	3.67	3.32	-0.35	1.41	-9.61	38.25	1.87
Central	Spring	4.16	4.21	0.05	1.11	1.16	26.58	1.47
Central	Summer	3.18	3.19	0.01	0.95	0.18	29.74	1.28
Central	Fall	3.62	3.84	0.22	1.00	5.94	27.60	1.32
Central	Winter	4.41	4.45	0.04	1.08	0.90	24.49	1.43
South	Spring	4.54	4.39	-0.15	1.23	-3.32	27.14	1.66
South	Summer	3.81	3.75	-0.06	1.09	-1.68	28.51	1.48
South	Fall	3.86	3.82	-0.04	1.02	-0.92	26.54	1.37
South	Winter	4.28	4.13	-0.15	1.10	-3.47	25.74	1.47
Southeast	Spring	3.57	3.78	0.21	1.11	5.87	31.09	1.46
Southeast	Summer	3.04	3.05	0.01	1.01	0.26	33.33	1.36
Southeast	Fall	3.31	3.49	0.19	1.05	5.72	31.86	1.41
Southeast	Winter	3.65	3.94	0.29	1.15	7.93	31.53	1.53
Southwest	Spring	4.68	4.12	-0.55	1.60	-11.80	34.21	2.17
Southwest	Summer	4.08	3.54	-0.55	1.54	-13.43	37.78	2.09
Southwest	Fall	4.16	3.61	-0.55	1.47	-13.25	35.35	2.02
Southwest	Winter	4.19	3.64	-0.55	1.55	-13.21	37.03	2.18
East-North Central	Spring	4.46	4.52	0.06	1.14	1.29	25.50	1.49
East-North Central	Summer	3.67	3.90	0.22	1.07	6.12	29.01	1.42
East-North Central	Fall	4.09	4.47	0.38	1.12	9.21	27.41	1.48
East-North Central	Winter	4.69	4.75	0.06	1.17	1.20	24.93	1.55
West	Spring	4.19	3.88	-0.31	1.40	-7.38	33.52	1.89
West	Summer	4.08	3.64	-0.45	1.33	-10.94	32.54	1.77
West	Fall	3.68	3.34	-0.35	1.32	-9.39	35.91	1.80
West	Winter	3.53	3.28	-0.25	1.39	-7.12	39.20	1.90

Table 3.3.1. Mean observed, mean modeled, mean bias (MB), mean absolute error (MAE), normalized mean bias (NMB), normalized mean error (NME), and root mean square error (RMSE) for water vapor mixing ratio (g/kg) for the 12US simulation.

3.4 Precipitation

Monthly total rainfall is plotted for each grid cell to assess how well the model captures the spatial variability and magnitude of convective and non-convective rainfall. As described earlier, the PRISM estimations for rainfall are only within the continental United States. WRF rainfall estimates by month are shown for all grid cells in the domain. Monthly total estimates are shown for the 36NOAM domain (Figures 3.4.1 through 3.4.12) and 12US domain (Figures 3.4.13 through 3.4.24).

In general, WRF performs adequately in terms of the spatial patterns and magnitude of precipitation across the US throughout the year. Both simulations, however, have difficulty simulating precipitation in areas of complex terrain (e.g., northern CA and the Pacific Northwest). Both simulations tend to underpredict precipitation during periods of increased convective activity (Jun – Oct), with notable underpredictions observed in the eastern US. In general, both simulations overpredict precipitation across the western areas of the country during most months, with notable overpredictions of precipitation in the southwest during July and August. Overpredictions are observed during the Spring and Fall months across the Northeast and Mid-MS/OH Valley regions. General underpredictions are observed across the Deep South and Southern Plains throughout much of the year.

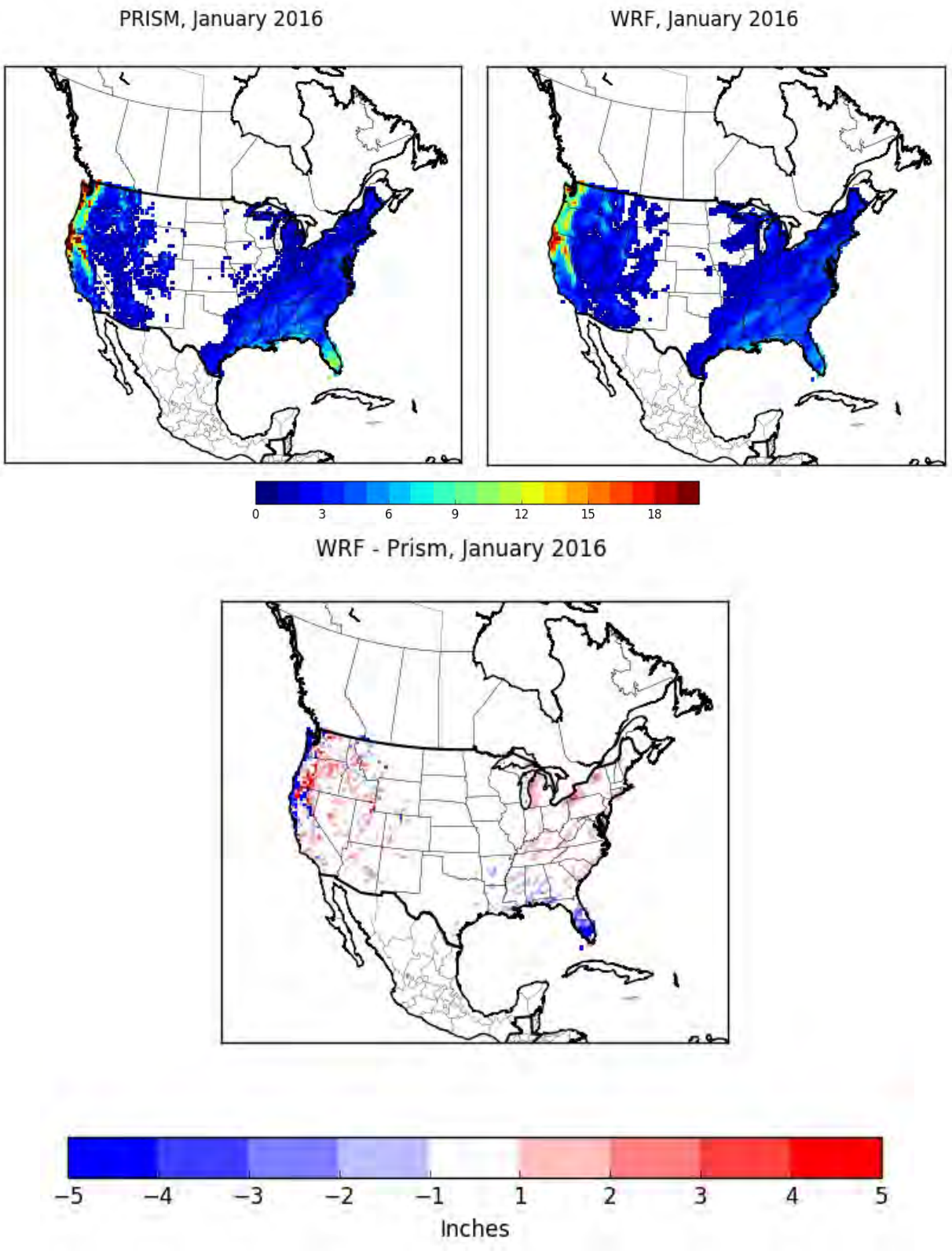

Figure 3.4.1. PRISM analysis (top left) and WRF (top right) estimated monthly total rainfall (in) and the difference (bottom) for January for the 36NOAM simulation.

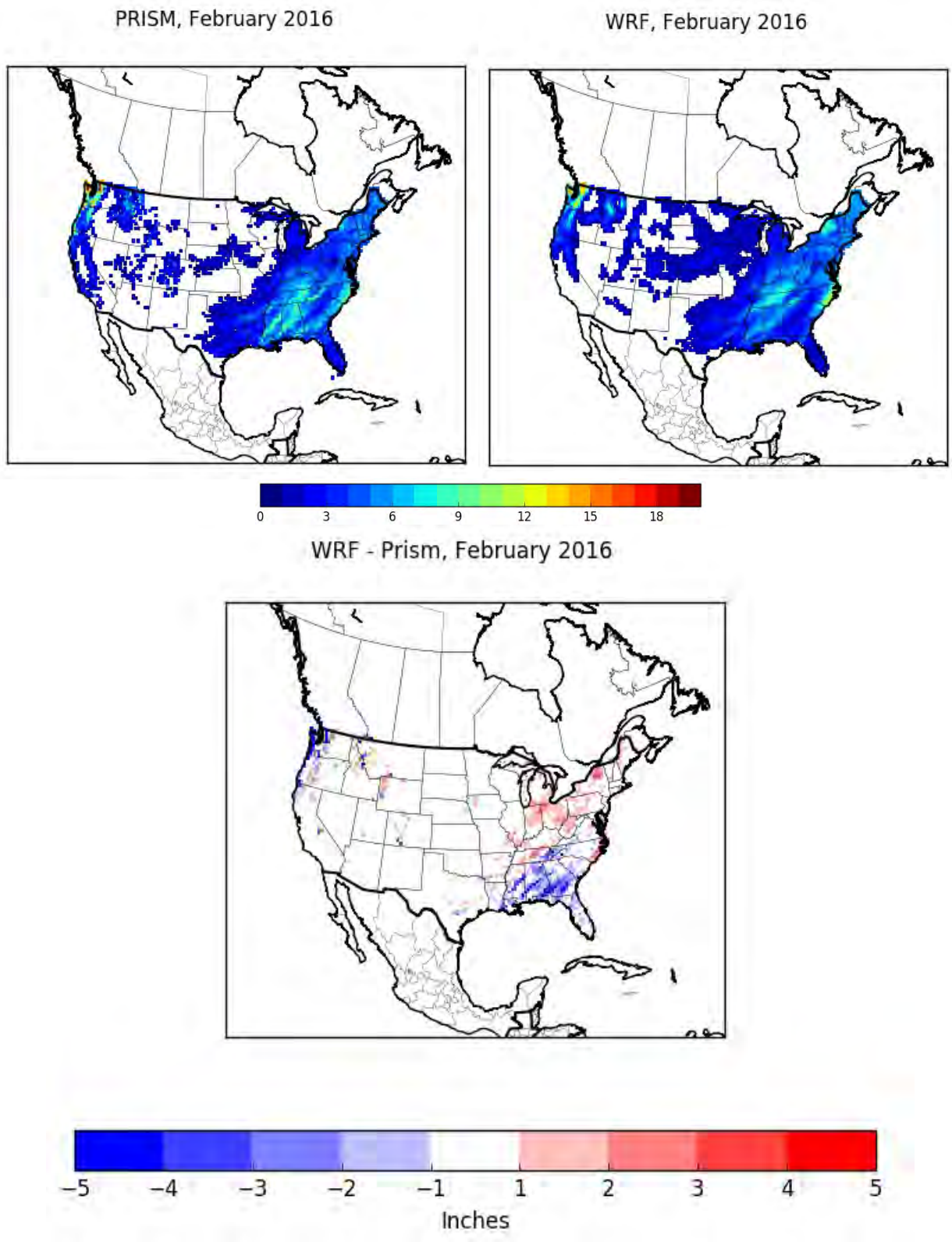

Figure 3.4.2. PRISM analysis (top left) and WRF (top right) estimated monthly total rainfall (in) and the difference (bottom) for February for the 36NOAM simulation.

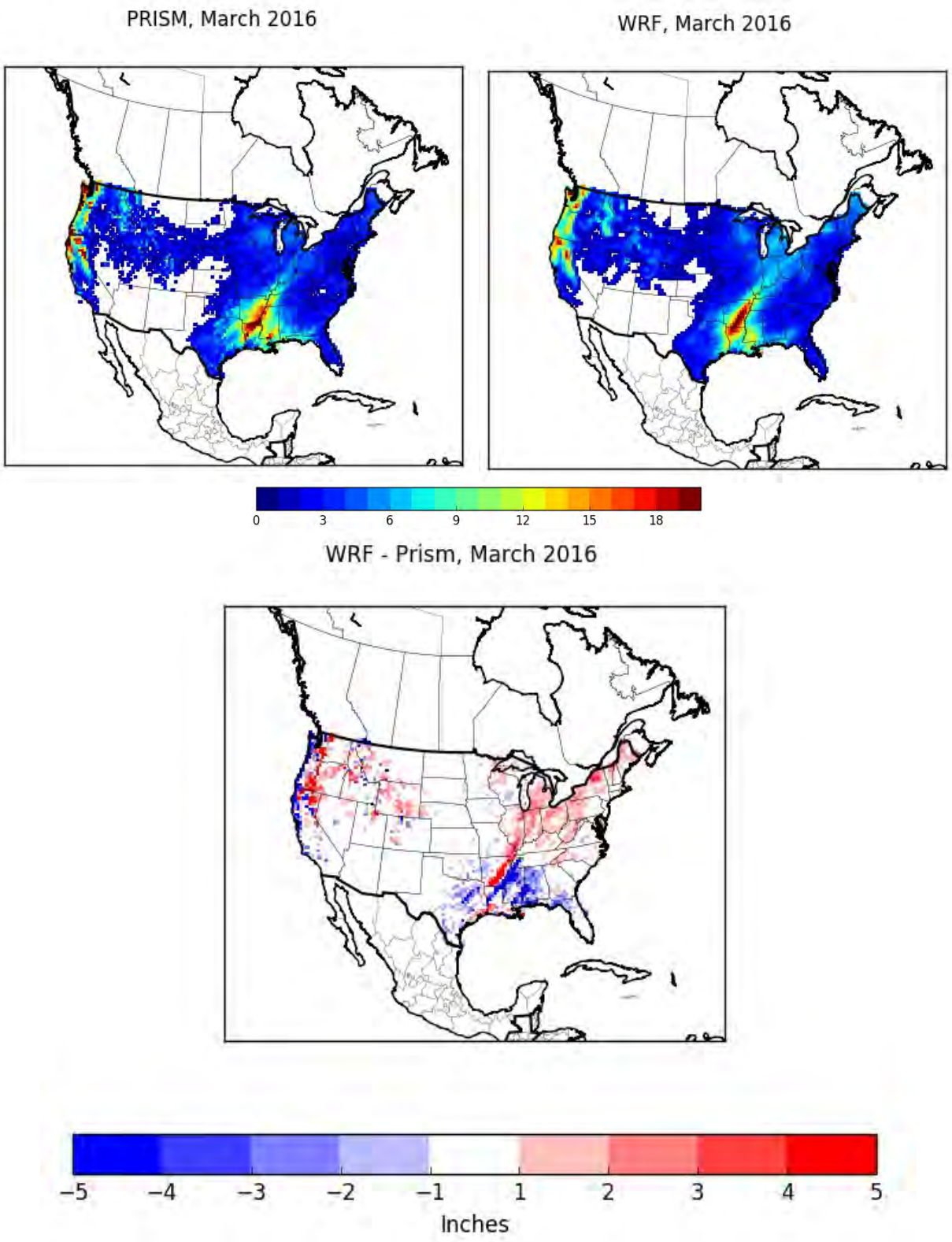

Figure 3.4.3. PRISM analysis (top left) and WRF (top right) estimated monthly total rainfall (in) and the difference (bottom) for March for the 36NOAM simulation.

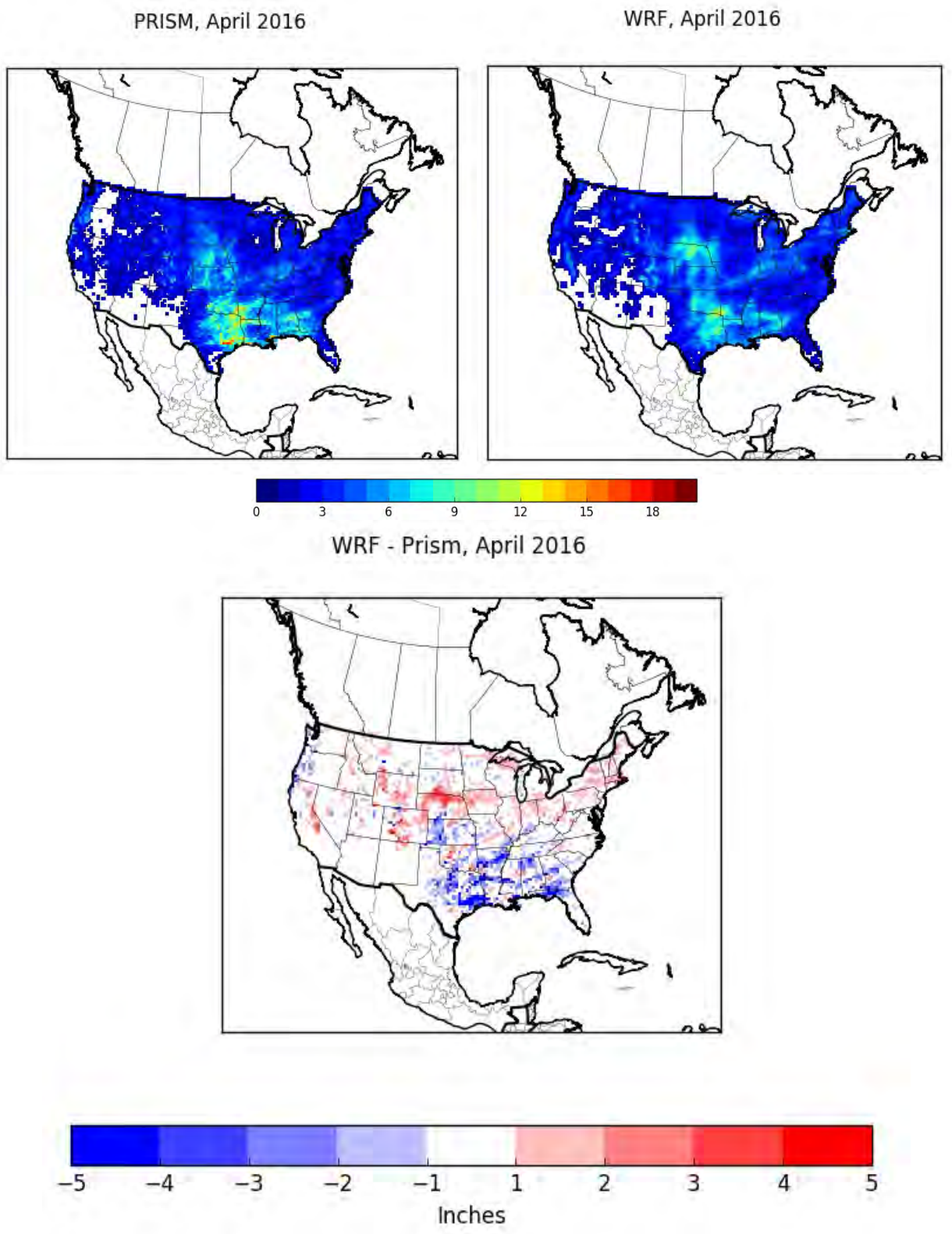

Figure 3.4.4. PRISM analysis (top left) and WRF (top right) estimated monthly total rainfall (in) and the difference (bottom) for April for the 36NOAM simulation.

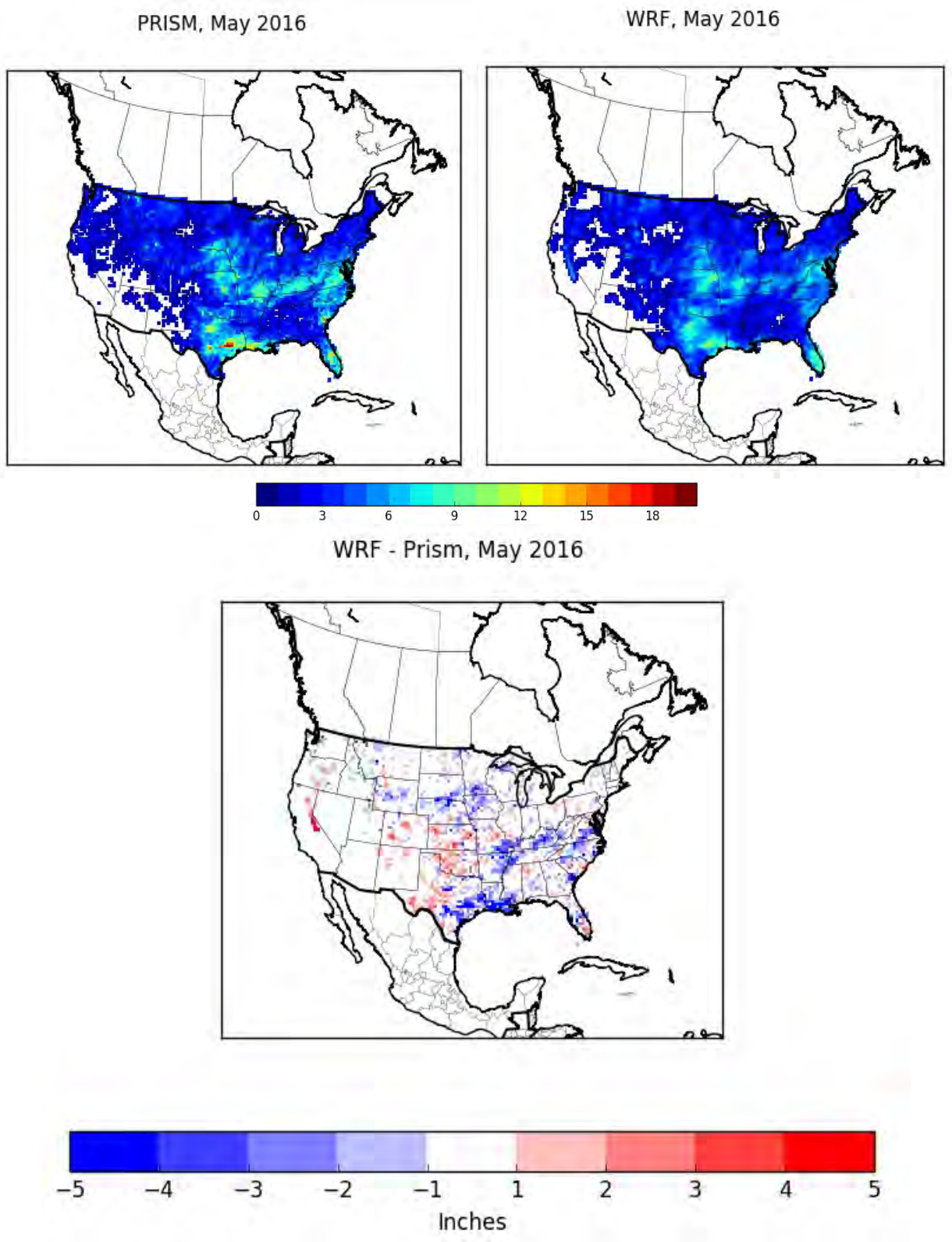

Figure 3.4.5. PRISM analysis (top left) and WRF (top right) estimated monthly total rainfall (in) and the difference (bottom) for May for the 36NOAM simulation.

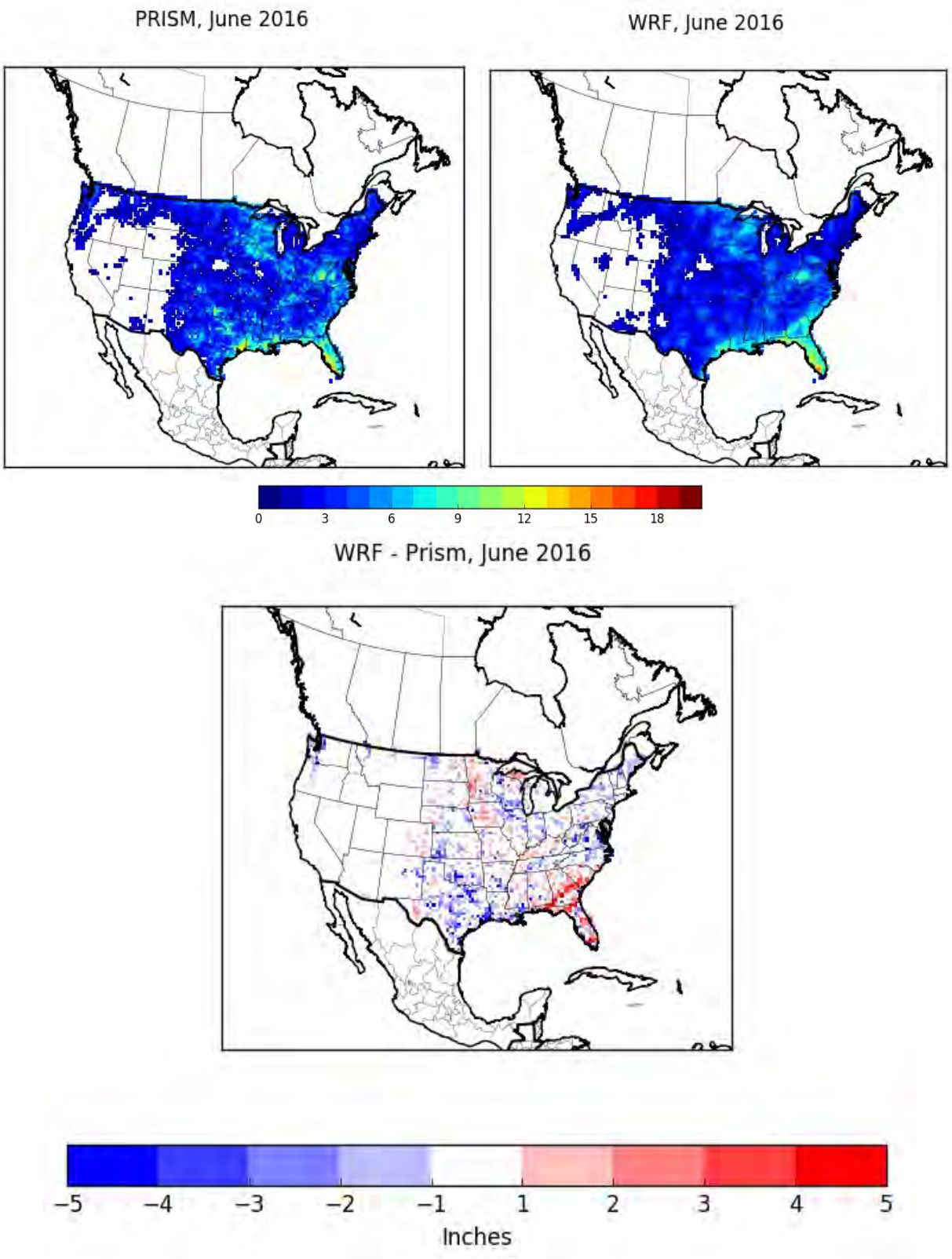

Figure 3.4.6. PRISM analysis (top left) and WRF (top right) estimated monthly total rainfall (in) and the difference (bottom) for June for the 36NOAM simulation.

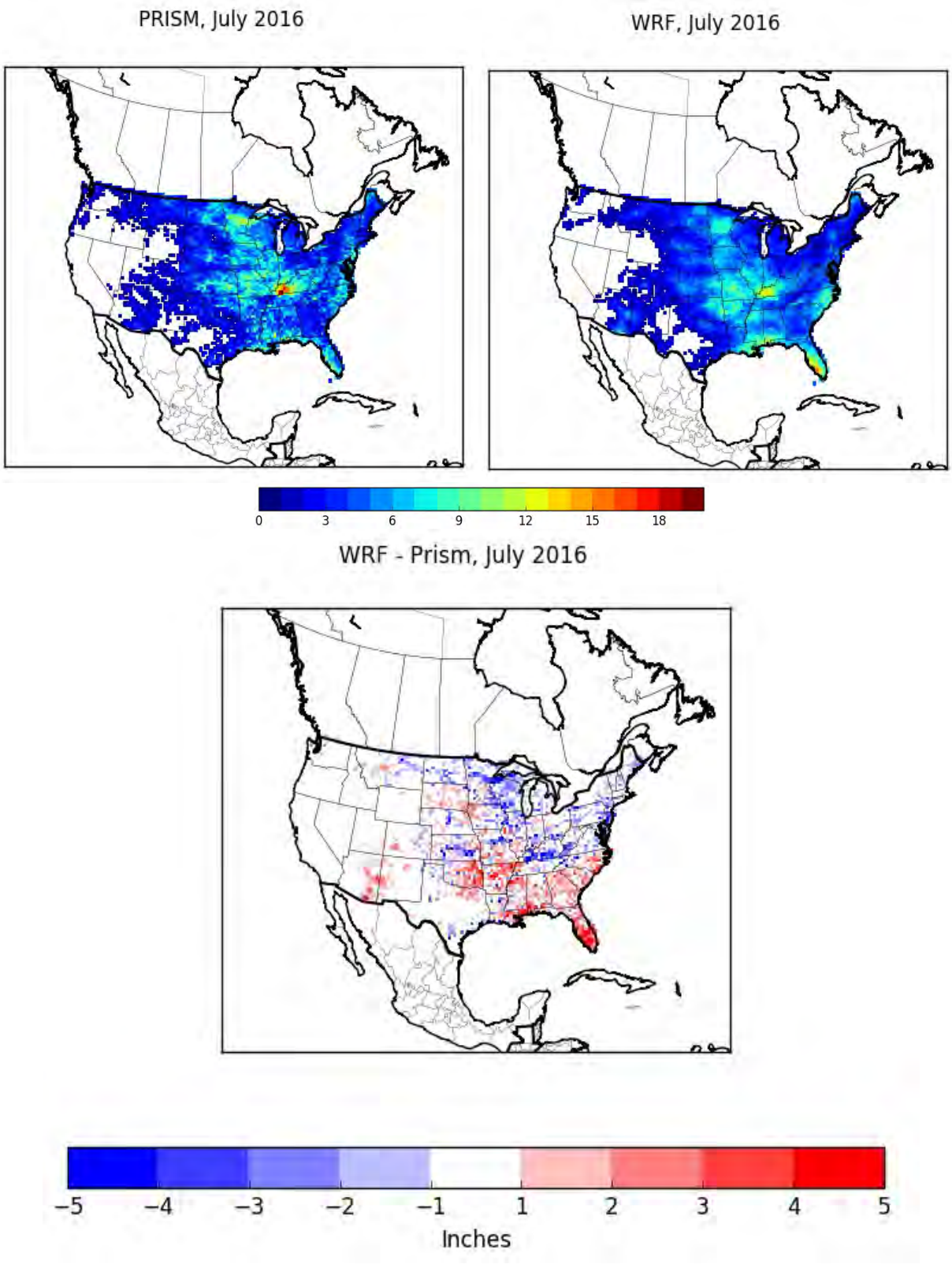

Figure 3.4.7. PRISM analysis (top left) and WRF (top right) estimated monthly total rainfall (in) and the difference (bottom) for July for the 36NOAM simulation.

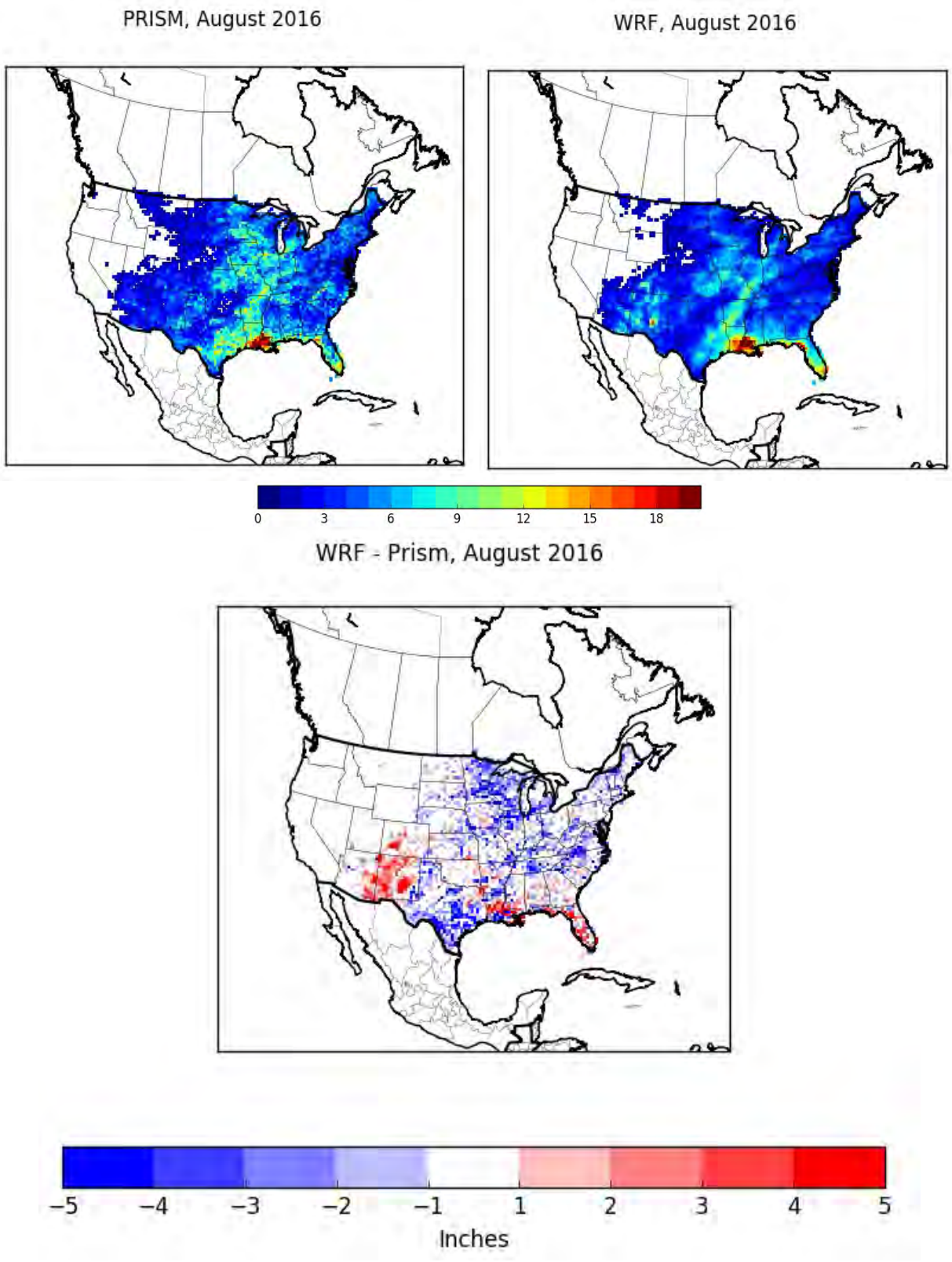

Figure 3.4.8. PRISM analysis (top left) and WRF (top right) estimated monthly total rainfall (in) and the difference (bottom) for August for the 36NOAM simulation.

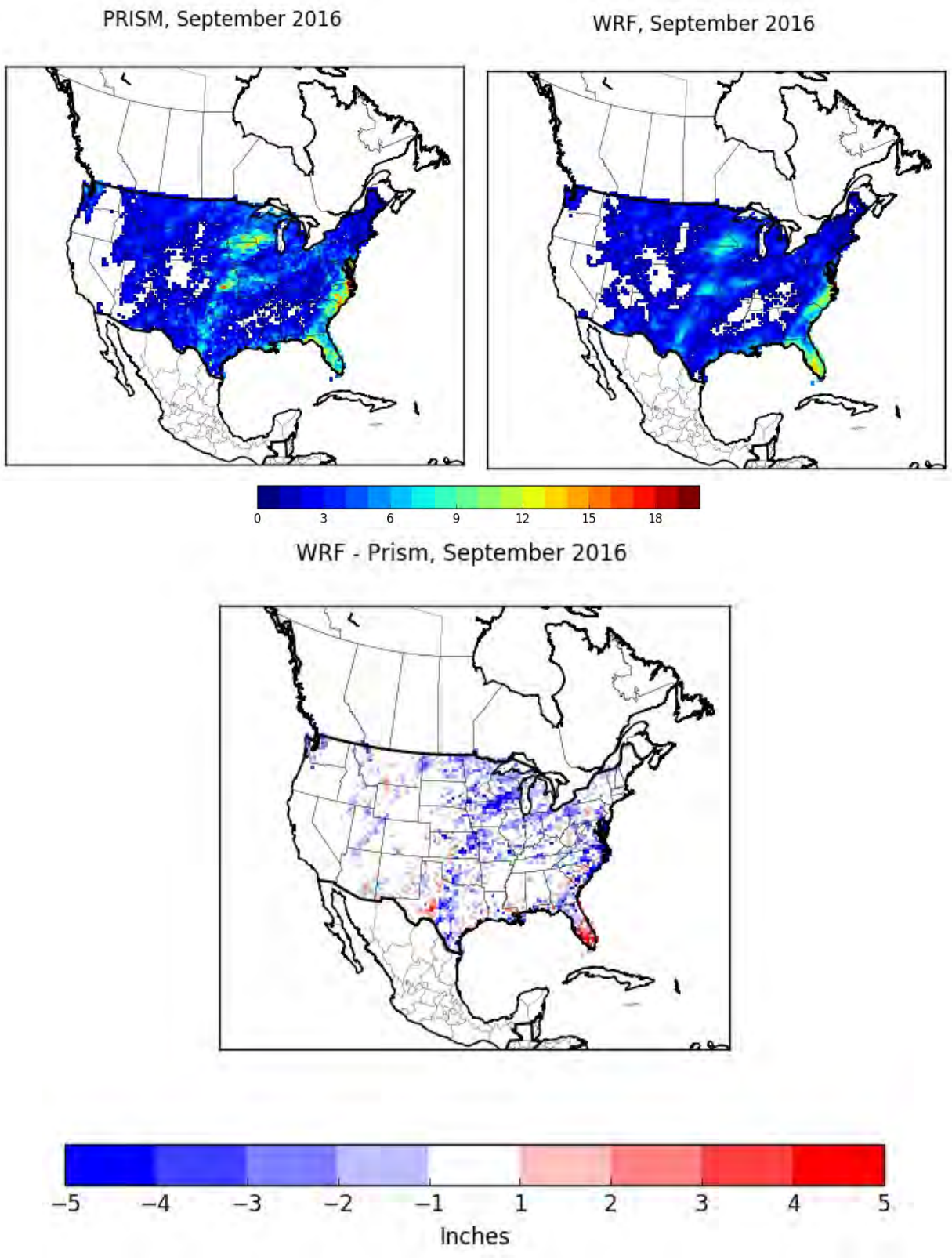

Figure 3.4.9. PRISM analysis (top left) and WRF (top right) estimated monthly total rainfall (in) and the difference (bottom) for September for the 36NOAM simulation.

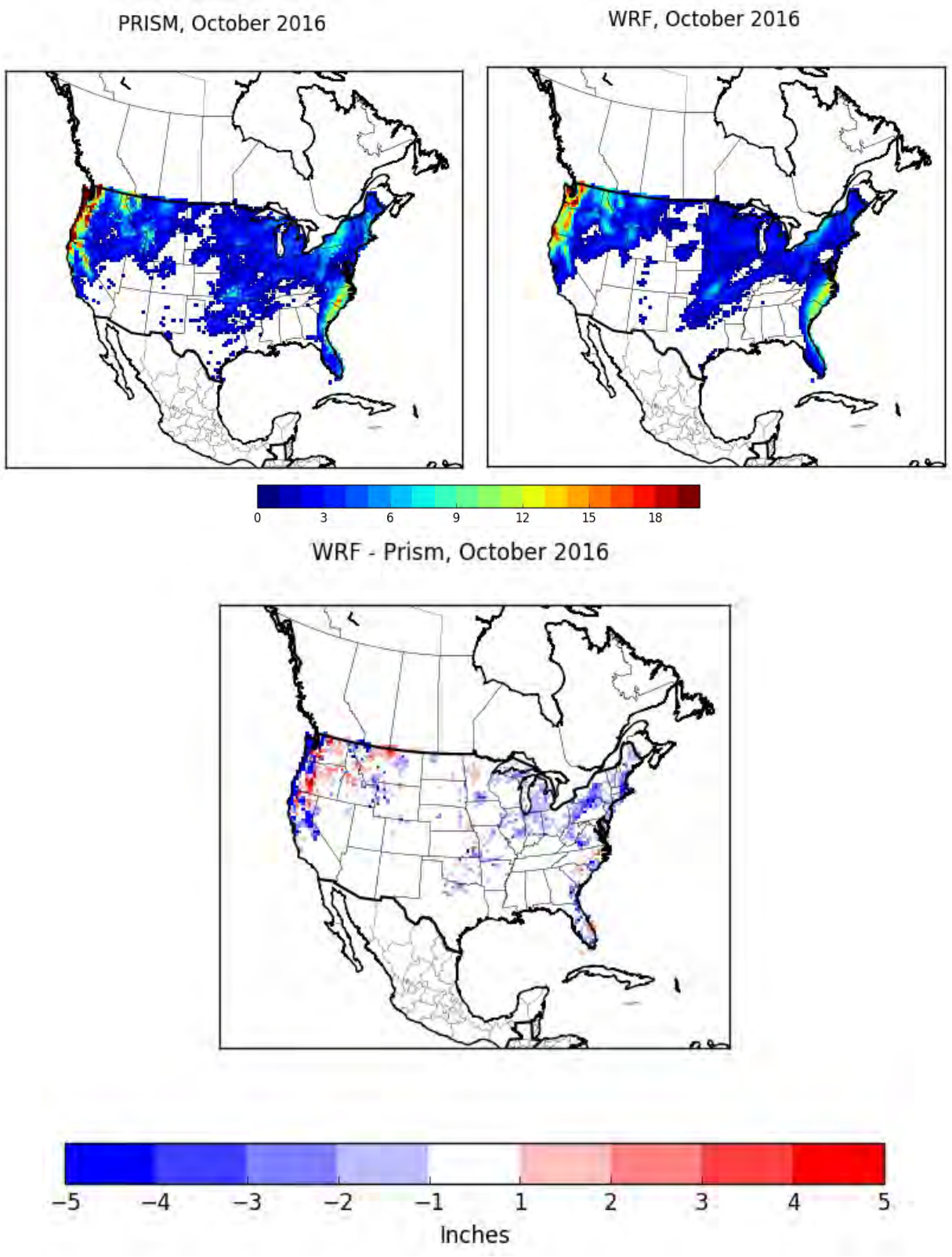

Figure 3.4.10. PRISM analysis (top left) and WRF (top right) estimated monthly total rainfall (in) and the difference (bottom) for October for the 36NOAM simulation.

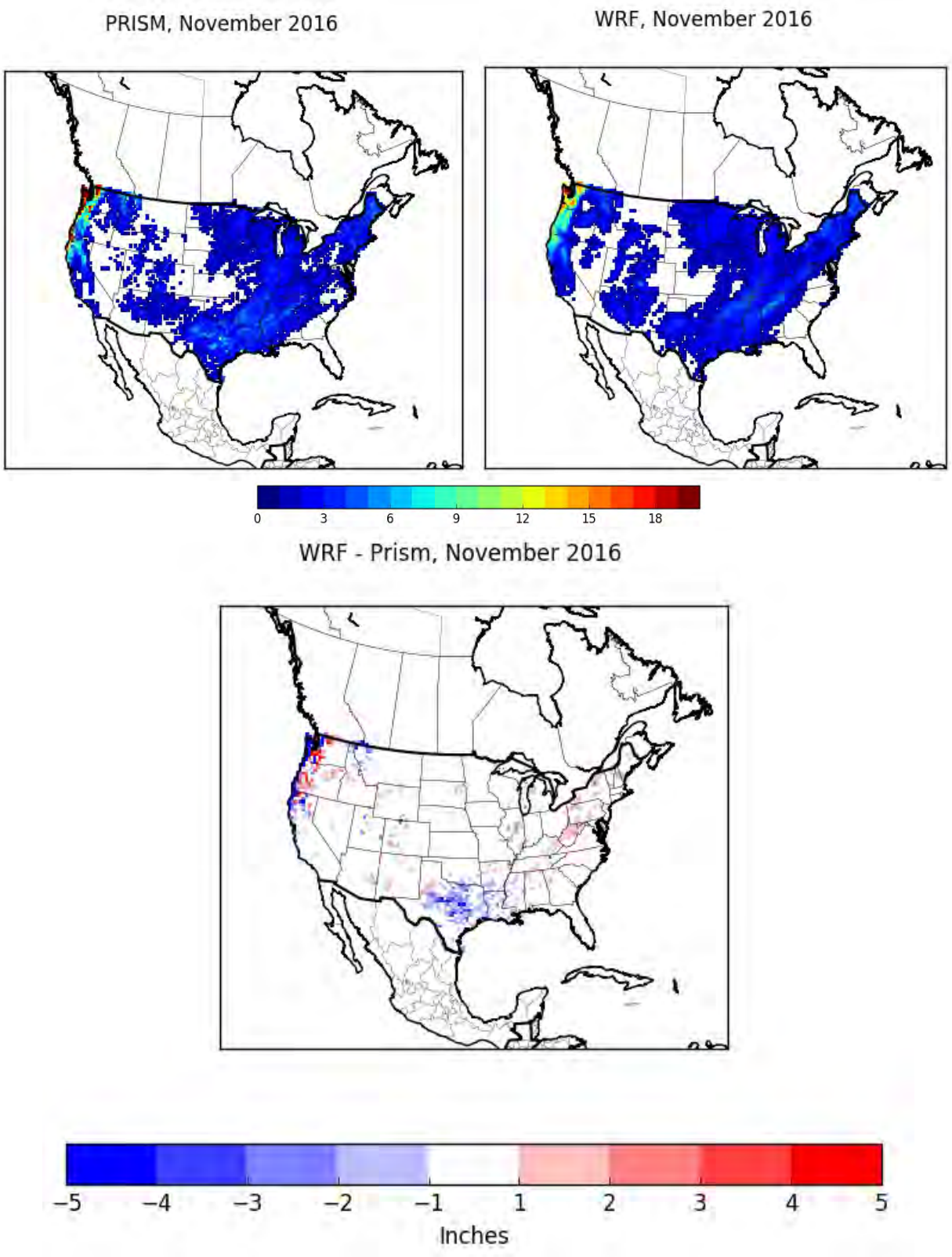

Figure 3.4.11. PRISM analysis (top left) and WRF (top right) estimated monthly total rainfall (in) and the difference (bottom) for November for the 36NOAM simulation.

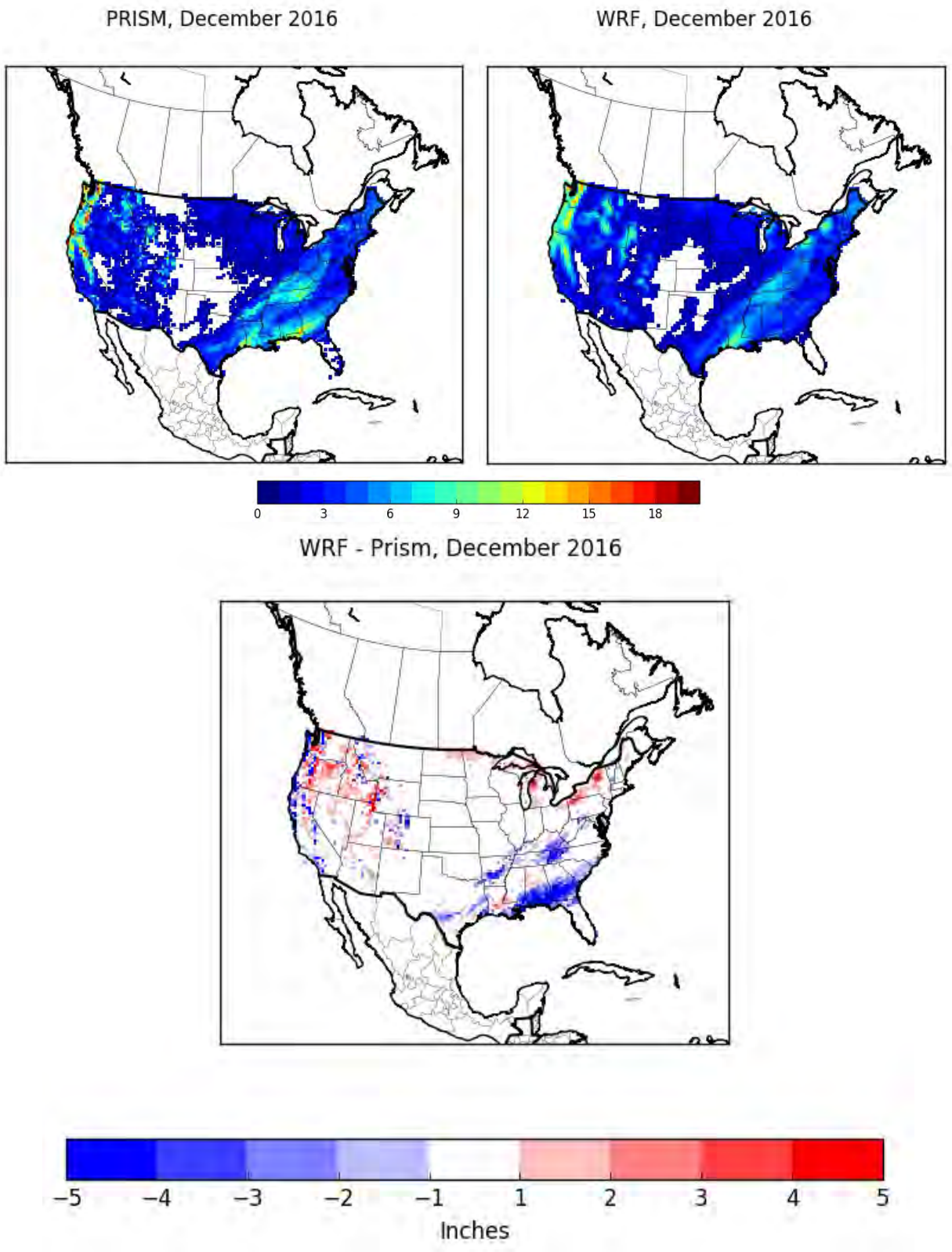

Figure 3.4.12. PRISM analysis (top left) and WRF (top right) estimated monthly total rainfall (in) and the difference (bottom) for November for the 36NOAM simulation.

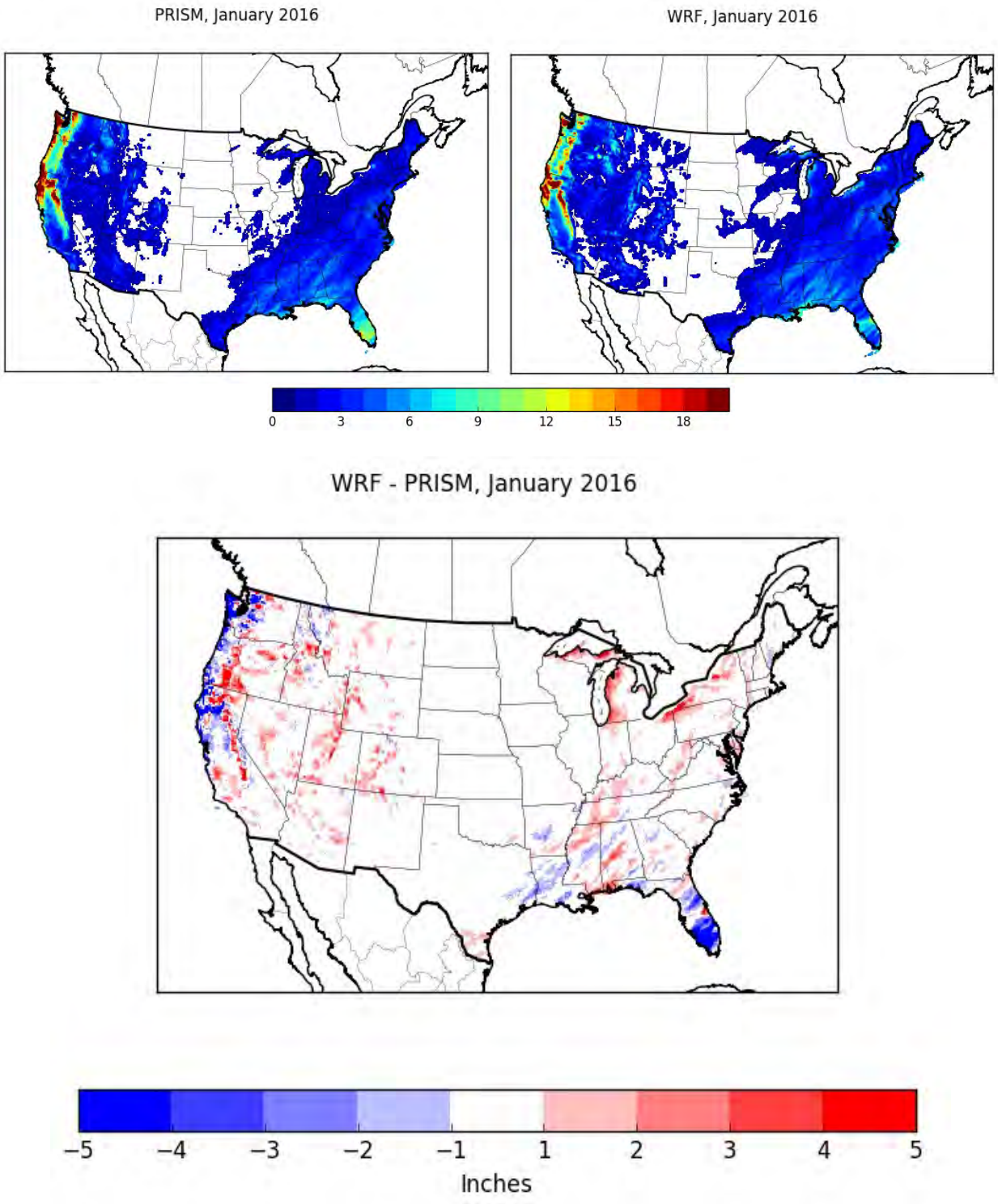

Figure 3.4.13. PRISM analysis (top left) and WRF (top right) estimated monthly total rainfall (in) and the difference (bottom) for January for the 12US simulation.

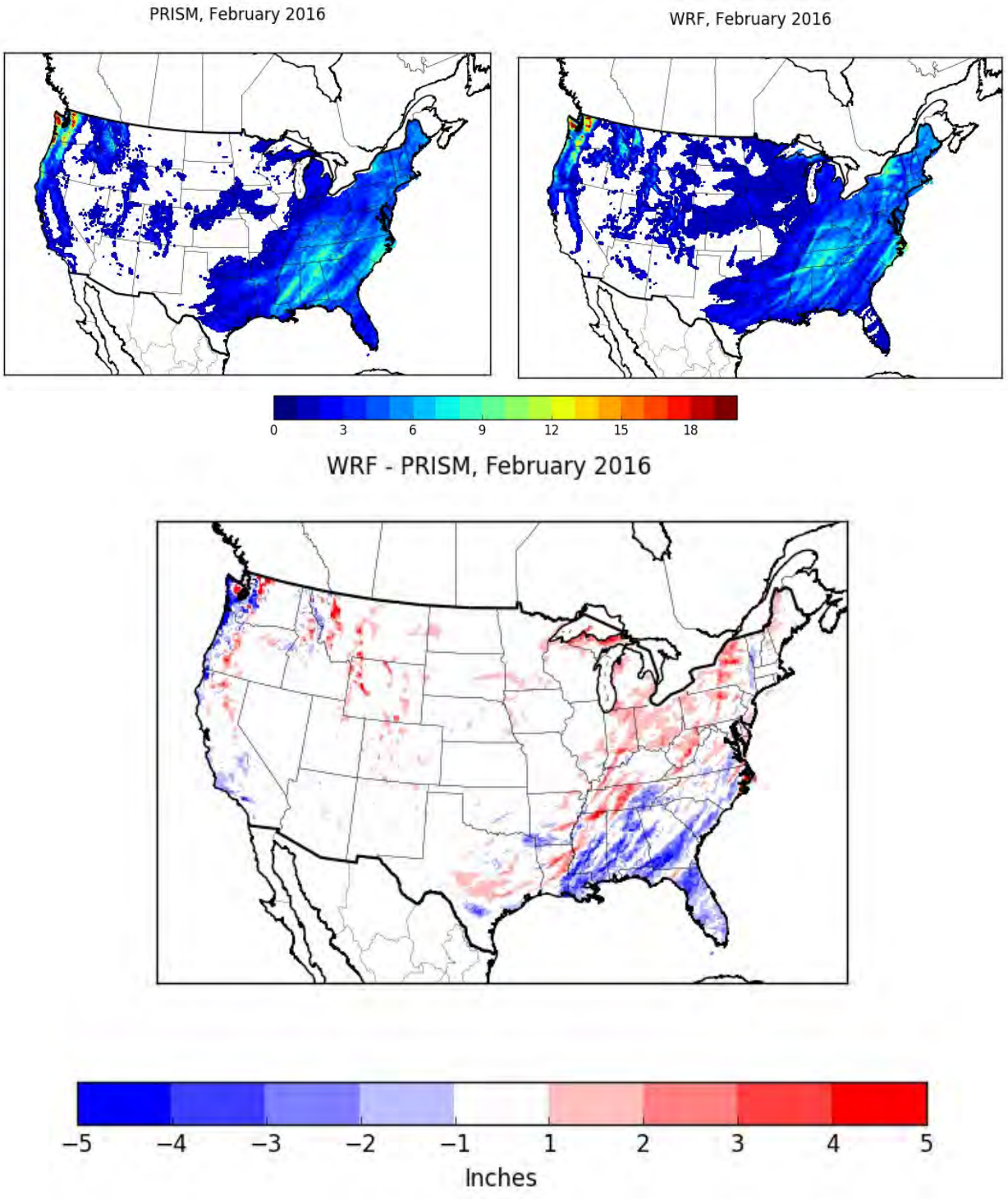

3.4.14. PRISM analysis (top left) and WRF (top right) estimated monthly total rainfall (in) and the difference (bottom) for February for the 12US simulation.

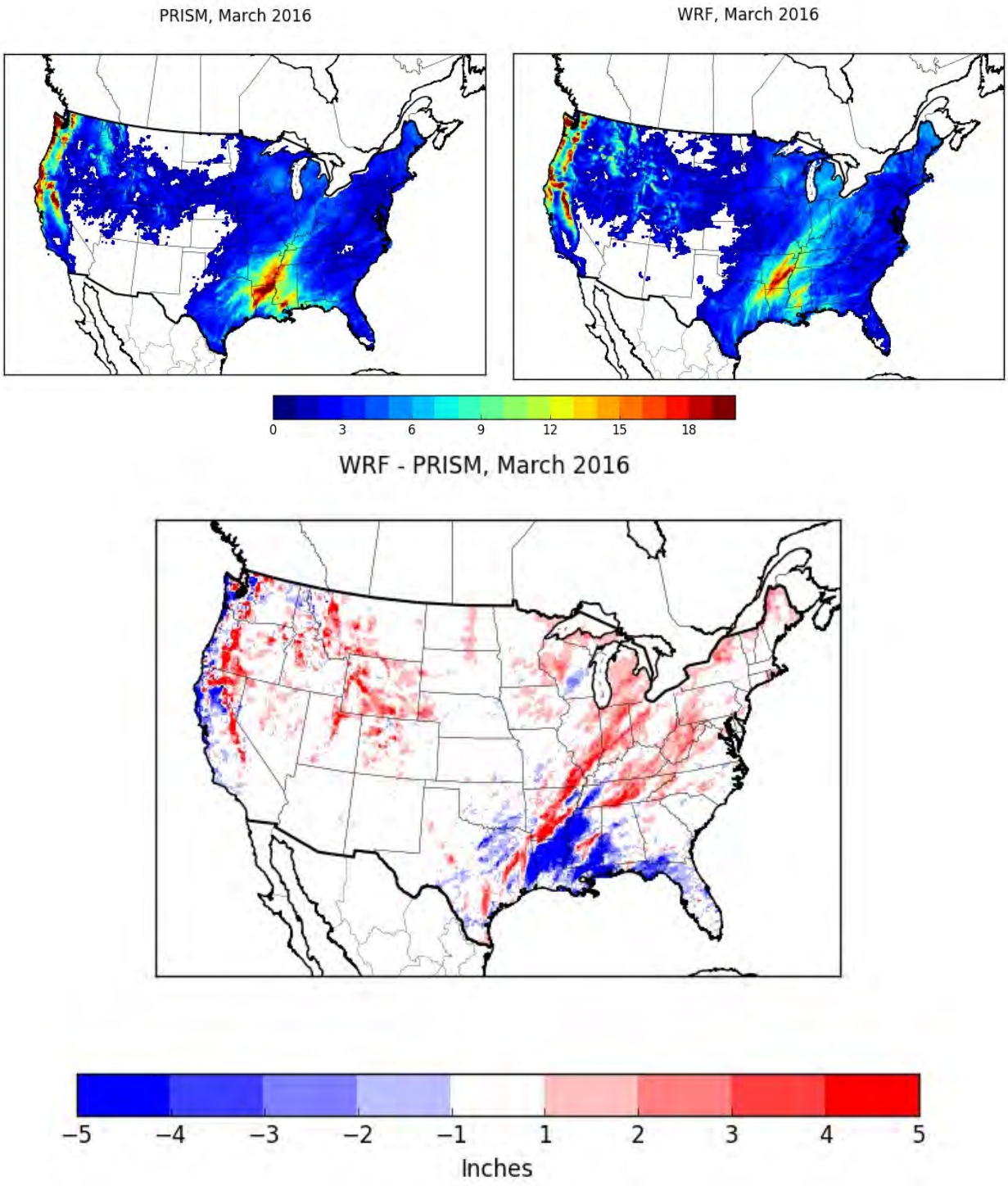

Figure 3.4.15. PRISM analysis (top left) and WRF (top right) estimated monthly total rainfall (in) and the difference (bottom) for March for the 12US simulation.

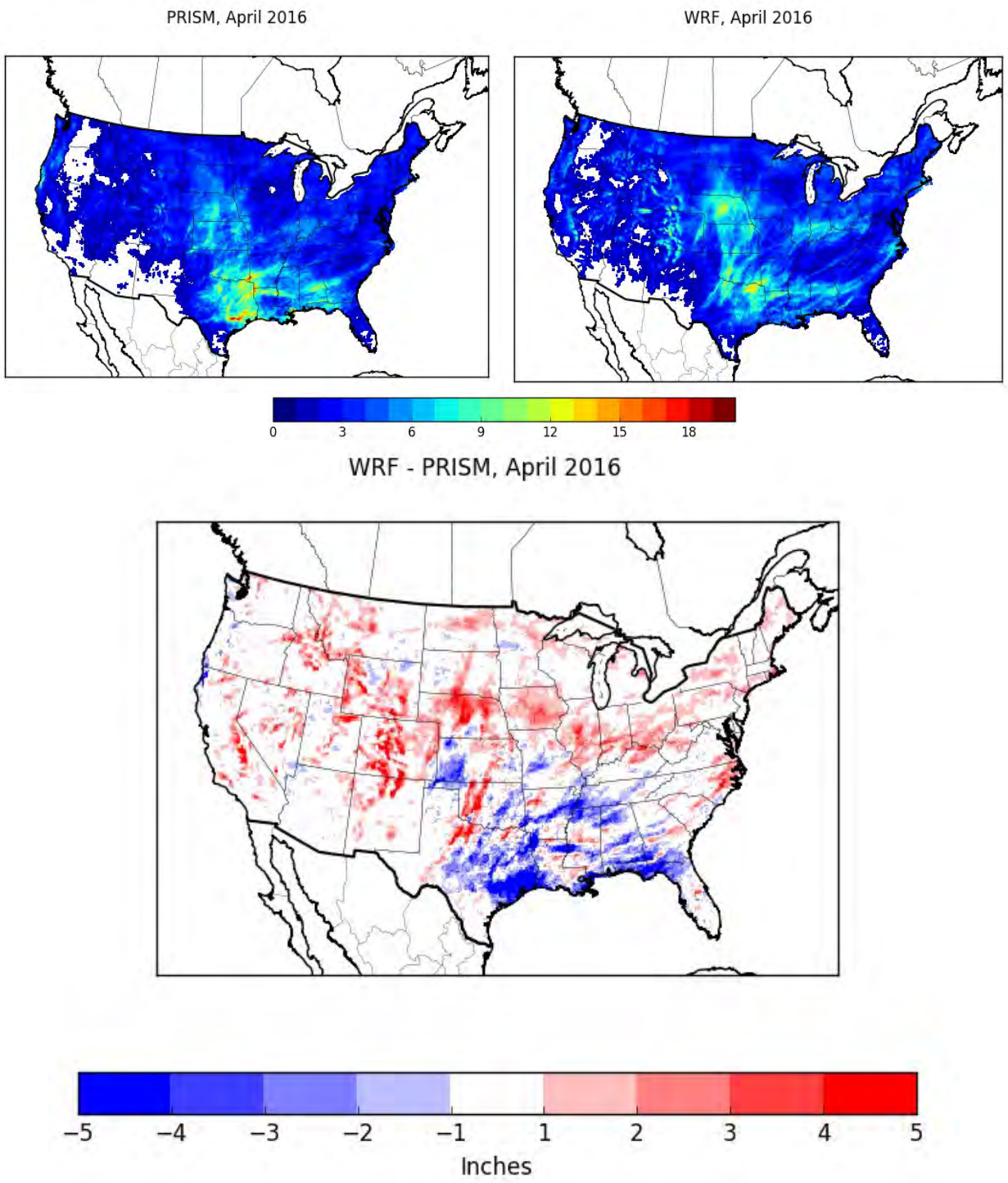

Figure 3.4.16. PRISM analysis (top left) and WRF (top right) estimated monthly total rainfall (in) and the difference (bottom) for April for the 12US simulation.

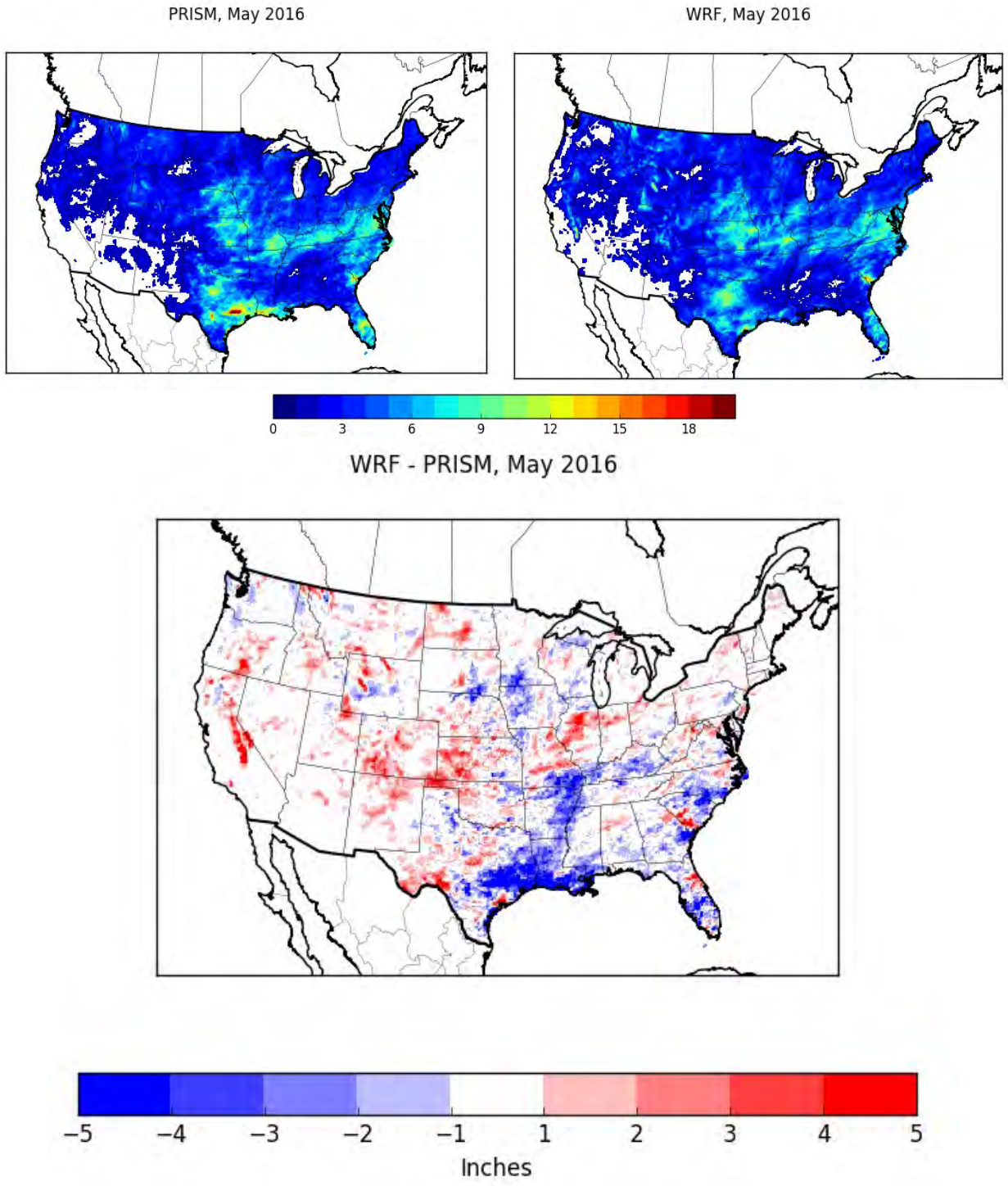

Figure 3.4.17. PRISM analysis (top left) and WRF (top right) estimated monthly total rainfall (in) and the difference (bottom) for May for the 12US simulation.

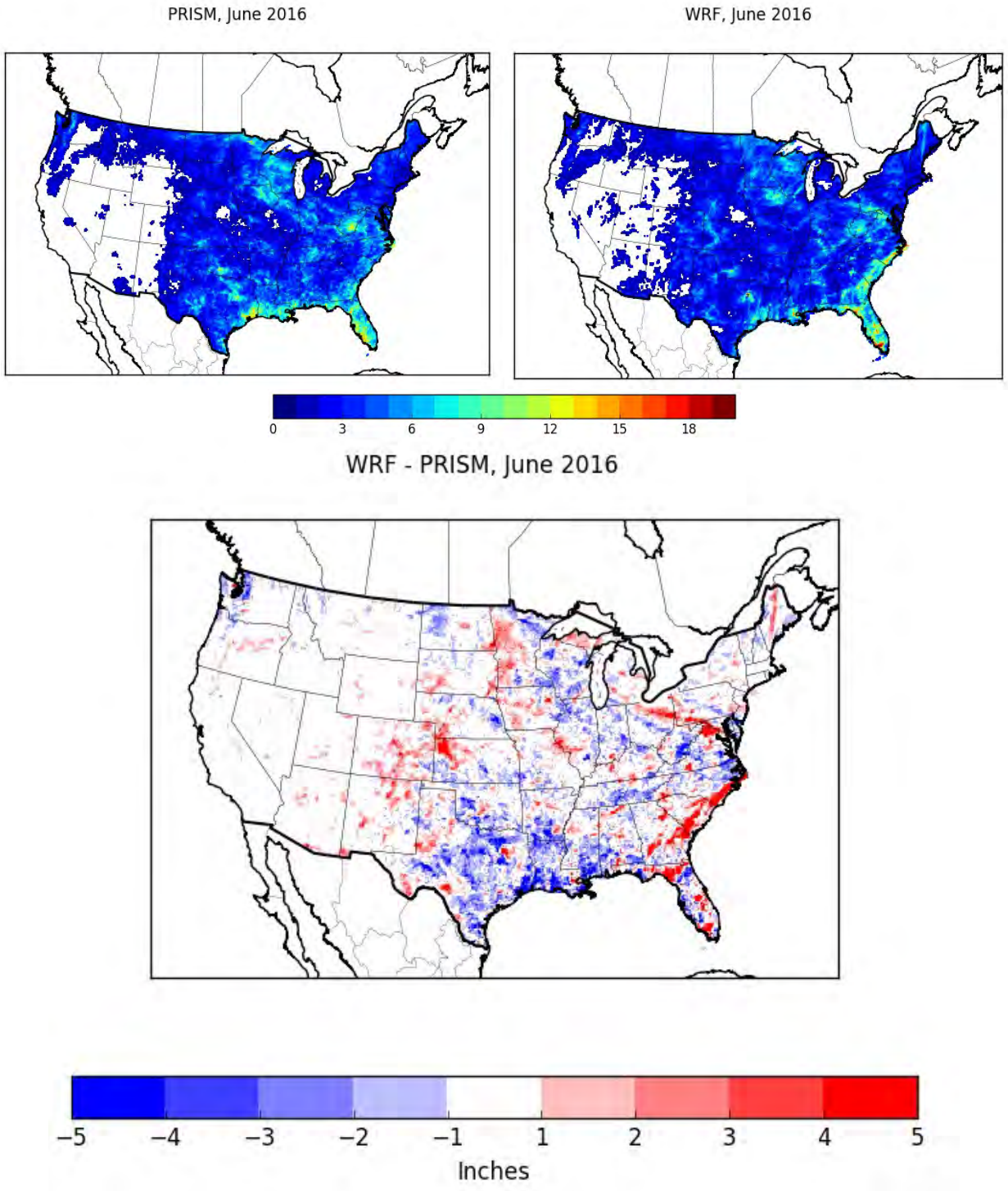

Figure 3.4.18. PRISM analysis (top left) and WRF (top right) estimated monthly total rainfall (in) and the difference (bottom) for June for the 12US simulation.

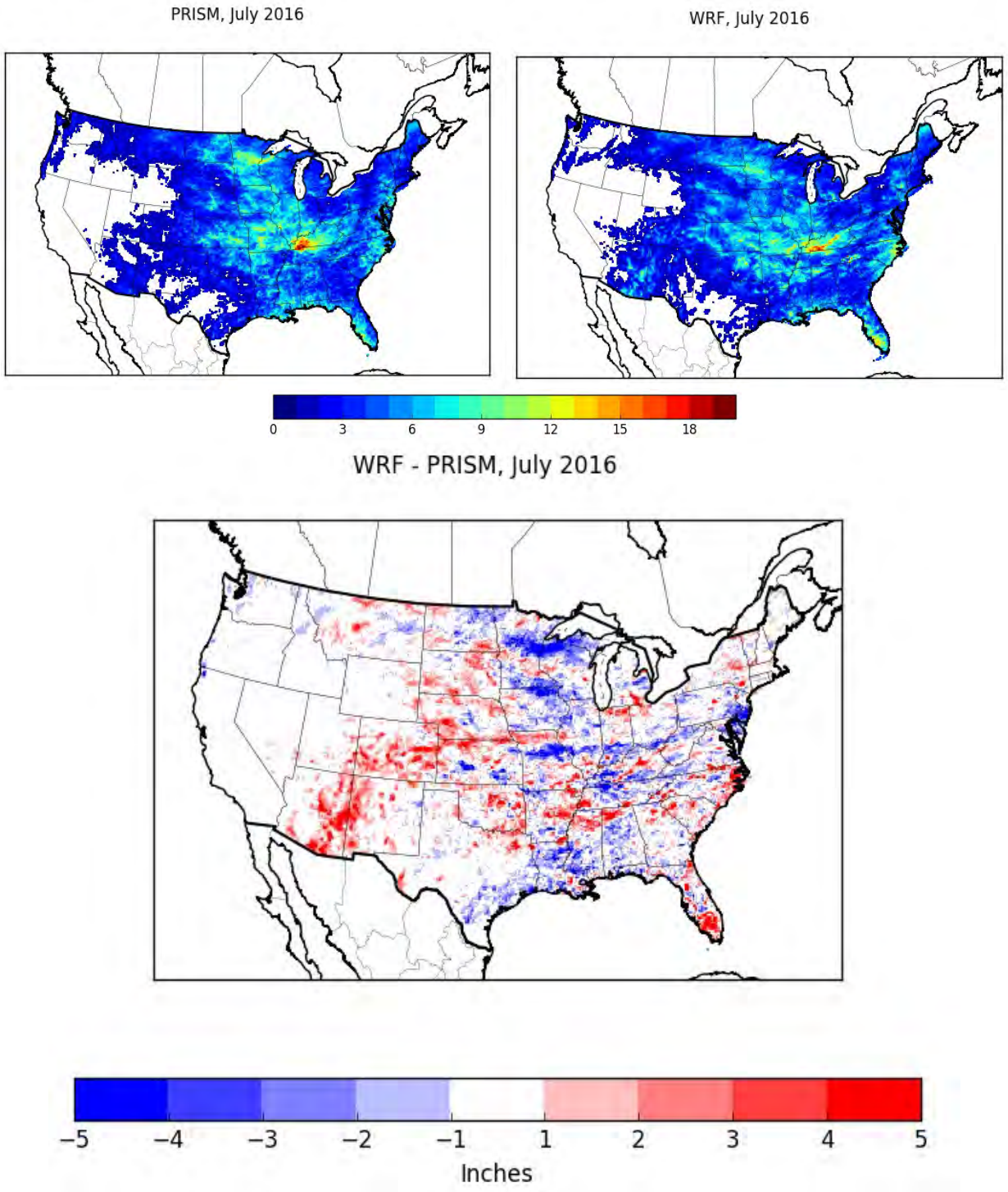

Figure 3.4.19. PRISM analysis (top left) and WRF (top right) estimated monthly total rainfall (in) and the difference (bottom) for July for the 12US simulation.

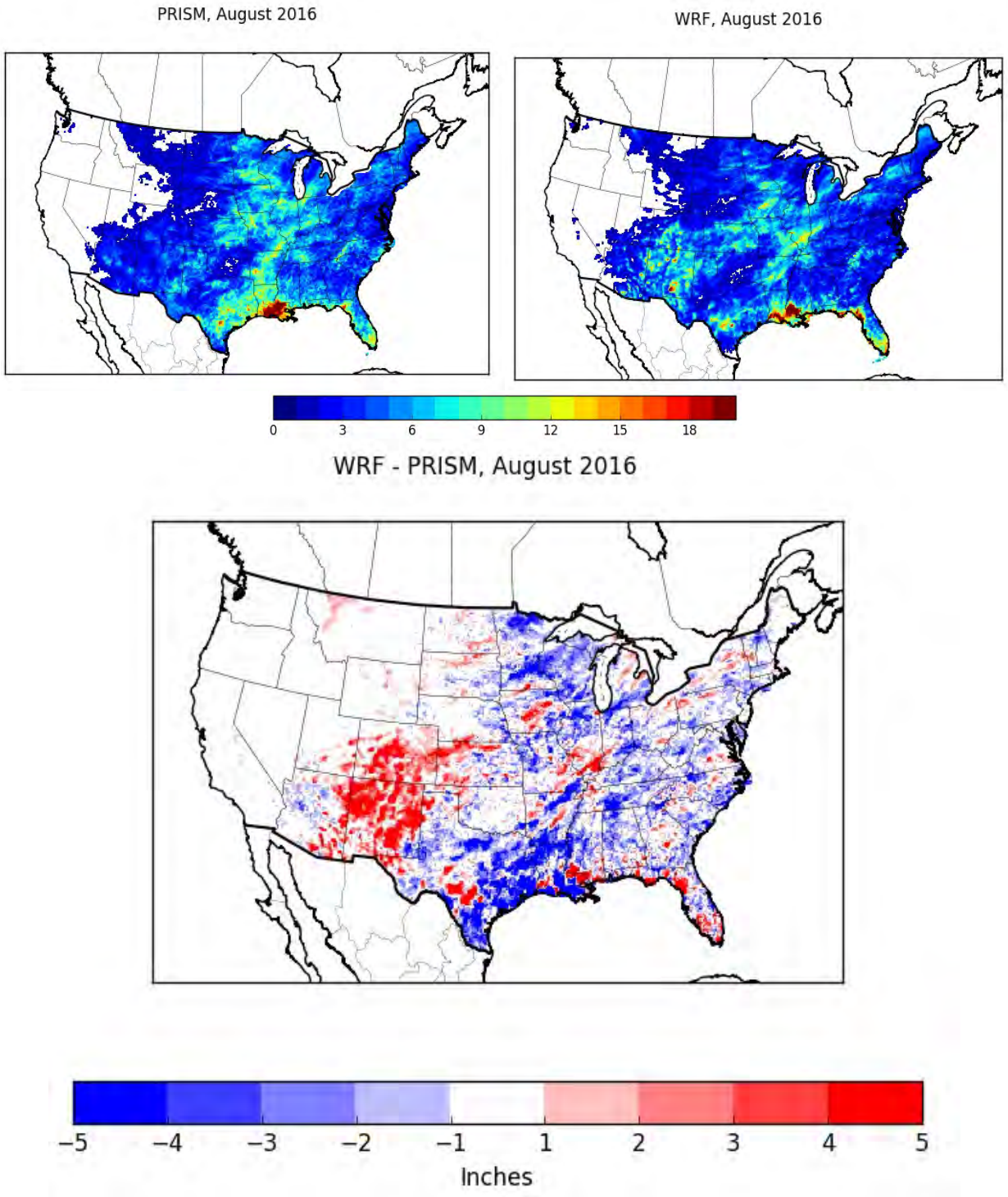

Figure 3.4.20. PRISM analysis (top left) and WRF (top right) estimated monthly total rainfall (in) and the difference (bottom) for August for the 12US simulation.

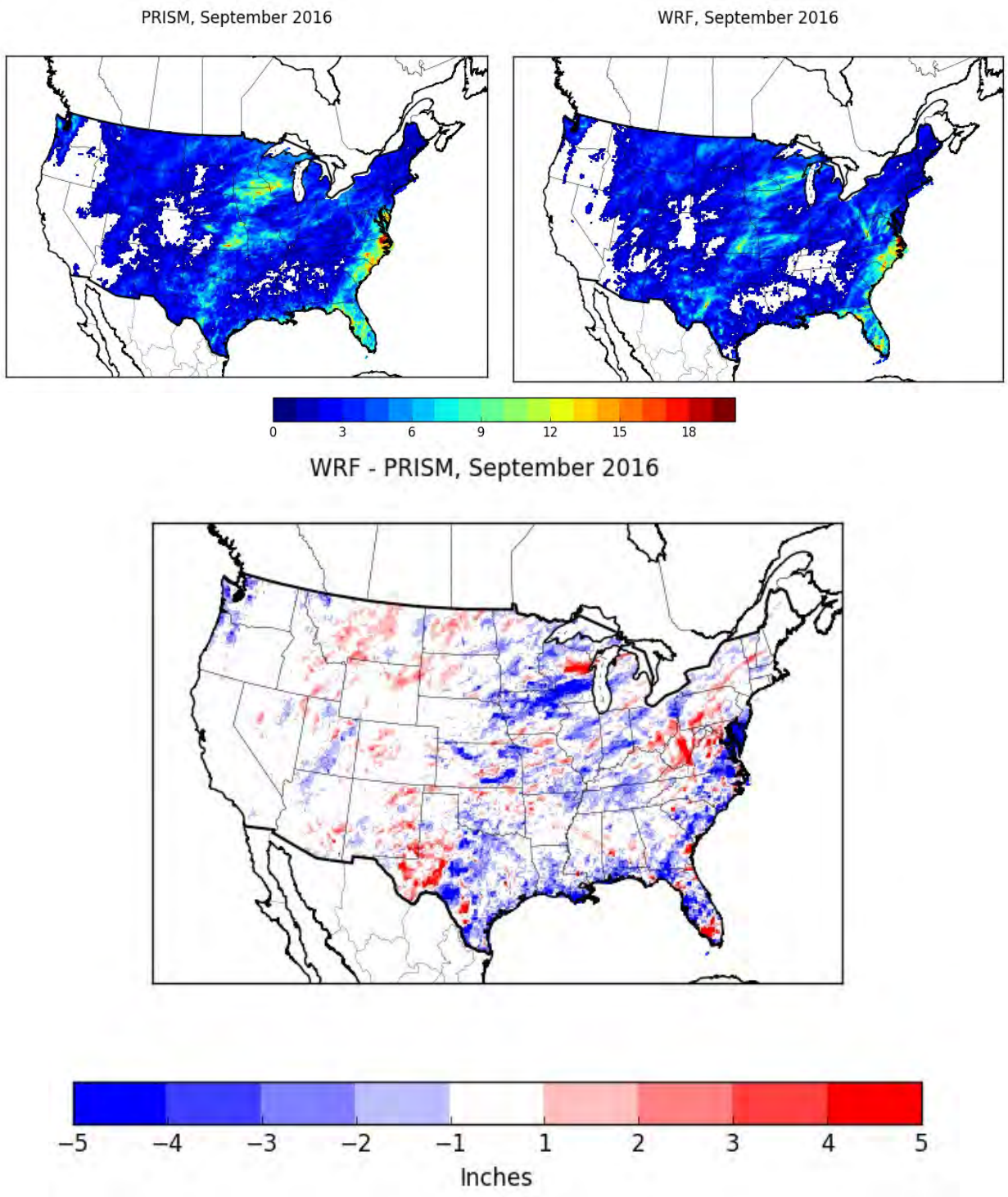

Figure 3.4.21. PRISM analysis (top left) and WRF (top right) estimated monthly total rainfall (in) and the difference (bottom) for September for the 12US simulation.

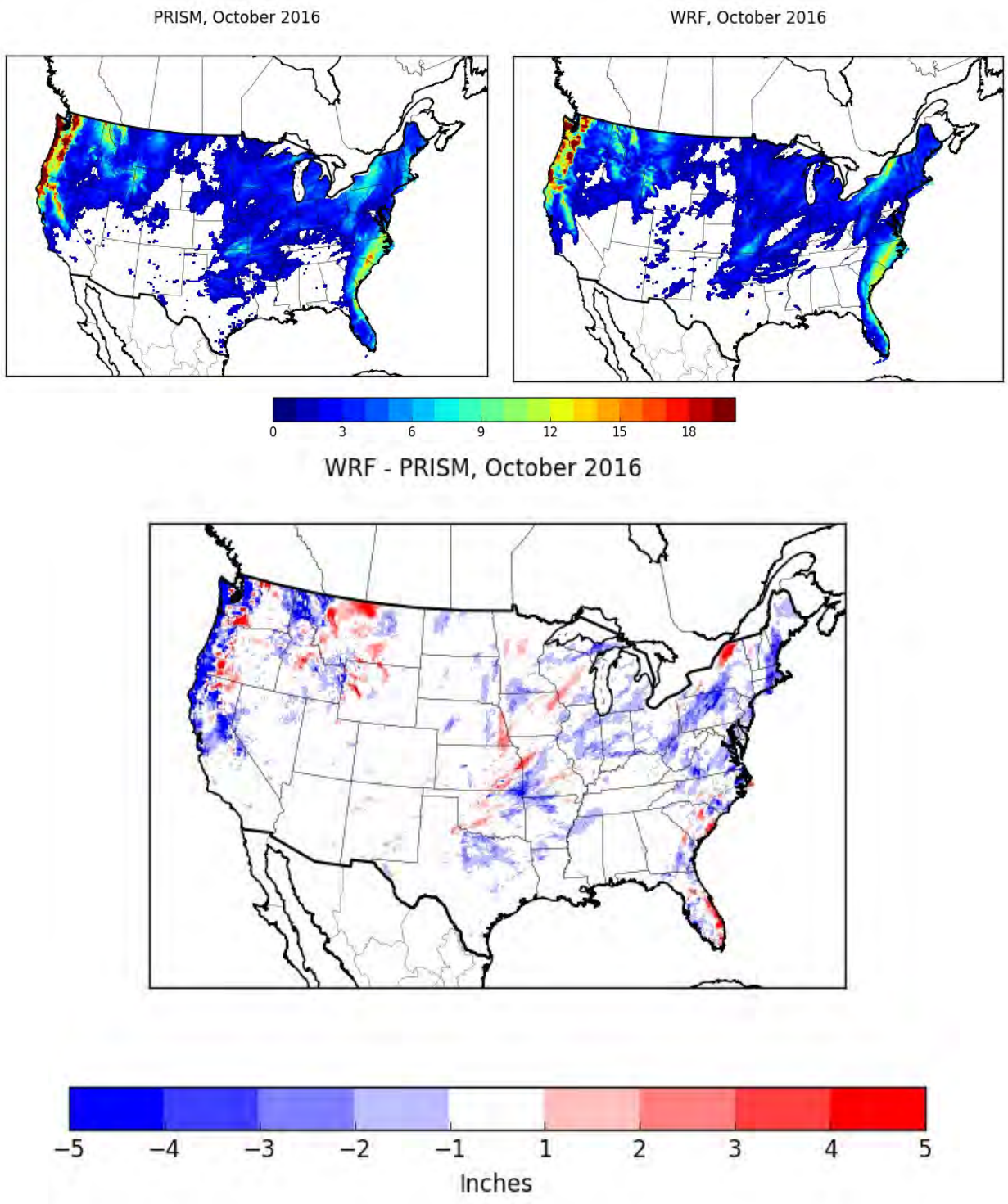

Figure 3.4.22. PRISM analysis (top left) and WRF (top right) estimated monthly total rainfall (in) and the difference (bottom) for October for the 12US simulation.

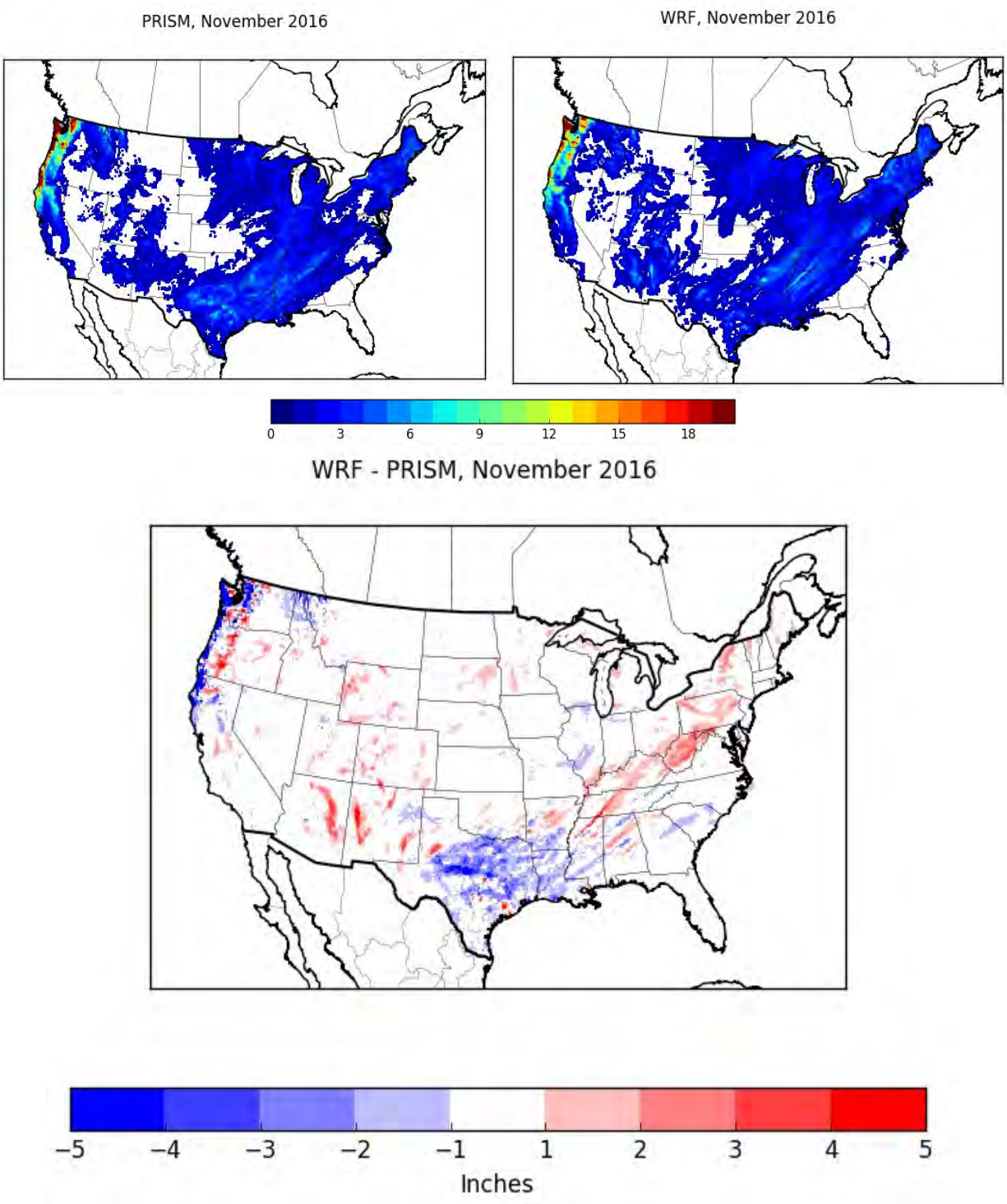

Figure 3.4.23. PRISM analysis (top left) and WRF (top right) estimated monthly total rainfall (in) and the difference (bottom) for November for the 12US simulation.

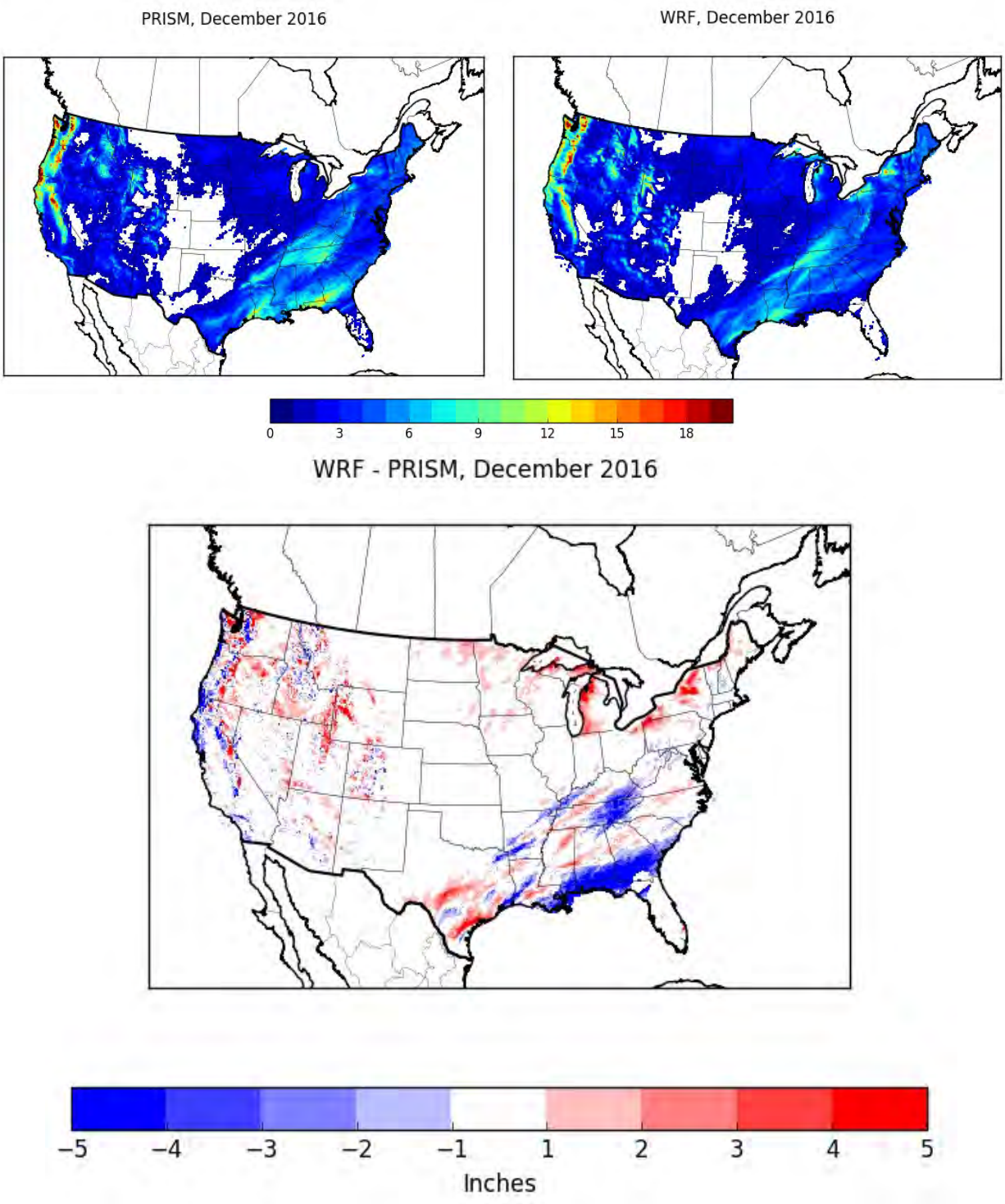

Figure 3.4.24. PRISM analysis (top left) and WRF (top right) estimated monthly total rainfall (in) and the difference (bottom) for December for the 12US simulation.

3.5 Solar Radiation

Photosynthetically activated radiation (PAR) is a fraction of shortwave downward radiation and is an important input for the biogenic emissions model for estimating isoprene (Carlton and Baker, 2011). Isoprene emissions are important for regional ozone chemistry and play a role in secondary organic aerosol formation. Radiation performance evaluation also gives an indirect assessment of how well the model captures cloud formation during daylight hours.

Shortwave downward radiation estimates are compared to surface-based measurements made at SURFRAD and SOLRAD network monitors for the 36NOAM (Figure 3.6.1) 12US (Figure 3.6.2) domains.

Overall, both the 36- and 12km simulations show WRF has little bias in shortwave radiation predictions during the fall and winter months. Biases tend to grow during the spring and peak in the summer, though the spread in overpredictions tends to be less than 100 W/m^2 on average, with a median bias close to zero.

More variability is noted on an hourly basis. WRF tends to overpredict early morning to early afternoon shortwave radiation, while underpredicting the late afternoon and early evening values. The median overprediction at the time of greatest incoming solar radiation is near 100 W/m^2 in the 36km simulation and closer to 50 W/m^2 in the 12km simulation. In the late afternoon and evening hours, the median bias is close to -50 W/m^2 in both simulations. These errors are likely attributable to the model being unable to accurately simulate cloud features at subgrid (<12km) scales. This assumption is based on the slight improvement in predictions at 12km versus 36km.

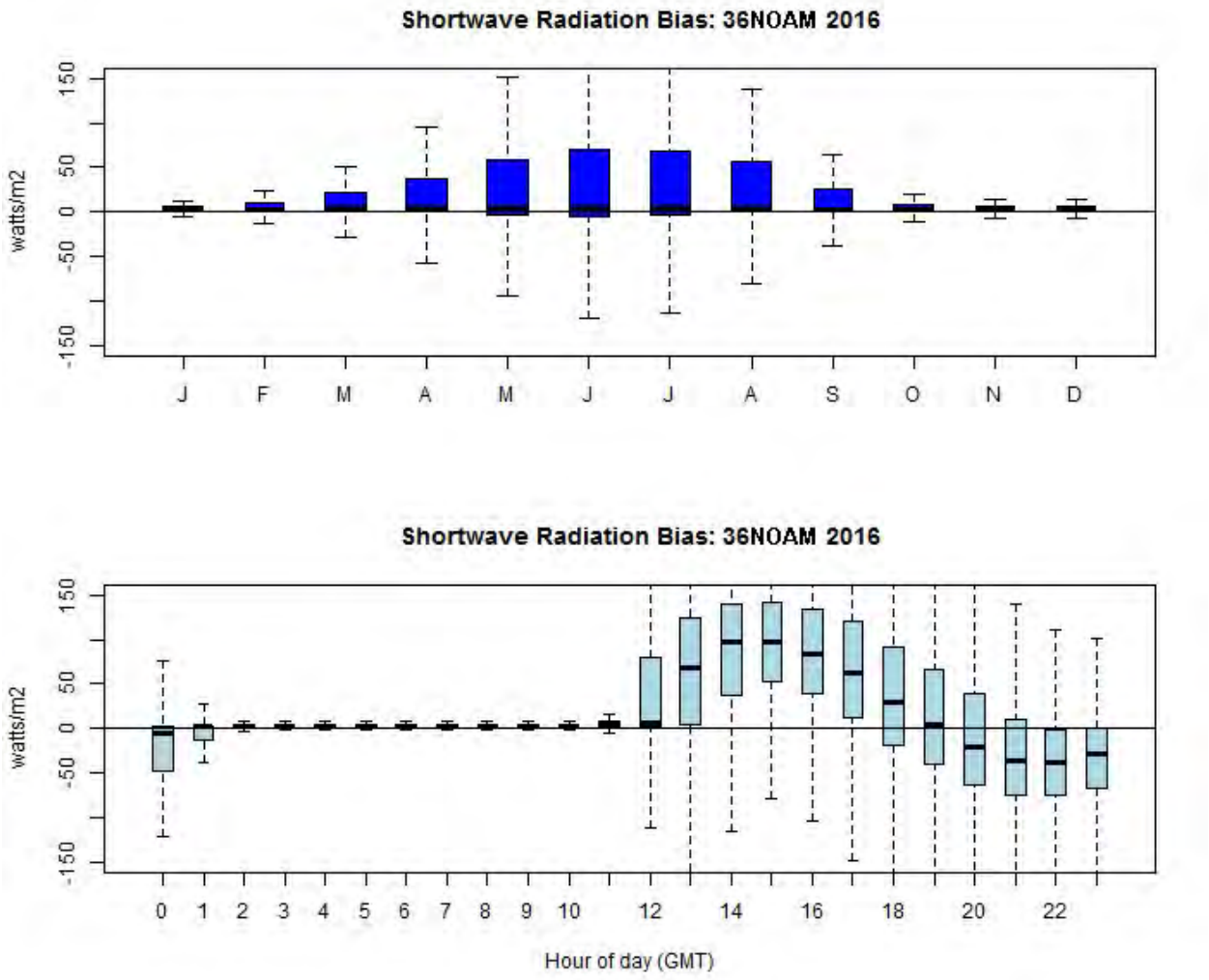

Figure 3.5.1. Distribution of hourly bias for shortwave radiation (W/m^2) by month (top) and by hour of the day (bottom) for the 36NOAM domain.

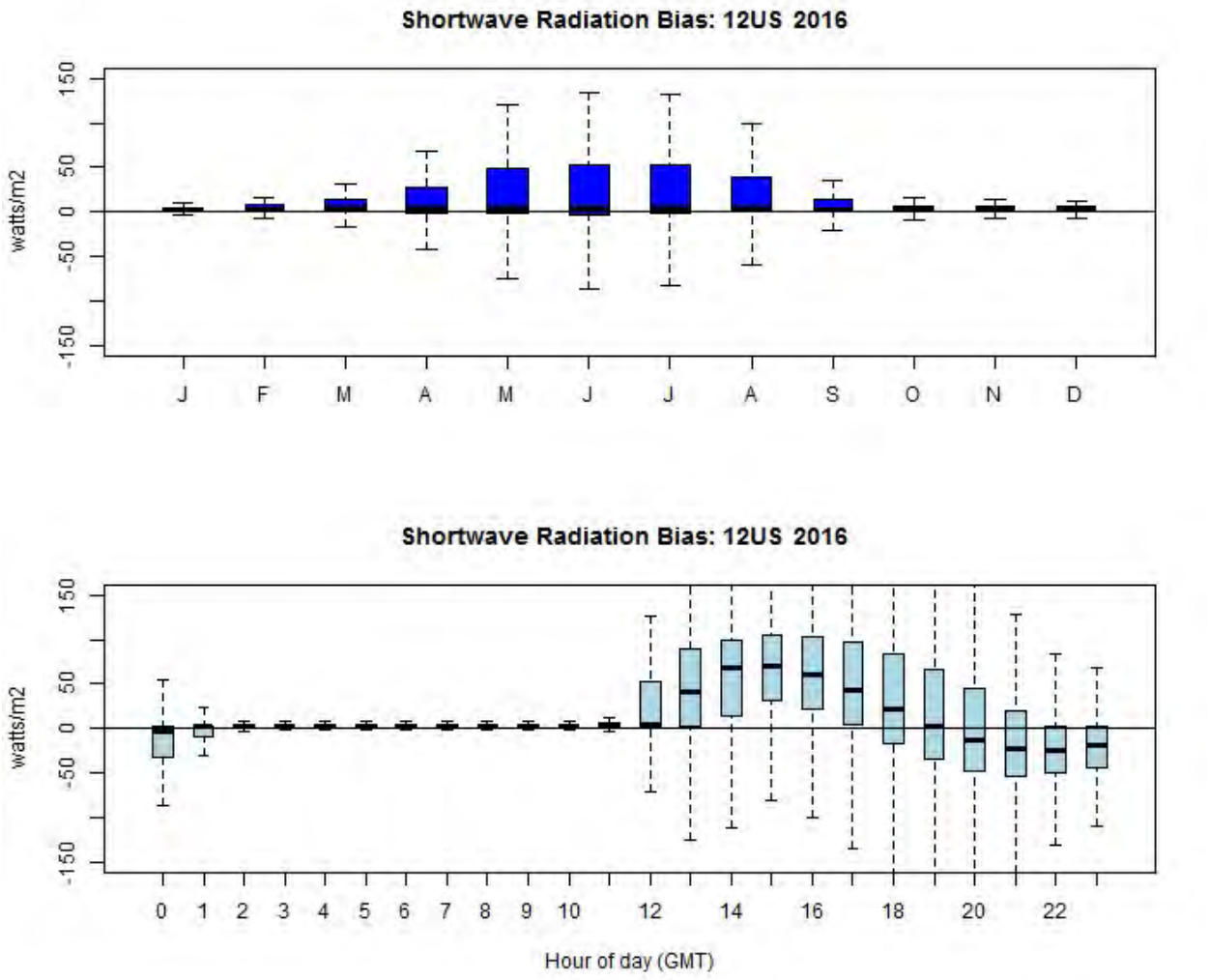

Figure 3.5.2. Distribution of hourly bias for shortwave radiation (W/m^2) by month (top) and by hour of the day (bottom) for the 12US domain.

4 CLIMATE REPRESENTATIVENESS OF 2016

Figures 4.1 and 4.2 show the divisional rankings for observed temperatures across the US for 2016. A climatic representation of the precipitation for 2016 is shown in Figures 4.3 and 4.4. These plots are useful in determining the representativeness of 2016 in terms of certain climatological variables compared to historical averages.

Temperatures in 2016 were above average to much above average across several months of the year, with record warmth observed in many areas of the country at varying times of the year. Cooler than average conditions were noted in the eastern US in January, central and eastern US in May, Pacific Northwest in July, southwest in August, and the Intermountain West and Northwest in December.

Drier than normal conditions were observed across the southeastern US for most of the year with the exception of February, May, September, and October. In the northeast, abnormally dry conditions also persisted throughout much of the year, except in February, August, October, and December. Near-record precipitation was observed in the Deep South and Upper Great Lakes in March and August, and Pacific Northwest in October.

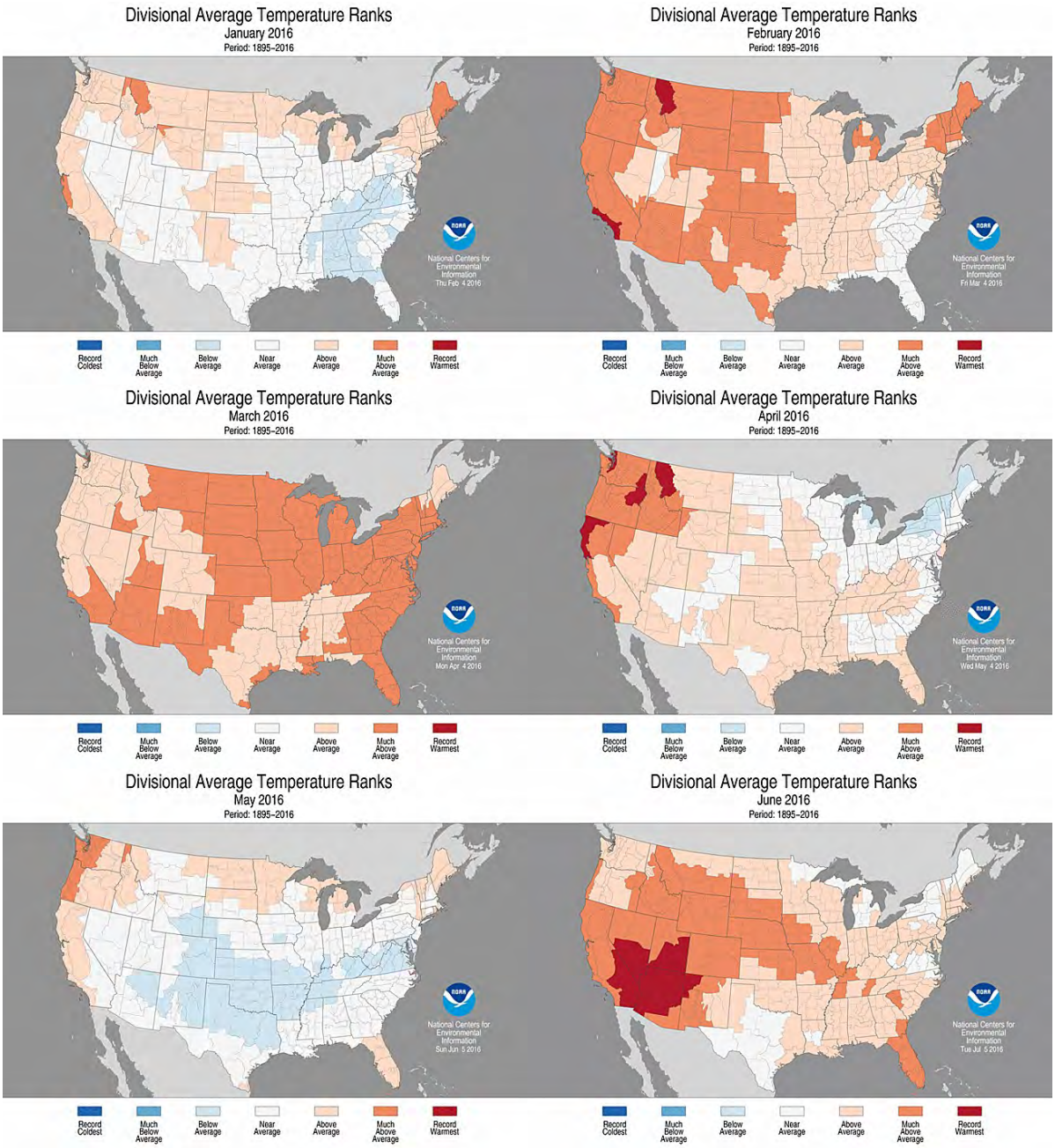

Figure 4.1 Climatic temperature rankings by climate division: January to June 2016. http://www.ncdc.noaa.gov/temp-and-precip/maps.php

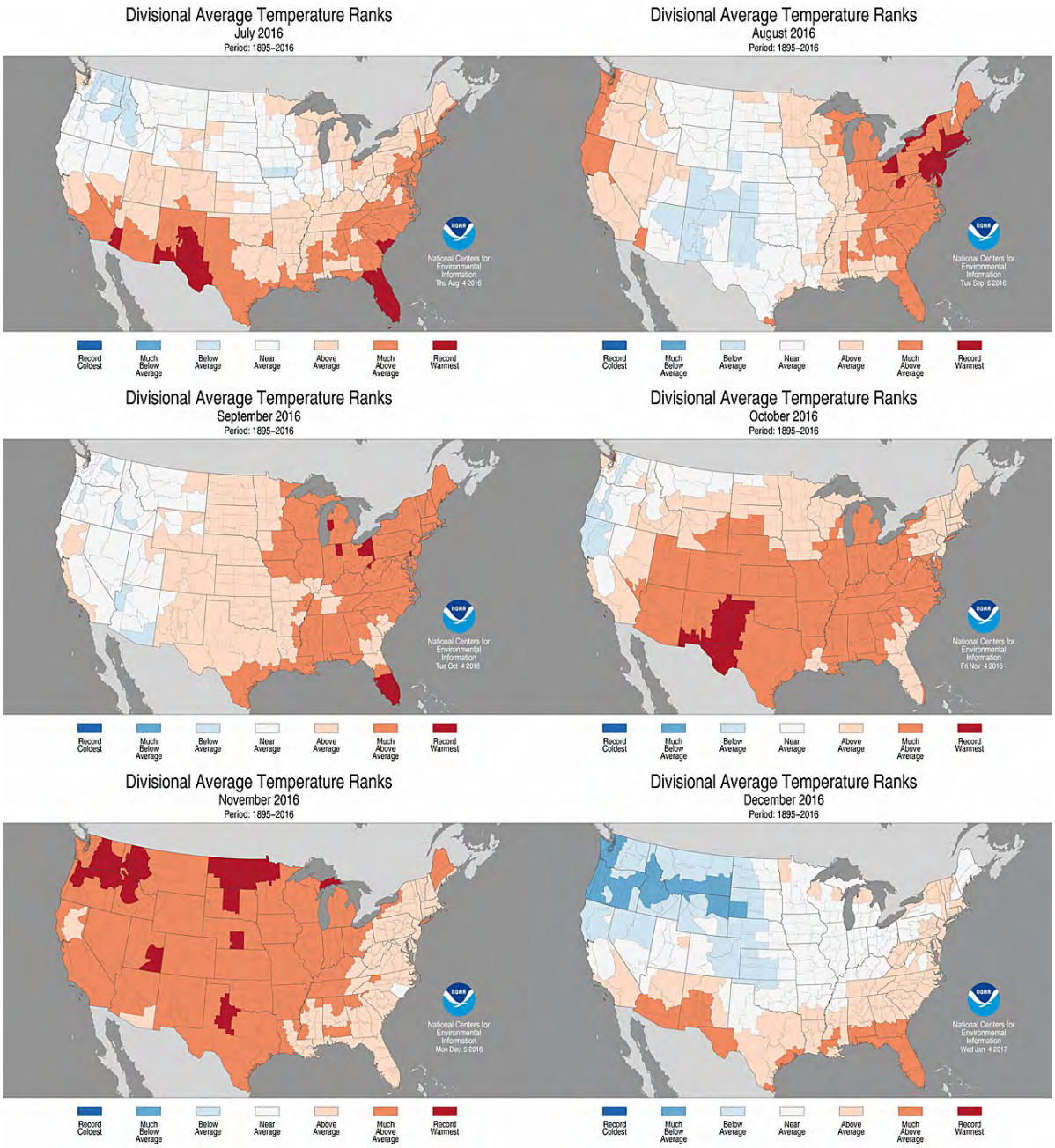

Figure 4.2 Climatic temperature rankings by climate division: July to December 2016. http://www.ncdc.noaa.gov/temp-and-precip/maps.php

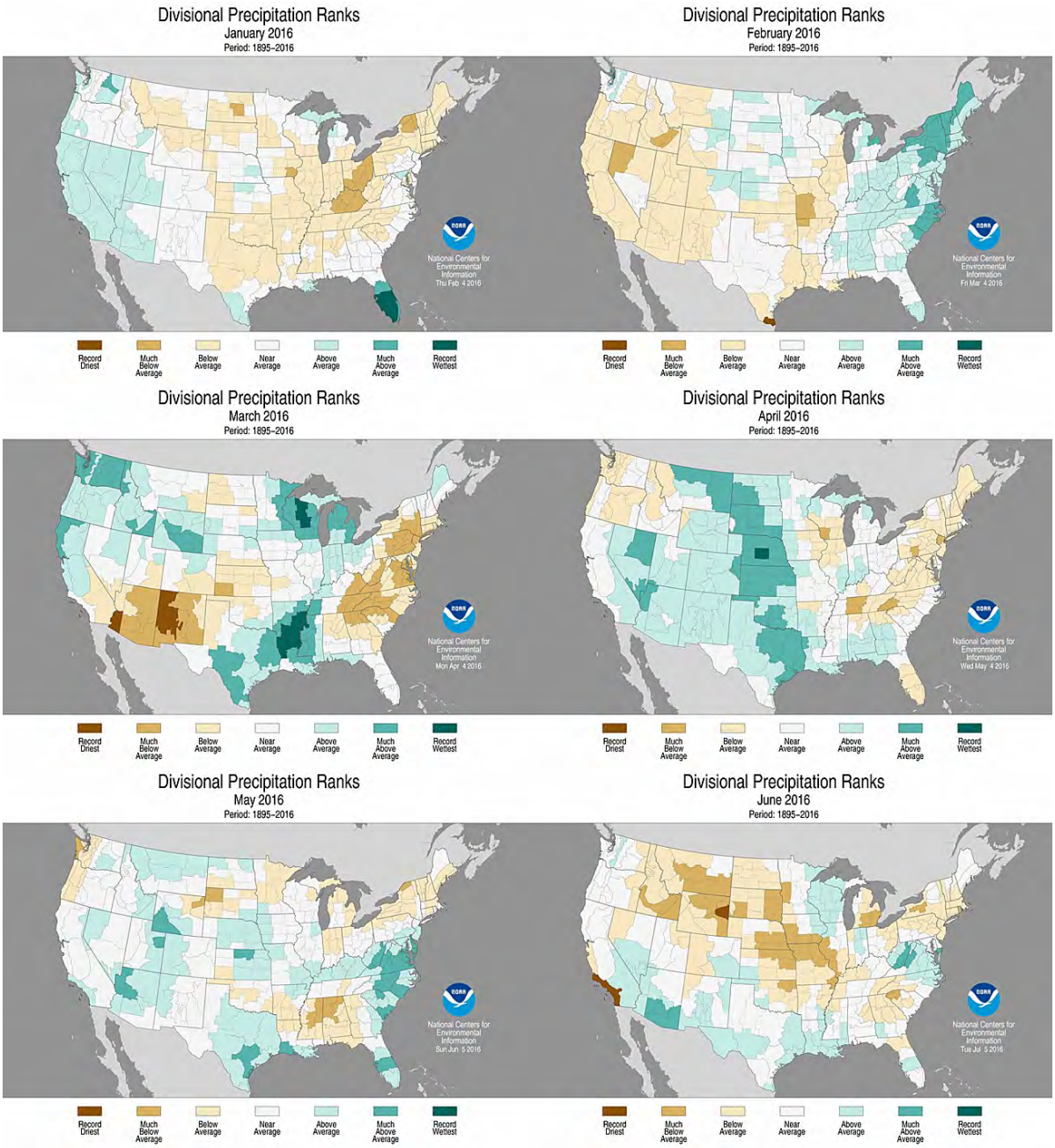

Figure 4.3 Climatic rainfall rankings by climate division: January to June 2016. http://www.ncdc.noaa.gov/temp-and-precip/maps.php

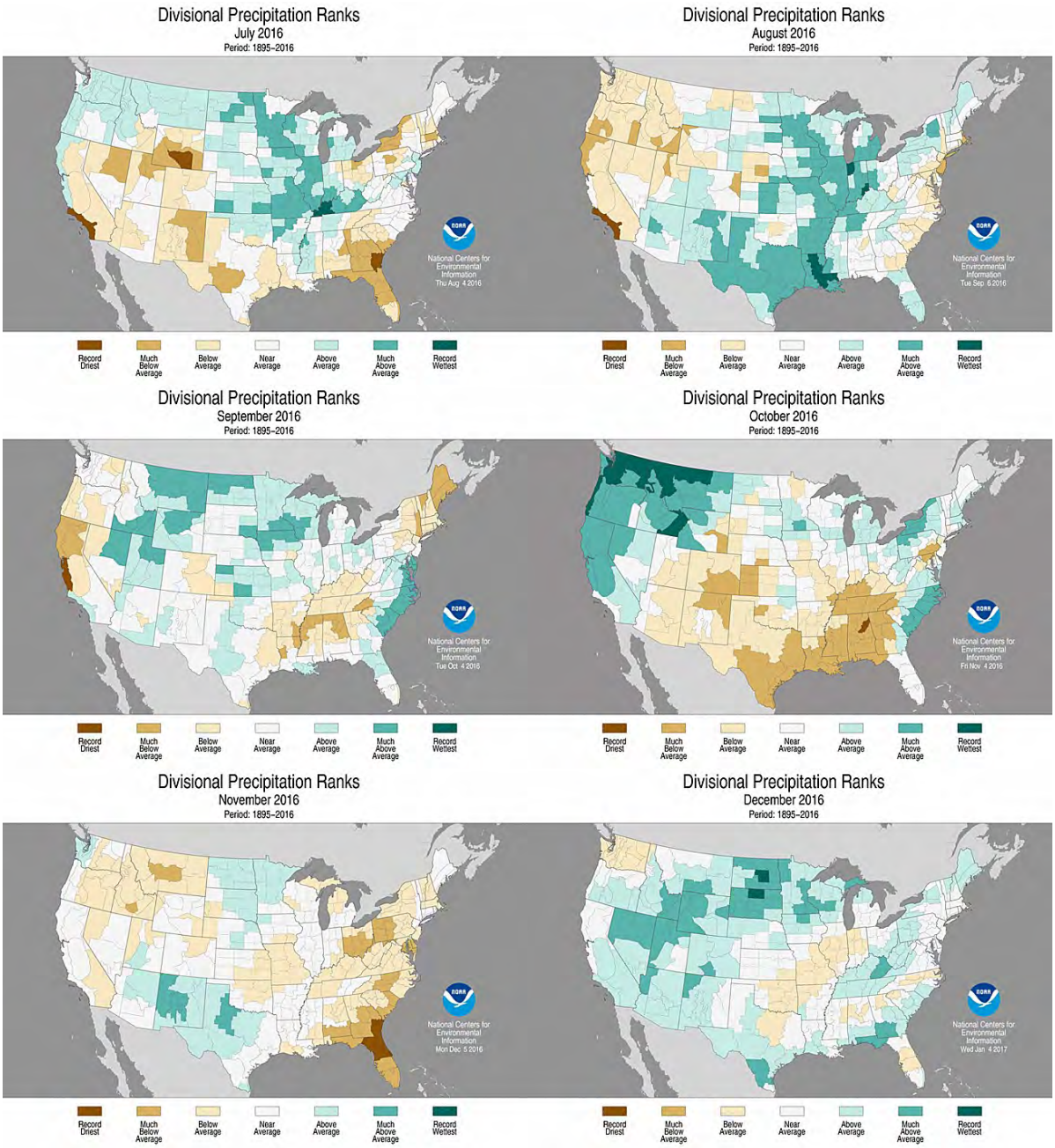

Figure 4.4 Climatic rainfall rankings by climate division: July to December 2016. https://www.ncdc.noaa.gov/sotc/

5 REFERENCES

Boylan, J.W., Russell, A.G., 2006. PM and light extinction model performance metrics, goals, and criteria for three-dimensional air quality models. Atmospheric Environment 40, 4946-4959.

Carlton, A.G., Baker, K.R., 2011. Photochemical Modeling of the Ozark Isoprene Volcano: MEGAN, BEIS, and Their Impacts on Air Quality Predictions. Environmental Science & Technology 45, 4438-4445.

Cooper, O.R., Stohl, A., Hubler, G., Hsie, E.Y., Parrish, D.D., Tuck, A.F., Kiladis, G.N., Oltmans, S.J., Johnson, B.J., Shapiro, M., Moody, J.L., Lefohn, A.S., 2005. Direct Transport of Midlatitude Stratospheric Ozone into the Lower Troposphere and Marine Boundary Layer of the Pacific Ocean. Journal of Geophysical Research – Atmospheres 110, D23310, doi:10.1029/2005JD005783.

ENVIRON, 2008. User's Guide Comprehensive Air Quality Model with Extensions. ENVIRON International Corporation, Novato.

Gilliam, R.C., Pleim, J.E., 2010. Performance Assessment of New Land Surface and Planetary Boundary Layer Physics in the WRF-ARW. Journal of Applied Meteorology and Climatology 49, 760-774.

Heath, Nicholas K., Pleim, J.E., Gilliam, R., Kang, D., 2016. A simple lightning assimilation technique for improving retrospective WRF simulations. Journal of Advances in Modeling Earth Systems. 8. 10.1002/2016MS000735.

Langford, A.O., Reid, S.J., 1998. Dissipation and Mixing of a Small-Scale Stratospheric Intrusion in the Upper Troposphere. Journal of Geophysical Research 103, 31265-31276.

Otte, T.L., Pleim, J.E., 2010. The Meteorology-Chemistry Interface Processor (MCIP) for the CMAQ modeling system: updates through MCIPv3.4.1. Geoscientific Model Development 3, 243-256.

Skamarock, W.C., Klemp, J.B., Dudhia, J., Gill, D.O., Barker, D.M., Duda, M.G., Huang, X., Wang, W., Powers, J.G., 2008. A Description of the Advanced Research WRF Version 3.

Stammer, D., F.J. Wentz, and C.L. Gentemann, 2003, Validation of Microwave Sea Surface Temperature Measurements for Climate Purposes, *J. Climate,* 16, 73-87.

United States Environmental Protection Agency	Office of Air Quality Planning and Standards Air Quality Assessment Division Research Triangle Park, NC	Publication No. EPA-454/R-19-010 July 2019